The Bigger Picture

Electrocatalytic water splitting is a green approach to producing clean H_2 fuel, especially when it is driven by renewable energy sources. Conventional water electrolysis always produces H_2 and O_2 simultaneously under corrosive acidic or alkaline conditions with large voltage inputs, posing safety concerns of H_2/O_2 mixing. Therefore, it is desirable to develop new electrolyzer design for decoupled water splitting in eco-friendly neutral solution with small voltage inputs, enabling separated H_2 and O_2 evolution. Herein, we report (ferrocenylmethyl)trimethylammonium chloride and $Na_4[Fe(CN)_6]$ as proton-independent electron reservoirs to achieve separated H_2 and O_2 evolution in near neutral solution driven by electricity or solar cells under sunlight irradiation. $Na_4[Fe(CN)_6]$ can also integrate H_2 evolution with organic oxidation to yield H_2 and high-value organic products. This work offers promising economic and safety advantages for sustainable H_2 production and organic transformation.

Highlights

Stable proton-independent electron reservoirs of inexpensive iron complexes

Decoupling H_2 evolution from O_2 evolution in neutral electrolyte with small voltage inputs

Photovoltaic-driven decoupled water splitting under natural sunlight irradiation

Decoupled H_2 evolution integrated with valorization of biomass-derived intermediates

eTOC Blurb

Robust proton-independent electron reservoirs of (ferrocenylmethyl)trimethylammonium chloride and $Na_4[Fe(CN)_6]$ are utilized to separate H_2 evolution from O_2 evolution with much lower voltage inputs compared to that of conventional water splitting electrolysis. Such decoupled water splitting can be readily driven by photovoltaics with small photovoltages in near neutral solution under natural sunlight irradiation. The electron reservoirs can facilitate sustainable H_2 production from decoupled water splitting and further integrate H_2 evolution with organic upgrading, yielding two value-added products (H_2 and 2,5-furandicarboxylic acid).

Graphical abstract:

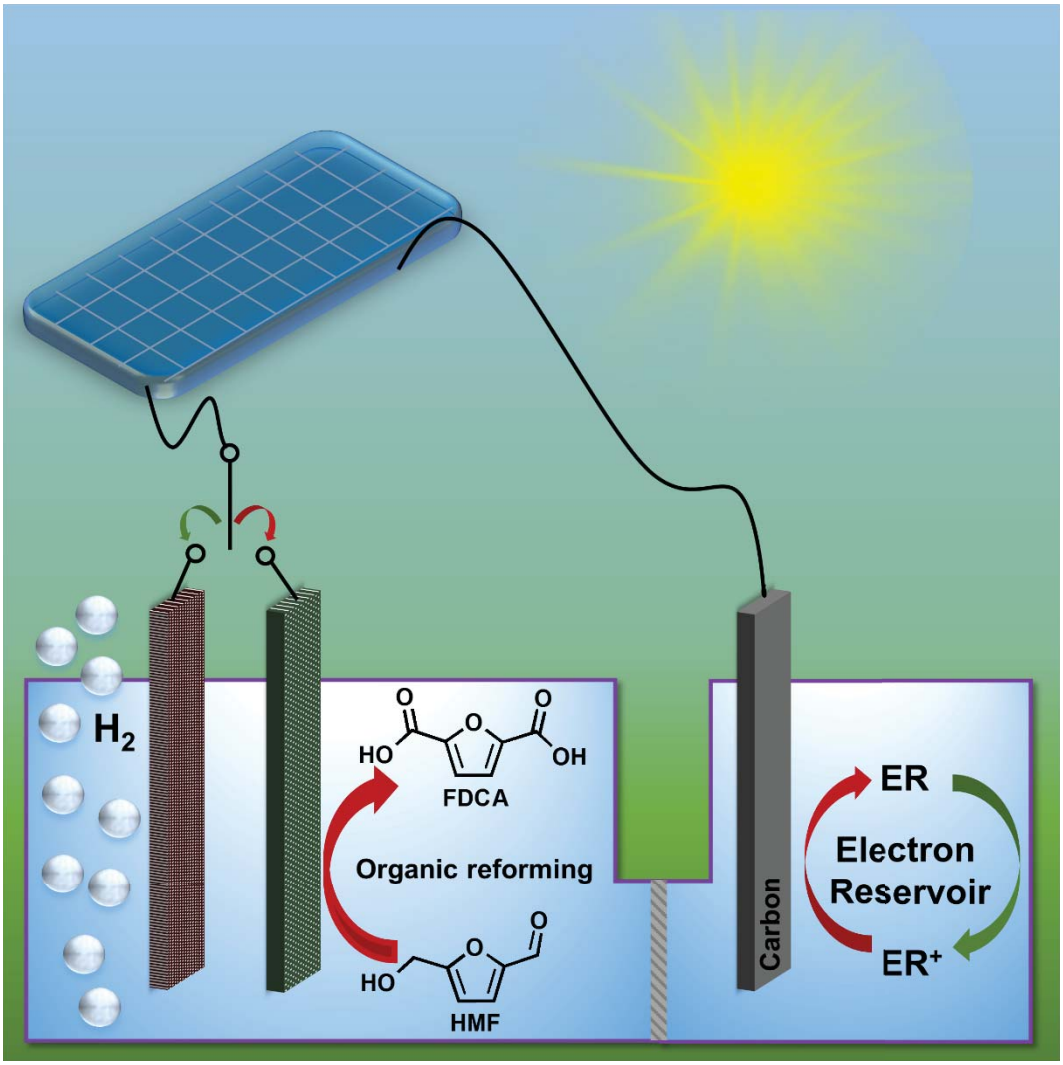

New Electrolyzer Design for Flexible Decoupled Water Splitting and Organic Upgrading with Electron Reservoirs

Wei Li,[1,2] Nan Jiang,[1,2] Bo Hu,[1] Xuan Liu,[1] Fuzhan Song,[1] Guanqun Han,[1] Taylor J. Jordan,[1] Tanner B. Hanson,[1] T. Leo Liu,[1] and Yujie Sun[1,3,*]

[1]Department of Chemistry and Biochemistry, Utah State University, Logan, UT 84322, United States
[2]These authors contributed equally.
[3]Lead contact
*Correspondence: yujie.sun@usu.edu

SUMMARY

Conventional water splitting electrolysis drives the H_2 and O_2 evolution reactions (HER and OER) simultaneously with large voltage inputs. Herein, two inexpensive iron complexes as proton-independent electron reservoirs (ERs) are described for decoupled water electrolysis. (Ferrocenylmethyl)trimethylammonium chloride and $Na_4[Fe(CN)_6]$, which have proper redox potentials in aqueous media, are able to couple their oxidation with HER. The subsequent reduction of the oxidized ER^+ are then paired with OER. Both steps require much smaller voltage than that of direct water splitting. Nearly 100 % Faradaic efficiency and remarkable cycling stability are obtained for both electron reservoirs. Such a decoupled water splitting can also be driven by photovoltaic cells with small photovoltages under sunlight irradiation. Furthermore, a two-step electrolysis of HER and the oxidation of 5-hydroxymethylfurfural mediated by $Na_4[Fe(CN)_6]$ is demonstrated under alkaline condition, producing H_2 and 2,5-furandicarboxylic acid. This work presents a decoupled water electrolyzer design with great flexibility and safety advantages.

INTRODUCTION

H_2 production from water electrolysis with renewable energy inputs is a promising approach to the storage of renewable electricity in chemical forms.[1-4] Due to the thermodynamic requirements and slow kinetics of water splitting, conventional water electrolysis is usually conducted with a large voltage input (1.8–2.5 V) under either acidic or alkaline conditions, utilizing proton exchange membrane (PEM) electrolyzers or alkaline electrolyzers at elevated temperatures, respectively.[5,6] Regardless of the electrolyzer type, conventional water electrolysis always produces H_2 and O_2 simultaneously (**Scheme 1A**), and thus the rate of the H_2 evolution reaction (HER) is strictly dependent on the rate of the O_2 evolution reaction (OER).[7-9] Furthermore, the concurrence of HER and OER results in potential H_2/O_2 gas crossover, which is particularly severe at low current density (*e.g.*, 10 mA cm^{-2}, a benchmark current density for solar-driven water splitting) and/or under high gas pressure, even if an ostensibly gas impermeable membrane is utilized.[10-13] This will further require the downstream purification of H_2 *(e.g.,* catalytic de-oxygenation). In addition, H_2/O_2 mixing may lead to the formation of reactive oxygen species due to the coexistence of H_2, O_2 and catalysts under electrocatalytic conditions, which would degrade the electrolyzer and shorten its operation lifetime.[14, 15] Overall, these limitations of conventional water splitting electrolysis call upon an alternative electrolyzer design, not only circumventing these drawbacks but also enabling more flexibility in electrolyzer manufacture for a wide range of applications.

Recent years have witnessed the emergence of a decoupling strategy for water splitting, wherein redox mediators are employed to decouple HER from OER. Representative proton-dependent redox mediators include phosphomolybdic acid and hydroquinone sulfonate.[8,12, 16] The combination of V(III)/V(II) and Ce(IV)/Ce(III) redox mediators has also been employed for indirect water electrolysis.[17,18] However, all of these redox mediators only function well in strongly acidic media which are corrosive environments for the device and severely limit the scope of suitable electrocatalysts, particularly for OER,[19] as most of the earth-abundant transition metal-based OER electrocatalysts cannot survive in strongly acidic electrolytes. The required proton migration between electrolyzer chambers also results in a great pH gradient and hence a large ohmic resistance.[20] Recently, a solid-state redox relay of $NiOOH/Ni(OH)_2$ was reported for alkaline water electrolysis, wherein HER and OER took place simultaneously in separate chambers with a fairly large voltage input (~2.1 V).[21] Nevertheless, $NiOOH/Ni(OH)_2$ is only stable under strongly alkaline condition and it requires long-time pre-activation prior to operation. Reversing current polarity or physically swapping two saturated $NiOOH/Ni(OH)_2$ electrodes are needed to regenerate the redox replay for electrolysis cycling. Furthermore, the produced O_2 through the sluggish OER under the alkaline conditions is not of significant value.[9, 22] These limitations motivate us to develop alternative inexpensive electrolyzers of great convenience, flexibility, and durability for decoupled water electrolysis under benign conditions and preferably generating high-value products instead of O_2.

Herein, we demonstrate that a ferrocene-derived complex, (ferrocenylmethyl)trimethylammonium chloride (FcNCl), is able to act as a stable proton-independent electron reservoir to decouple HER from OER in near neutral electrolyte (0.5 M Na_2SO_4). Besides, $Na_4[Fe(CN)_6]$ is employed as a robust and low-cost proton-independent electron reservoir with a wider stable pH range from neutral to alkaline conditions not only for decoupled water splitting but also for H_2 production integrated with organic upgrading. By taking the advantage of these two electron reservoirs, HER and OER, which have to take place simultaneously in one-step water splitting, are separated and coupled with the oxidation and reduction of electron reservoirs, respectively. Hence, HER and OER can occur at different times with different rates and both steps require smaller voltage inputs compared to that of direct water splitting. The separation of HER from OER also eliminates the further downstream purification of H_2, reducing the cost and increasing the purity of H_2 fuel.[8] The neutral electrolyte enables us to utilize nonprecious metal phosphide and Ni foam as

electrocatalysts to catalyze HER and OER, respectively. Because of the substantially reduced voltage inputs for the decoupled water electrolysis, the H_2 and O_2 evolution can be driven by commercial photovoltaic (PV) cells with photovoltages (< 1.7 V) lower than those of reported PV-driven water electrolysis. Thus a wider solar spectrum could be utilized, expanding the candidate pool of semiconductors absorbing longer-wavelength sunlight for solar-driven water electrolysis without the need of many solar cells in series connection.[7,12,23] With the assistance of the alkaline stable $Na_4[Fe(CN)_6]$ electron reservoir, OER can be replaced with an organic oxidation to produce value-added product from biomass-derived intermediate compound (*e.g.*, 5-hydroxymethylfurfural). A two-step electrolysis of decoupled HER and organic oxidation is also successfully demonstrated. Overall, the use of proton-independent electron reservoirs enables great flexibility in electrolyzer design for decoupled water splitting, H_2 production and organic upgrading. It allows the cathodic and anodic reactions in the working compartment to occur at different times, not only avoiding the H_2/O_2 mixing problem but also making both reaction rates independent of each other. The utilization of environmentally benign neutral electrolyte further expands the pool of electrocatalyst candidates encompassing those inexpensive 1st-row transition metal-based electrocatalysts, and allows for potential integration with biocatalysts for the production of biofuels, bioproducts,[24-27] and seawater electrolysis.

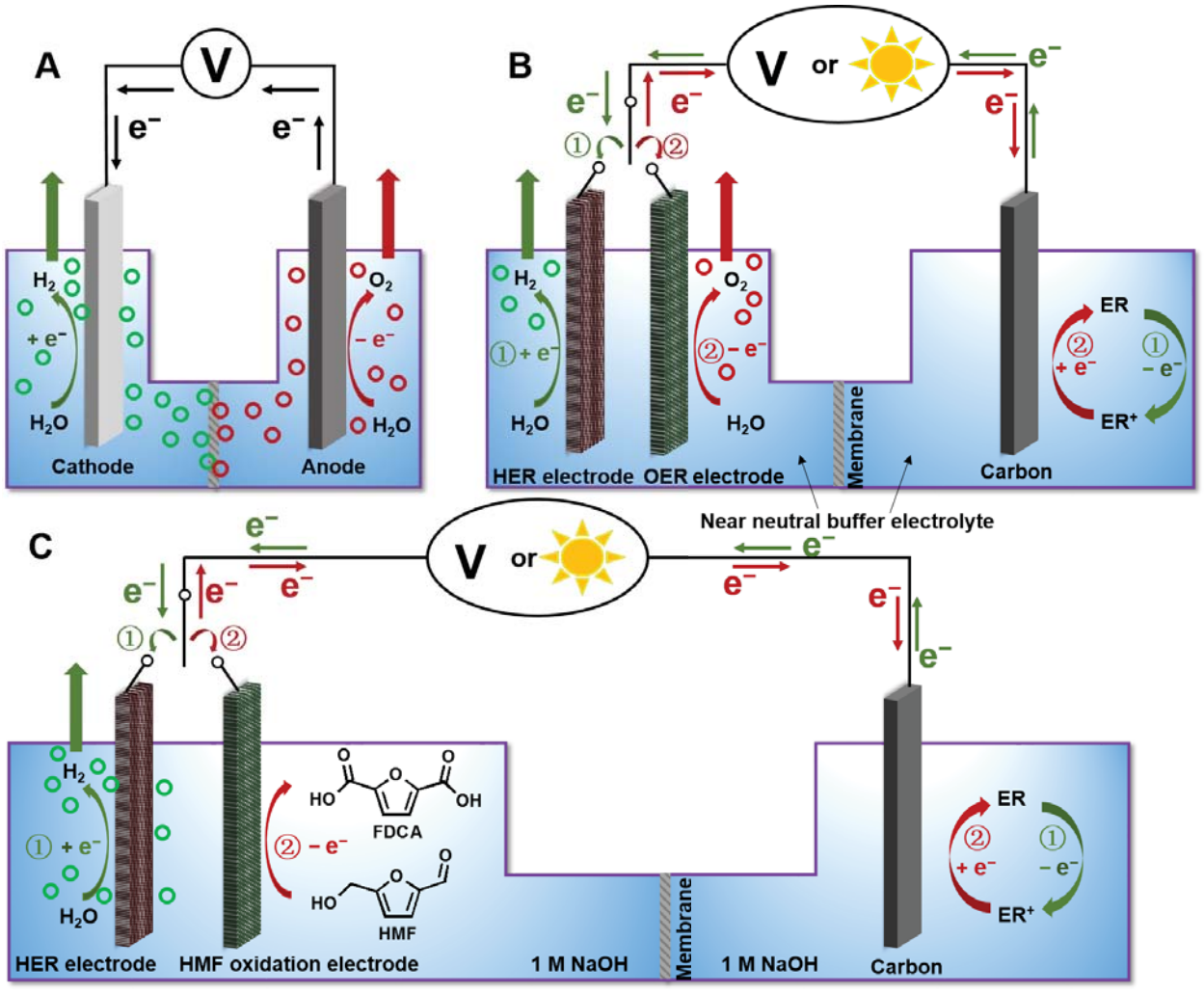

Scheme 1. Schematic illustration of electrolyzer designs.
(A) Conventional electrolyzer for one-step full water splitting.

(B) A new electrolyzer design for decoupled water splitting with stepwise HER and OER in near neutral electrolyte, wherein two working electrodes are alternatively utilized in the working compartment while a carbon electrode is used in the counter compartment containing an electron reservoir of either FcNCl or $Na_4[Fe(CN)_6]$.
(C) A new electrolyzer design for stepwise HER and organic oxidation in alkaline electrolyte (1 M NaOH). $Na_4[Fe(CN)_6]$ is introduced in the counter chamber with a carbon electrode.
For (B) and (C), ER and ER^+ denote the reduced (*i.e.*, FcNCl or $[Fe(CN)_6]^{4-}$) and oxidized (*i.e.*, $FcNCl^+$ or $[Fe(CN)_6]^{3-}$) forms of the adopted electron reservoir, respectively.

RESULTS AND DISCUSSION

Principle for decoupled water splitting and integrated organic upgrading

The principle for decoupled water splitting in near neutral solution is illustrated in **Scheme 1B**. An ideal electron reservoir should possess a reversible redox potential positioned between the electrocatalytic onset potentials of HER and OER in the same electrolyte. A two-compartment H-cell will be adopted with an ion exchange membrane. In the working chamber both the HER (*e.g.*, a transition metal phosphide working electrode) and OER (*e.g.*, a Ni foam working electrode) electrodes are placed; while a carbon counter electrode is positioned in the counter chamber containing the electron reservoir solution. In step 1, the HER working electrode is connected to the carbon counter electrode through an external power source. Upon an appropriate negative voltage bias applied to the HER working electrode, H_2 evolution will take place on it and simultaneously the oxidation of electron reservoir will occur on the carbon counter electrode. In this case, the voltage input will be smaller than that required for full water splitting, as the oxidation potential of electron reservoir is less positive compared to the OER onset potential. After a certain amount of charge passed (determined by the capacity of electron reservoir), step 2 switches the connection from the HER electrode to the OER electrode. When a sufficient positive voltage bias is applied to the OER working electrode, O_2 evolution will take place and meanwhile the reduction of the oxidized electron reservoir (ER^+) back to its original state (ER) will occur on the carbon counter electrode. Such a positive voltage bias is also smaller than that for full water splitting, as the reduction potential of the oxidized electron reservoir is less negative relative to the HER onset potential. Under alkaline condition, OER in step 2 can be replaced by electrochemical organic oxidation (**Scheme 1C**), such as the oxidation of 5-hydroxymethylfurfural (HMF) to 2,5-furandicarboxylic acid (FDCA), in that its required oxidation potential is less positive than that of OER. Under this new scenario, a large voltage input for one-step water splitting is separated into two smaller voltage inputs for individual HER, OER, or organic upgrading, which can be readily driven by PV cells of small photovoltages. The key to the success of this decoupling strategy is to find a suitable electron reservoir complex.

Selection criteria of electron reservoir

As alluded in the above discussion, an ideal electron reservoir for decoupled water electrolysis should satisfy the following criteria: (i) high solubility in water, (ii) fast and reversible proton-independent redox feature positioned between the HER and OER onset potentials, (iii) strong robustness for repeated redox cycling, and (iv) low-cost composition and synthesis from abundant materials. The (ferrocenylmethyl)trimethylammonium chloride, FcNCl, exhibits high water solubility and excellent electrochemical stability in a long cycling neural aqueous redox flow battery,[28] and indeed meets all the criteria. FcNCl can be conveniently synthesized via direct alkylation of a commercially available precursor (ferrocenylmethyl)-dimethylamine (FcN) with methyl chloride in a nearly unity yield.[28] Even though the precursor FcN is almost insoluble in water, the solubility of FcNCl dramatically increases to at least 4 M in water. The most critical feature of our electron reservoir distinct from the reported proton-dependent redox mediators is that the redox electrochemistry does not involve protonation or deprotonation for the proton-

independent electron reservoir, eliminating the dependence on the use of strongly acidic electrolytes.[8,12,16] Instead, a mild near neutral electrolyte (0.5 M Na_2SO_4) was used.

The electrochemistry of FcNCl was investigated via cyclic voltammetry and compared to the HER and OER onset potentials. As plotted in **Figure 1**, the cyclic voltammogram of 50 mM FcNCl in 0.5 M Na_2SO_4 (pH ~ 6.5) showed a reversible redox couple at 0.40 V *vs.* Ag/AgCl (sat. KCl) on a glassy carbon electrode. In the absence of electrocatalysts, HER and OER currents do not take off until −1.2 and 1.7 V *vs.* Ag/AgCl, respectively, on carbon electrodes in 0.5 M Na_2SO_4. In near neutral electrolyte, a large group of earth-abundant electrocatalysts can be employed to reduce the voltage inputs for HER and OER.[29- 36] Therefore, when a nickel foam decorated with Ni_2P (Ni_2P/Ni/NF) and a bare Ni foam (NF) were used as the HER and OER electrodes (**Figures S1** and **S2**), respectively, the overpotentials for the two half reactions of water splitting were dramatically reduced (**Figure 1**). Nevertheless, the HER and OER still needed applied potentials beyond −1.0 and +1.0 V *vs.* Ag/AgCl, respectively, to achieve appreciable catalytic current densities. Therefore, even with the assistance of water splitting electrocatalysts, the redox potential of FcNCl was still well positioned between the HER and OER onsets. In addition, the scan rate dependence of the cyclic voltammograms of FcNCl was also studied (**Figure S3**). The linear trend obtained from the variation of its anodic and cathodic peak currents along the square root of scan rate indicated that this redox process involved a molecular species in solution under diffusion control. The diffusion constant of FcNCl was further probed via linear sweep voltammogram (LSV) using a rotating disk electrode (**Figure S4**). Calculation based on the derived Levich pot resulted in a diffusion constant of 0.71×10^{-6} cm^2 s^{-1} and an electron transfer rate constant of 1.33×10^{-5} cm s^{-1} for FcNCl in 0.5 M Na_2SO_4, both of which were in good agreement with reported values for FcNCl and analogous complexes in aqueous media.[28]

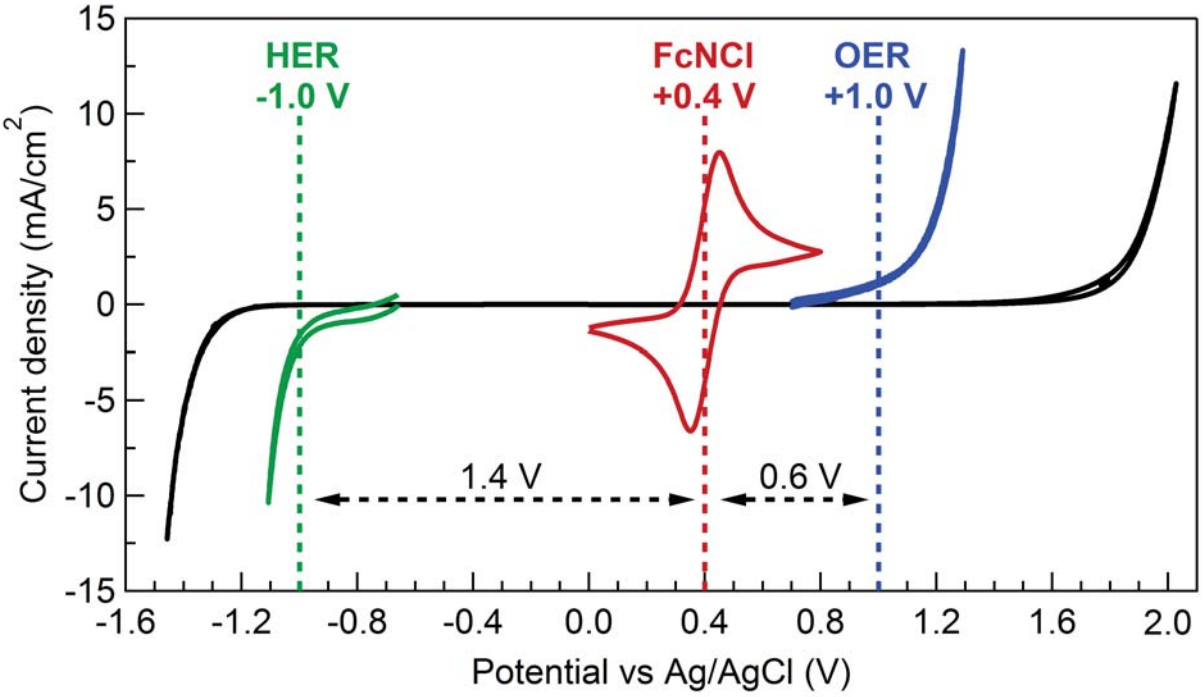

Figure 1. Comparison of the cyclic voltammograms of FcNCl, HER, and OER under near neutral condition. All the CV curves were collected in a three-electrode configuration in 0.5 M Na_2SO_4 (pH = 6.5) using Ag/AgCl (sat. KCl) as the reference electrode. Cyclic voltammogram of 50 mM FcNCl (red) was collected at a scan rate of 100 mV s^{-1} with a glassy carbon working electrode and carbon counter electrode. Cyclic

voltammograms of HER (black) and OER (black) were collected on bare glassy carbon electrodes at a scan rate of 5 mV s^{-1} (iR-corrected). Cyclic voltammograms (iR-corrected) of HER on Ni_2P/Ni/NF (green) and OER on nickel foam (blue) were collected at a scan rate of 5 mV s^{-1} with a carbon counter electrode.

Decoupled water electrolysis using FcNCl

According to the aforementioned experimental results obtained in three-electrode configuration, we were confident that FcNCl could act as an electron reservoir for decoupled water electrolysis. As an initial attempt to evaluate the feasibility of our strategy, a two-electrode compartment H-cell with an anion exchange membrane was utilized to collect the linear sweep voltammogram of HER on Ni_2P/Ni/NF in 0.5 M Na_2SO_4. A carbon rod was utilized as the counter electrode. A negative voltage bias was applied to Ni_2P/Ni/NF and no catalytic HER current was observed until scanning beyond −2.4 V (**Figure 2A**). However, upon the addition of 50 mM FcNCl in the counter electrode compartment, the catalytic HER current on Ni_2P/Ni/NF rose rapidly after −1.4 V, saving nearly 1 V voltage input compared to the above condition (step 1 in **Scheme 1B**). With an external bias of −1.8 V continuously applied to the Ni_2P/Ni/NF working electrode, the produced H_2 amount in an air-tight H-cell was quantified by gas chromatography (GC) and compared to the theoretically calculated amount assuming all the passed charge was utilized to form H_2. **Figure 2B** plots the GC-measured and theoretically calculated H_2 amounts and the near overlap of these two H_2 evolution traces rendered a Faradaic efficiency close to 100 % for H_2 evolution. Note that only H_2 was produced during this electrolysis and the corresponding anodic reaction was the oxidation of FcNCl to $FcNCl^+$ on the carbon counter electrode. No O_2 was detected in the headspace of the counter chamber (**Figure S5**), indicating the high purity of H_2 product.

After the 50 mM FcNCl in the counter compartment had been fully oxidized, we switched the working electrode connection from the Ni_2P/Ni/NF electrode to the NF electrode (step 2 in **Scheme 1B**). Subsequently, a positive voltage bias was applied to NF to drive O_2 evolution. As displayed in **Figure 2C**, the catalytic OER current took off at merely 0.6 V. This is because the redox potential of $FcNCl^{+/0}$ (0.4 V *vs.* Ag/AgCl) was relatively closer to the OER onset (~1.0 V *vs.* Ag/AgCl) on NF (**Figure 1**). Nevertheless, in the absence of $FcNCl^+$ in the counter compartment, a much larger voltage input (> 2.4 V) was required to conduct OER using the same electrodes. The GC-measured O_2 amount also matched the theoretically calculated value very well (**Figure 2D**), confirming the nearly unity Faradaic efficiency for this decoupled O_2 evolution electrolysis at an applied bias of 1.7 V. In the meantime, no H_2 was detected in the counter chamber (**Figure S5**). In fact, the cathodic reaction occurring in the counter compartment was the reduction of $FcNCl^+$ back to the FcNCl, thus accomplishing its regeneration cycle as an electron reservoir.

The voltage between Ni_2P/Ni/NF and carbon counter electrodes was −1.478 V to drive a current density of −10 mA cm^{-2} for HER in the presence of 50 mM FcNCl (**Figure 2A**). In the second step for OER and $FcNCl^+$ reduction, a small voltage of 0.954 V was required to achieve the current density of 10 mA cm^{-2} (**Figure 2C**). If a Ni_2P/Ni/NF || NF electrode couple was used for one-step water splitting without any electron reservoir, a much larger voltage input of 2.338 V was required to produce 10 mA cm^{-2} in 0.5 M Na_2SO_4 (**Figure S6**). This demonstrates a high efficiency of 96% for two-step decoupled water splitting relative to one-step direct water splitting. This efficiency is higher than that of the reported phosphomolybdic acid-mediated (79 %) and potassium hydroquinone sulfonate-mediated (80 %) decoupled water electrolyzers and comparable to that (93 %) of silicotungstic acid-mediated system in acidic solution and $Ni(OH)_2$-mediated decoupled water electrolysis system (92 %) without considering resistive factors.[8,9,16,37] The practical energy efficiency of our decoupled water electrolyzer could be calculated by dividing the thermoneutral potential (*i.e.*, 1.48 V, see details in Supplemental Information) of water electrolysis by the total applied voltage at room temperature,[38,39] when the Faradaic efficiencies of HER and OER are both 100 %. The calculated energy efficiency was 61 % at 10 mA cm^{-2}, which is comparable to

that of the silicotungstic acid-mediated (63 %), the potassium hydroquinone sulfonate-mediated (61 %) or the phosphomolybdic acid-mediated (59 %) decoupled water electrolyzers, and the Pt-based PEM electrolyzer (67 %) in acidic electrolyte and the efficiency of $Ni(OH)_2$-mediated Ir || Pt electrolyzer (67 %) in 1 M NaOH solution at room temperature (**Table S1**).[8,16,21,37] When proton buffers were added in the electrolyte, we were able to collect the HER and OER linear sweep voltammograms at pH 5, 7, and 9 (**Figures S7** – **S9**). Within the pH range from 5 to 9, our FcNCl functioned well as an electron reservoir for decoupled water splitting.

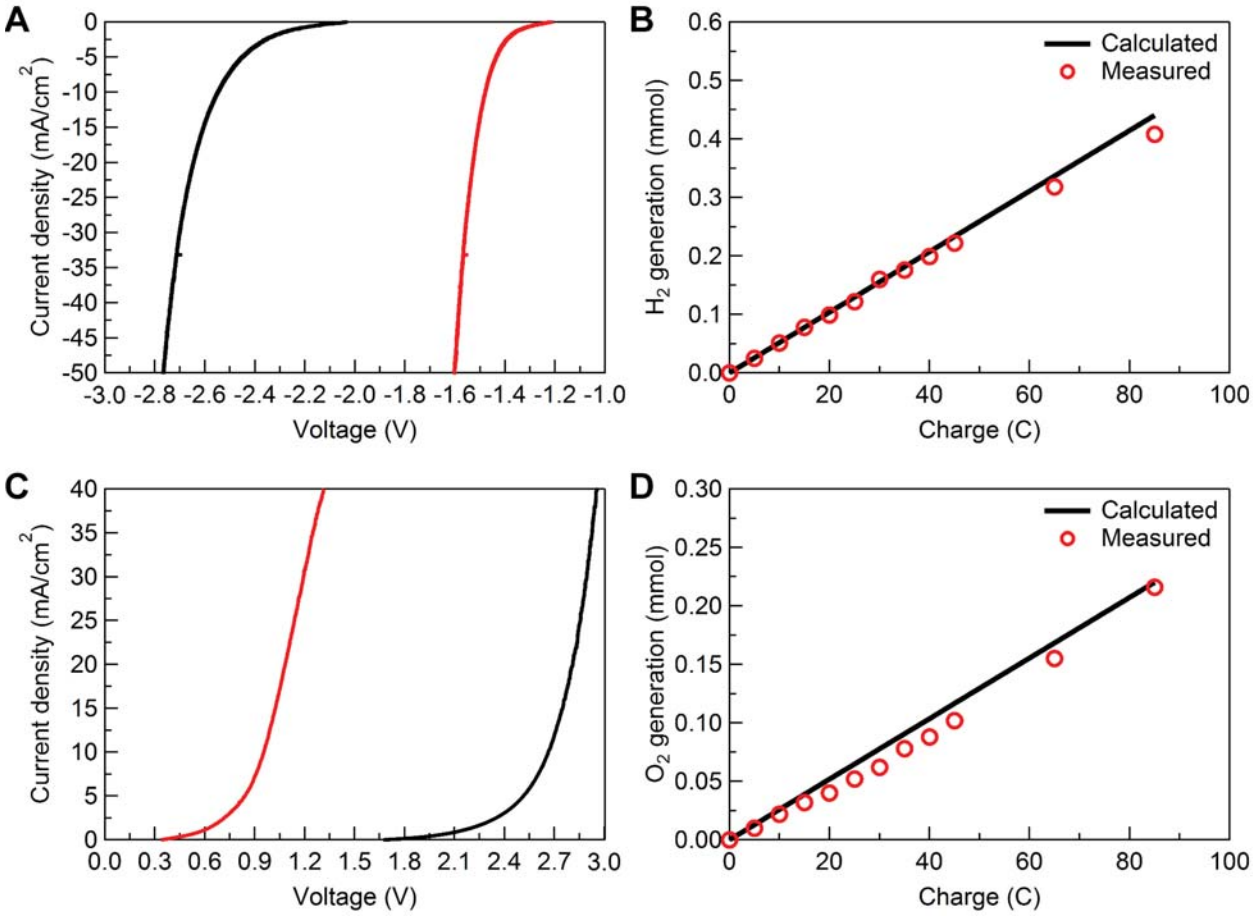

Figure 2. Electrochemical investigation of decoupled HER and OER with the assistance of FcNCl as an electron reservoir.
(A) Linear sweep voltammograms of Ni_2P/Ni/NF as the working electrode and carbon rod as the counter electrode with 0 (black) or 50 mM (red) FcNCl and 0.5 M Na_2SO_4 in the counter chamber and only 0.5 M Na_2SO_4 in the working compartment (scan rate = 5 mV s^{-1}, iR-corrected).
(B) Comparison of the GC-measured and theoretically calculated H_2 amounts during electrolysis at −1.8 V under (A)'s condition with FcNCl.
(C) Linear sweep voltammograms of NF as the working electrode and carbon rod as the counter electrode with 0 (black) or 50 mM (red) $FcNCl^+$ and 0.5 M Na_2SO_4 in the counter chamber and only 0.5 M Na_2SO_4 in the working compartment (scan rate = 5 mV s^{-1}, iR-corrected).
(D) Comparison of the GC-measured and theoretically calculated H_2 amounts during electrolysis at 1.7 V under (C)'s condition with $FcNCl^+$.

In order to evaluate the robustness of FcNCl as an electron reservoir for repeated HER and OER electrolysis, a long-term decoupled water electrolysis was conducted by alternating the applied voltage bias to the Ni_2P/Ni/NF and NF electrodes in 0.5 M Na_2SO_4; while the counter compartment was charged with a carbon electrode immersed in 10 mM FcNCl and 0.5 M Na_2SO_4.

By alternating the applied voltage bias of −1.6 V to Ni_2P/Ni/NF for H_2 evolution and 1.8 V to NF for O_2 production, we carried out the decoupled water electrolysis with each half cycle passing ~7 C charge before switching the applied bias. **Figure 3** displays the accumulated charge versus time for 20 successive cycles. At the beginning of each cycle, the pH of the electrolyte was 6.5. Upon the completion of the HER step, the pH value in the working compartment rose to 9, which decreased back to 6.5 once the OER step was finished. The similarity of these 20 charge versus time cycles indicated the robust cycling performance of FcNCl for repeated oxidation and reduction. Apparently, the generation of H_2 and O_2 periodically in the working compartment did not affect the reversible redox chemistry of FcNCl in the counter compartment. We also used NO_3^- as a counter ion to replace Cl^- in FcNCl. The change of counter ion did not affect the redox feature of FcN^- (**Figure S10**). The performance of $FcN(NO_3)$ as an electron reservoir for decoupled water electrolysis was comparable to that of FcNCl in **Figure S11**.

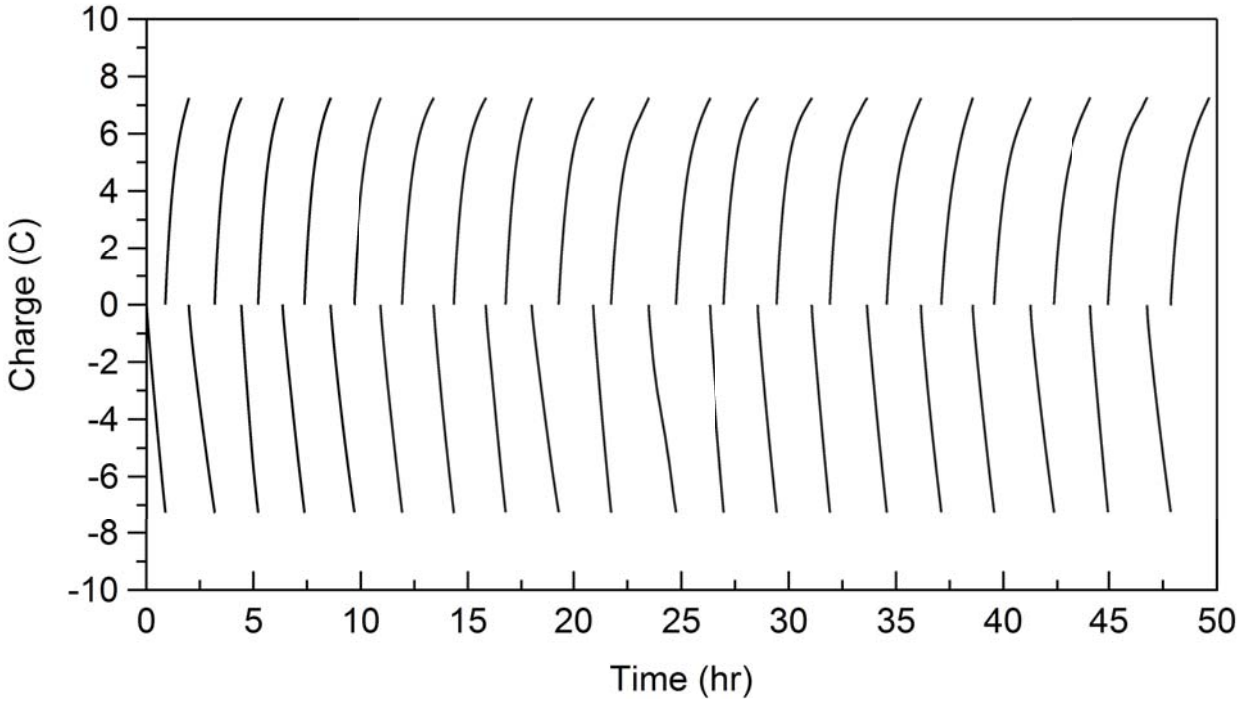

Figure 3. Electrolysis cycles of HER and OER to assess the stability of FcNCl as an electron reservoir. Charge evolution plot for repeated two-electrode water electrolysis cycles with 0.5 M Na_2O_4 in the working compartment and 10 mM FcNCl together with 0.5 M Na_2SO_4 in the counter compartment. Ni_2P/Ni/NF and NF were utilized as the HER and OER electrodes, respectively, in the working chamber and a carbon rod as the counter elelectrode in the counter chamber. Voltage bias between the working and counter electrodes were alternated at −1.6 V for HER and 1.8 V for OER, periodically. No iR correction was applied.

Solar-driven H_2 production decoupled from OER using FcNCl

Light-driven H_2 evolution from water splitting has been widely recognized as a promising approach to storing renewable solar energy in green chemical forms (*i.e.*, H_2).[7,21,23] By virtue of the remarkably reduced voltage input for decoupled water electrolysis using FcNCl as described above, it is feasible to conduct H_2 generation in near neutral solution under natural sunlight irradiation if a single photovoltaic (PV) module with small photovoltage is used as the external power source. Based on the aforementioned results, we reasoned that the combination of a PV cell (photovoltage > 1.4 V) and FcNCl would be able to drive HER without any external bias. Hence, a two-electrode H-type cell with the same configuration was connected with a commercial PV cell (~1.6 V, **Figure S12**) to assess our hypothesis. **Figure 4A** shows the linear sweep

voltammograms of HER collected on Ni_2P/Ni/NF in 0.5 M Na_2SO_4; while 10 mM FcNCl and 0.5 M Na_2SO_4 were loaded in the counter comparment with a carbon rod as the counter electrode. To reach a current density of −30 mA cm^{-2} for H_2 evolution, an external voltage bias of −1.58 V was required in the absence of natural sunlight irradiation. In contrast, when the solar cell was fully exposed to solar irradiation (intensity = 92 ± 5 mW cm^{-2}), the same current density could be achieved at zero external bias. **Figure 4B** displays the current evolution over time upon chopped solar irradiation, when the applied external bias was set at 0 V. When solar irradiation was not blocked, an immediate rise in cathodic current was observed, accompanied with vigorous H_2 bubble formation and release on the Ni_2P/NF working electrode. The periodic on and off catalytic HER current dependent on the sunlight exposure strongly supported the conclusion that the detected H_2 evolution was solely driven by sunlight irradiation. Control experiment under an identical condition but without FcNCl in the counter compartment demonstrated that FcNCl was crucial for this solar-driven decoupled H_2 evolution.

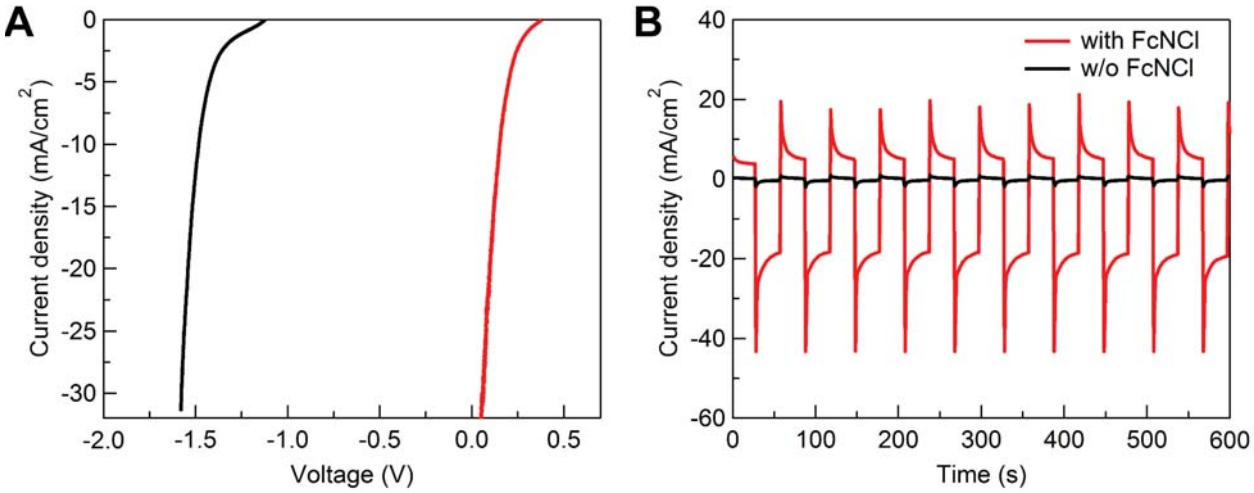

Figure 4. Electrocatalyic H_2 evolution with the assistance of a PV cell under natural sunlight irradiation. (A) Linear sweep voltammograms of HER on Ni_2P/Ni/NF in 0.5 M Na_2SO_4 with a carbon electrode in the counter chamber charged with 10 mM FcNCl and 0.5 M Na_2SO_4 with (red) and without (black) an external PV cell under sunlight irradiation (iR-corrected).
(B) Produced HER current density on Ni_2P/Ni/NF over time under chopped sunlight irradiation with no external voltage bias. Red curve: 10 mM FcNCl in the counter compartment. Black curve: No FcNCl was added in the counter compartment. No iR correction was applied.

Decoupled water splitting and organic oxidation using $Na_4[Fe(CN)_6]$

As demonstrated in the above discussion, the FcNCl electron reservoir is stable in the pH range of 5–9. To extend such new electrolyzer design to other applications, $Na_4[Fe(CN)_6]$ was also introduced as a proton-independent electron reservoir which is stable in a wider pH range from neutral to alkaline (1.0 M NaOH) conditions. $Na_4[Fe(CN)_6]$ is a low-cost chemical with relatively high solubility (0.6 M) in water and multiple industrial applications.[40] The electrochemical results demonstrate that $Na_4[Fe(CN)_6]$ possesses a suitable redox feature located between the onset potentials of HER and OER catalyzed by Co-P and Ni foam working electrodes, respectively (**Figures S13** – **S16**), with a large diffusion coefficient of 3.53×10^{-6} cm^2 s^{-1} and an electron transfer rate constant of 2.20×10^{-1} cm s^{-1} as well as remarkable robustness in 0.5 M Na_2SO_4 and 0.5 M sodium phosphate buffer (NaPi, pH = 7.0) electrolyte (**Figure S17**). The utilization of $Na_4[Fe(CN)_6]$ as an electron reservoir was proved to effectively split a large voltage input of one-step water splitting to two smaller voltage inputs for separate HER and OER processes with great cycling stability and a Faradic efficiency of 100 % under neutral condition (**Figures S18** – **S21**). The energy efficiency was calculated to be 64.6 %, comparable to other decoupled water splitting

systems in acidic or alkaline electrolytes (**Table S1**). In addition, PV cells with small photovoltages (1.1 or 1.6 V, **Figure S22**) were also able to drive decoupled water splitting under natural sunlight irradiation when $Na_4[Fe(CN)_6]$ was employed as the electron reservoir (**Figures S23** and **S24**).[7,23] Further optimization of the PV-electrolyzer design in terms of the sizes of PV panels and electrodes, concentrations of electron reservoir, and power densities of PV and electrolyzer, will be pursued to achieve high solar-to-H_2 efficiency.

As O_2 generated from water splitting is not a product of high value, we reasoned that it would be more economically attractive if our electron reservoir could be further utilized to promote HER and other organic upgrading reactions, such as electrochemical reforming of biomass-derived intermediates.[22, 41] For instance, 5-hydroxymethylfurfural (HMF) is an intermediate platform chemical produced from biomass materials which can be transformed to many value-added products.[42] Previous studies have demonstrated that HMF could be readily oxidized to more valuable 2,5-furandicarboxylic acid (FDCA) by nickel-based electrocatalysts under alkaline conditions.[43, 44] The electrochemical experiments of $Na_4[Fe(CN)_6]$ conducted in 1.0 M NaOH proved that its redox feature (1.3 V *vs.* RHE) was still positioned between the HER and OER onset potentials and less positive than the HMF oxidation on a Ni foam under the alkaline condition (**Figure S25**) with a diffusion coefficient of 4.70×10^{-6} cm^2 s^{-1} and an electron transfer rate constant of 8.45×10^{-2} cm s^{-1} (**Figure S26**), which were comparable to those reported values.[45] The negligible degradation during 1000 redox cycles of $Na_4[Fe(CN)_6]$ in 1.0 M NaOH further demonstrated its excellent stability.

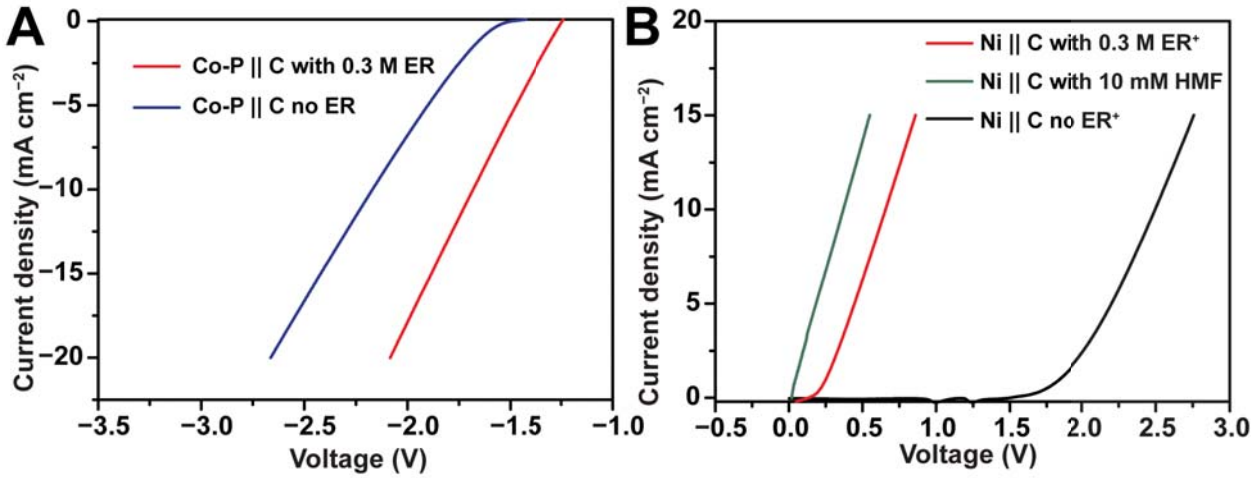

Figure 5. Electrochemical investigation of decoupled HER, OER and HMF oxidation with the assistance of $Na_4[Fe(CN)_6]$ as an electron reservoir.
(A) Linear sweep voltammograms of the two-electrode H-cell systems consisting of a Co-P working electrode and a carbon counter electrode with (red) or without (blue) 0.3 M $Na_4[Fe(CN)_6]$ (ER) in the counter compartment.
(B) Linear sweep voltammograms of the two-electrode H-cell systems consisting of a Ni foam working electrode and a carbon counter electrode under different conditions: neither $Na_3[Fe(CN)_6]$ (ER^+) nor HMF in both compartments (black); with 0.3 M ER^+ in the counter compartment (red); with 10 mM HMF in the working compartment and 0.3 M ER^+ in the counter compartment (green). The common electrolyte for all the above experiments was 1.0 M NaOH. All results were not iR-corrected.

Therefore, similar to decoupled water splitting, a two-compartment electrochemical cell with a cation exchange membrane was utilized for HER and HMF oxidation in 1.0 M NaOH (**Scheme 1c**). **Figure 5A** compares the linear sweep voltammogram (LSV) curves of a Co-P working

electrode for HER with and without 0.3 M $Na_4[Fe(CN)_6]$ in the counter compartment. The addition of the electron reservoir substantially shifted the LSV curve of HER towards positive direction. After the 0.3 M $Na_4[Fe(CN)_6]$ in the counter chamber had been oxidized after a chronocoulometry experiment, a LSV curve was collected on the Ni foam working electrode for OER (**Figure 5B**), which delivered 10 mA cm^{-2} at a voltage bias of 0.66 V. However, upon the addition of 10 mM HMF in the working chamber, a less positive onset potential was observed for HMF oxidation, achieving 10 mA cm^{-2} at a voltage bias of only 0.37 V. A chronocoulometry electrolysis for HMF oxidation was conducted at a voltage bias of 0.2 V. After passing 87 C charge, the conversion of HMF reached 100 %, resulting in the FDCA yield of 83% (**Figure S27**) without the need of noble metal catalysts that were widely used in previous reports.[46-48] It is anticipated that HER coupled with the electron reservoir oxidation can be driven by PV under the diurnal sunlight irradiation, while the electrocatalytic HMF oxidation is carried out at a small voltage (*e.g.*, 0.2 V) coupled with the electron reservoir regeneration at night with this novel electrolyzer design.[49] The exploration of new electron reservoirs with higher solubility is preferred in order to increase the capacitance of the electron reservoir solutions.

CONCLUSIONS

In summary, we have reported that a ferrocence-derived complex FcNCl could act as a robust and low-cost electron reservoir for decoupled water electrolysis under near neutral condition. Such a decoupling stratgegy enables H_2 and O_2 to be produced at different time and the production rate of one gas to be independent on the other, allowing fast H_2 production at elevated pressure without the concern of H_2/O_2 mixing. The reversible redox couple, high solubity, and great robustness of FcNCl in water make it feasible to conduct decoupled water electrolysis in near neutral water with earth-abundant electrocatalysts. Thanks to the substantially reduced voltage requirement for HER based on this decoupling approach, we further demonstrated that a PV cell with a small photovoltage (~1.6 V) was able to drive efficient H_2 evolution (~20 mA cm^{-2}) under natural sunlight irradiation without any external bias. Furthermore, we also introduced another electron reservoir, $Na_4[Fe(CN)_6]$, which is stable in a wider pH range from neural to alkaline conditions. The low cost, high solubility, remarkable robustness, and excellent redox properties of $Na_4[Fe(CN)_6]$ render itself an ideal electron reservoir not only for decoupled water splitting in neutral electrolyte but also for HER integrated with organic upgrading under alkaline conditions. This work offers attractive economic and safety advantages for sustainable H_2 production from water and also allows great flexibility in electrolyzer design for water electrolysis and electrocatalytic organic upgrading. This work will inspire researchers to explore novel electron reservoirs with lower cost, higher solubility, and better-positioned redox potential for decoupled water electrolysis and other promising electrocatalytic applications such as biocatalytic reactions, biomass valorization and seawater electrolysis.

SUPPLEMENTAL INFORMATION

Supplemental Information including detailed experimental procedures, 1 table and 27 figures can be found with this article online at http://dx.doi.org/

AUTHOR CONTRIBUTIONS

Y.S. designed and supervised the project, directed the research, analyzed and interpreted the data, and wrote the manuscript. W.L. and N.J. designed the methodology and conducted the experiments, prepared samples, analyzed and interpreted the data, and wrote the manuscript. W.L. and N.J. contributed equally to this work. B.H. and T.L.L. provided FcNCl and SELEMIONTM AMV membranes. X.L. contributed to SEM and elemental mapping measurements and assisted with sample preparation. F.S. assisted with XRD and some electrochemical measurements. G.H.

assisted with HPLC and GC experiments. T.J.J. and T.B.H. assisted with solar-driven water splitting experiments. All of the authors discussed the results and reviewed the manuscript.

ACKNOWLEDGEMETNS

We acknowledge the support of the National Science Foundation (CHE-1653978) and the Microscopy Core Facility at Utah State University. N.J. thanks the School of Graduate Studies Dissertation Fellowship of Utah State University.

REFERENCES AND NOTES

1 Lewis, N.S. and Nocera, D.G. (2006). Powering the planet: chemical challenges in solar energy utilization. Proc. Natl. Acad. Sci. U. S. A. *103*, 15729–15735.
2 Gray, H.B. (2009). Powering the planet with solar fuel. Nat. Chem. *1*, 7.
3 Cook, T.R., Dogutan, D.K., Reece, S.Y., Surendranath, Y., Teets, T.S., and Nocera, D.G. (2010). Solar energy supply and storage for the legacy and nonlegacy worlds. Chem. Rev. *110*, 6474–6502.
4 Walter, M.G., Warren, E.L., McKone, J.R., Boettcher, S.W., Mi, Q., Santori, E.A., and Lewis, N.S. (2010). Solar water splitting cells. Chem. Rev. *110*, 6446–6473.
5 Ursua, A., Gandia, L.M., and Sanchis, P. (2012). Hydrogen production from water electrolysis: current status and future trends. Proc. IEEE *100*, 410–426.
6 Carmo, M., Fritz, D.L., Mergel, J., and Stolten, D. (2013). A comprehensive review on PEM water electrolysis. Int. J. Hydrogen Energy *38*, 4901–4934.
7 Jia, J., Seitz, L.C., Benck, J.D., Huo, Y., Chen, Y., Ng, J.W.D., Bilir, T., Harris, J.S., and Jaramillo, T.F. (2016). Solar water splitting by photovoltaic-electrolysis with a solar-to-hydrogen efficiency over 30%. Nat. Commun. *7*, 13237.
8 Symes, M.D. and Cronin, L. (2013). Decoupling hydrogen and oxygen evolution during electrolytic water splitting using an electron-coupled-proton buffer. Nat. Chem. *5*, 403–409.
9 Chen, L., Dong, X., Wang, Y., and Xia, Y. (2016). Separating hydrogen and oxygen evolution in alkaline water electrolysis using nickel hydroxide. Nat. Commun. *7*, 11741.
10 Jin, J., Walczak, K., Singh, M.R., Karp, C., Lewis, N.S., and Xiang, C. (2014). An experimental and modeling/simulation-based evaluation of the efficiency and operational performance characteristics of an integrated, membrane-free, neutral pH solar-driven water-splitting system. Energy Environ. Sci. *7*, 3371–3380.
11 Berger, A., Segalman, R.A., and Newman, J. (2014). Material requirements for membrane separators in a water-splitting photoelectrochemical cell. Energy Environ. Sci. *7*, 1468–1476.
12 Bloor, L.G., Solarska, R., Bienkowski, K., Kulesza, P.J., Augustynski, J., Symes, M.D., and Cronin, L. (2016). Solar-driven water oxidation and decoupled hydrogen production mediated by an electron-coupled-proton buffer. J. Am. Chem. Soc. *138*, 6707–6710.
13 Barbir, F. (2005) PEM electrolysis for production of hydrogen from renewable energy sources. Sol. Energy *78*, 661–669.
14 Ghassemzadeh, L., Kreuer, K.-D., Maier, J., and Müller, K. (2010). Chemical degradation of Nafion membranes under mimic fuel cell conditions as investigated by solid-state NMR spectroscopy. J. Phys. Chem. C *114*, 14635–14645.
15 Prabhakaran, V., Arges, C.G., and Ramani, V. (2012). Investigation of polymer electrolyte membrane chemical degradation and degradation mitigation using in situ fluorescence spectroscopy. Proc. Natl. Acad. Sci. U. S. A. *109*, 1029–1034.
16 Rausch, B., Symes, M. D., and Cronin, L. (2013). A bio-inspired, small molecule electron-coupled-proton buffer for decoupling the half-reactions of electrolytic water splitting. J. Am. Chem. Soc. *135*, 13656–13659.
17 Amstutz, V., Toghill, K.E., Powlesland, F., Vrubel, H., Comninellis, C., Hu, X., and Girault, H.H. (2014). Renewable hydrogen generation from a dual-circuit redox flow battery. Energy Environ. Sci. *7*, 2350–2358.
18 Peljo, P., Vrubel, H., Amstutz, V., Pandard, J., Morgado, J., Santasalo-Aarnio, A., Lloyd, D., Gumy, F., Dennison, C.R., Toghill, K.E., and Girault, H.H. (2016). Green Chem. All-vanadium dual circuit redox flow battery for renewable hydrogen generation and desulfurization. *18*, 1785–1797.

19 Moreno-Hernandez I.A., MacFarland, C.A., Read, C.G., Papadantonakis, K.M., Brunschwig, B.S., Lewis, N.S. (2017). Crystalline nickel manganese antimonate as a stable water-oxidation catalyst in aqueous 1.0 M H_2SO_4. Energy Environ. Sci. *10*, 2103–2108.
20 Xiang, C., Papadantonakis, K.M., and Lewis, N.S. (2016). Principles and implementations of electrolysis systems for water splitting. Mater. Horiz. *3*, 169–173.
21 Landman, A., Dotan, H., Shter, G.E., Wullenkord, M., Houaijia, A., Maljusch, A., Grader, G.S., and Rothschild, A. (2017). Photoelectrochemical water splitting in separate oxygen and hydrogen cells. Nat. Mater. *16*, 646–651.
22 Chen, Y.X., Lavacchi, A., Miller, H.A., Bevilacqua, M., Filippi, J., Innocenti, M., Marchionni, A., Oberhauser, W., Wang, L., and Vizza, F. (2014). Nanotechnology makes biomass electrolysis more energy efficient than water electrolysis. Nat. Commun. *5*, 4036.
23 Luo, J., Im, J.-H., Mayer, M.T., Schreier M., Nazeeruddin, M.K., Park, N.-G., Tilley, S.D., Fan, H.J., and Grätzel, M. (2014). Water photolysis at 12.3% efficiency via perovskite photovoltaics and Earth-abundant catalysts. Science *345*, 1593–1596.
24 Sakimoto, K.K., Wong, A.B., and Yang, P. (2016). Self-photosensitization of nonphotosynthetic bacteria for solar-to-chemical production. Science *351*, 74–77.
25 Liu, C., Colón, B.C., Ziesack, M., Silver, P.A., and Nocera, D.G. (2016). Water splitting–biosynthetic system with CO_2 reduction efficiencies exceeding photosynthesis. Science *352*, 1210–1213.
26 Liu, C., Gallagher, J.J., Sakimoto, K.K., Nichols, E.M., Chang, C.J., Chang, M.C.Y., and Yang, P. (2015). Nanowire−bacteria hybrids for unassisted solar carbon dioxide fixation to value-added chemicals. Nano Lett. *15*, 3634–3639.
27 Nichols, E.M., Gallagher, J.J., Liu, C., Su, Y., Resasco, J., Yu, Y., Sun, Y., Yang, P., Chang, M.C.Y., and Chang, C.J. (2015). Hybrid bioinorganic approach to solar-to-chemical conversion. Proc. Natl. Acad. Sci. U. S. A. *112*, 11461–11466.
28 Hu, B., DeBruler, C., Rhodes, Z., and Liu, T.L. (2017) Long-cycling aqueous organic redox flow battery (AORFB) toward sustainable and safe energy storage. J. Am. Chem. Soc. *139*, 1207–1214.
29 Li, W., Gao, X., Xiong, D., Xia, F., Liu, J., Song, W.-G., Xu, J., Thalluri, S.M., Cerqueira, M.F., Fu, X., et al. (2017). Vapor-solid synthesis of monolithic single-crystalline CoP nanowire electrodes for efficient and robust water electrolysis. Chem. Sci. *8*, 2952–2958.
30 Burke, M.S., Kast, M.G., Trotochaud, L., Smith, A.M., and Boettcher, S.W. (2015). Cobalt–iron (oxy)hydroxide oxygen evolution electrocatalysts: the role of structure and composition on activity, stability, and mechanism. J. Am. Chem. Soc. *137*, 3638–3648.
31 Li, W., Gao, X., Xiong, D., Wei, F., Song, W.-G., Xu, J., and Liu, L. (2017). Hydrothermal synthesis of monolithic Co_3Se_4 nanowire electrodes for oxygen Evolution and overall water splitting with high efficiency and extraordinary catalytic stability. Adv. Energy Mater. *7*, 1602579.
32 Burke, M.S.; Zou, S., Enman, L.J., Kellon, J.E., Gabor, C A., Pledger, E., and Boettcher, S.W. (2015). Revised oxygen evolution reaction activity trends for first-row transition-metal (oxy)hydroxides in alkaline media. J. Phys. Chem. Lett. *6,* 3737–3742.
33 Li, W., Gao, X., Wang, X., Xiong, D., Huang, P.-P., Song, W.-G., Bao, X., and Liu, L. (2016). From water reduction to oxidation: Janus Co-Ni-P nanowires as high-efficiency and ultrastable electrocatalysts for over 3000 h water splitting. J. Power Sources *330*, 156–166.
34 You, B., Liu, X., Hu, G., Gul, S., Yano, J., Jiang, D. E., and Sun, Y. (2017). Universal surface engineering of transition metals for superior electrocatalytic hydrogen evolution in neutral water. J. Am. Chem. Soc., *139*, 12283–12290.
35 Li, W., Xiong, D., Gao, X., Song, W.-G., Xia, F., and Liu, L. (2017). Self-supported Co-Ni-P ternary nanowire electrodes for highly efficient and stable electrocatalytic hydrogen evolution in acidic solution. Catal. Today, *287*, 122–129.
36 Li, W., Wang, X., Xiong, D., and Liu, L. (2016). Efficient and durable electrochemical hydrogen evolution using cocoon-like MoS_2 with preferentially exposed edges. Int. J. Hydrogen Energy, *41*, 9344–9354.
37 Rausch, B., Symes, M.D., Chisholm, G., and Cronin, L. (2014). Decoupled catalytic hydrogen evolution from a molecular metal oxide redox mediator in water splitting. Science *345*, 1326–1330.
38 Bockris, J., Conway, B., Yeager, E., and White, R. (1981). Comprehensive treatise of electrochemistry: electrochemical processing (Plenum Press).
39 Qi, Z. (2013). Proton exchange membrane fuel cells (CRC Press).

40 Grieken, R., Aguado, J., López-Muñoz, M.-J., and Marugán, J. (2005). Photocatalytic degradation of iron-cyanocomplexes by TiO_2 based catalysts. Appl. Catal. B-Environ. *55*, 201–211.
41 Cha, H.G., and Choi, K.-S. (2015). Combined biomass valorization and hydrogen production in a photoelectrochemical cell. Nat. Chem. *7*, 328–333.
42 Zhang, Z., and Deng, K. (2015). Recent advances in the catalytic synthesis of 2,5-furandicarboxylic acid and its derivatives. ACS Catal. *5*, 6529–6544.
43 You, B., Liu, X., Jiang, N., and Sun, Y. (2016). A general strategy for decoupled hydrogen production from water splitting by integrating oxidative biomass valorization. J. Am. Chem. Soc. *138*, 13639–13646.
44 You, B., Jiang, N., Liu, X., and Sun, Y. (2016). Simultaneous H_2 generation and biomass upgrading in water by an efficient noble-metal-free bifunctional electrocatalyst. Angew. Chem. Int. Ed. *55*, 9913–9917.
45 Gong, K., Xu, F., Grunewald, J.B., Ma, X., Zhao, Y., Gu, S., and Yan, Y. (2016). All-soluble all-iron aqueous redox-flow battery. ACS Energy Lett. *1*, 89–93.
46 Davis, S.E., Houk, L.R., Tamargo, E.C., Datye, A.K., and Davis, R.J. (2011). Oxidation of 5-hydroxymethylfurfural over supported Pt, Pd and Au catalysts. Catal. Today *160*, 55–60.
47 Gorbanev, Y.Y., Klitgaard, S.K., Woodley, J.M., Christensen, C.H., and Riisager, A. (2009). Gold-catalyzed aerobic oxidation of 5-hydroxymethylfurfural in water at ambient temperature. ChemSusChem *2*, 672–675.
48 Chen, C., Yu, Y., Li, W., Cao, C., Li, P., Dou, Z., and Song, W. (2011). Mesoporous $Ce_{1-x}Zr_xO_2$ solid solution nanofibers as high efficiency catalysts for the catalytic combustion of VOCs. J. Mater. Chem. *21*, 12836–12841
49 Mallouk, T.E. (2013). Water electrolysis: divide and conquer. Nat. Chem. *5*, 362–363.

Main figure and scheme titles and legends

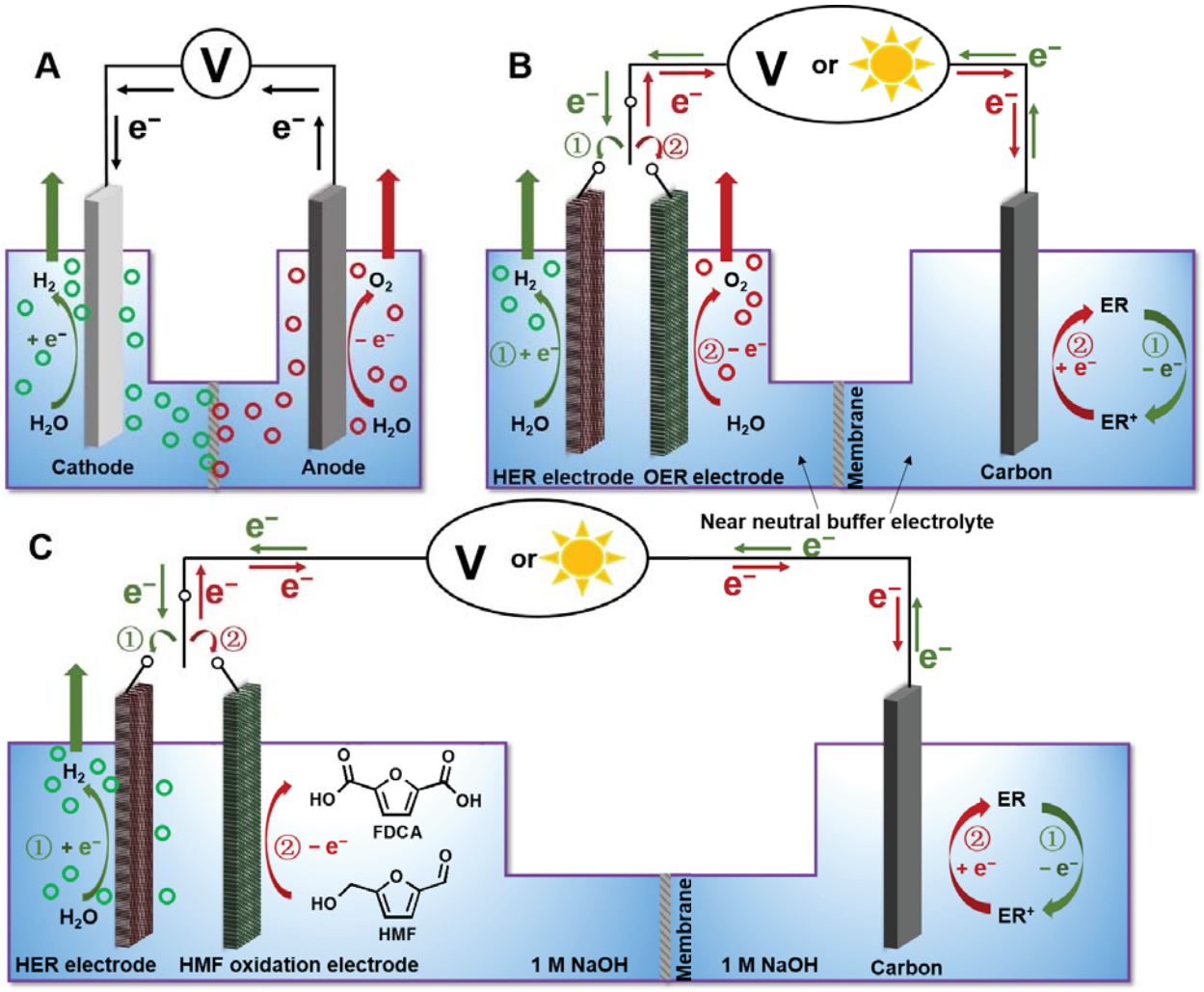

Scheme 1. Schematic illustration of electrolyzer designs.
(A) Conventional electrolyzer for one-step full water splitting.
(B) A new electrolyzer design for decoupled water splitting with stepwise HER and OER in near neutral electrolyte, wherein two working electrodes are alternatively utilized in the working compartment while a carbon electrode is used in the counter compartment containing an electron reservoir of either FcNCl or $Na_4[Fe(CN)_6]$.
(C) A new electrolyzer design for stepwise HER and organic oxidation in alkaline electrolyte (1 M NaOH). $Na_4[Fe(CN)_6]$ is introduced in the counter chamber with a carbon electrode.
For (B) and (C), ER and ER^+ denote the reduced (*i.e.*, FcNCl or $[Fe(CN)_6]^{4-}$) and oxidized (*i.e.*, $FcNCl^+$ or $[Fe(CN)_6]^{3-}$) forms of the adopted electron reservoir, respectively.

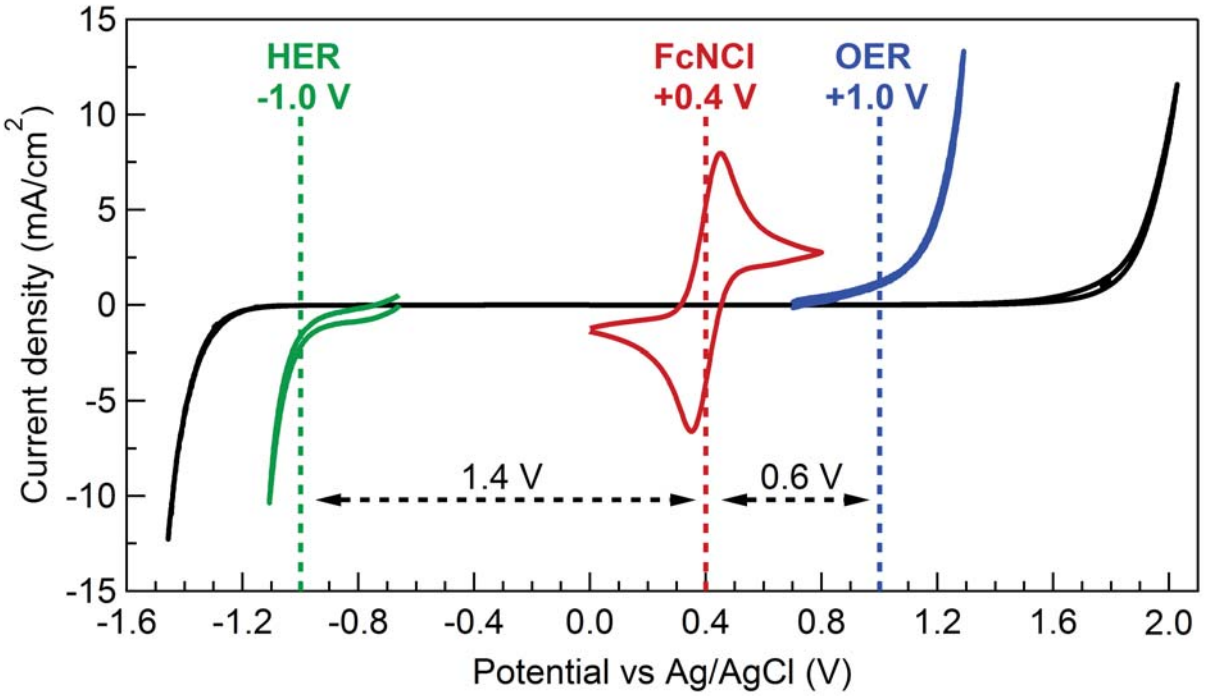

Figure 1. Comparison of the cyclic voltammograms of FcNCl, HER, and OER under near neutral condition. All the CV curves were collected in a three-electrode configuration in 0.5 M Na_2SO_4 (pH = 6.5) using Ag/AgCl (sat. KCl) as the reference electrode. Cyclic voltammogram of 50 mM FcNCl (red) was collected at a scan rate of 100 mV s^{-1} with a glassy carbon working electrode and carbon counter electrode. Cyclic voltammograms of HER (black) and OER (black) were collected on bare glassy carbon electrodes at a scan rate of 5 mV s^{-1} (iR-corrected). Cyclic voltammograms (iR-corrected) of HER on Ni_2P/Ni/NF (green) and OER on nickel foam (blue) were collected at a scan rate of 5 mV s^{-1} with a carbon counter electrode.

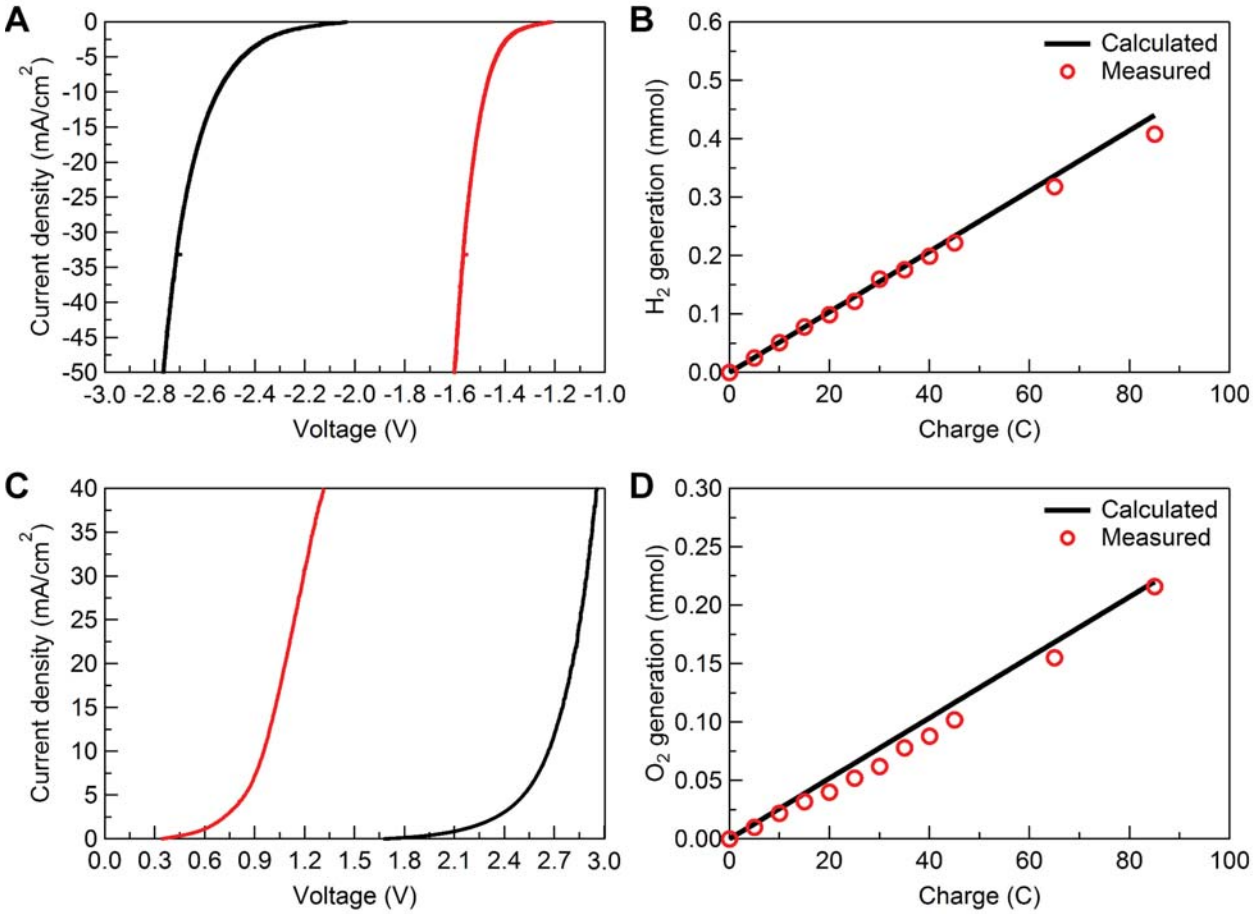

Figure 2. Electrochemical investigation of decoupled HER and OER with the assistance of FcNCl as an electron reservoir.

(A) Linear sweep voltammograms of Ni_2P/Ni/NF as the working electrode and carbon rod as the counter electrode with 0 (black) or 50 mM (red) FcNCl and 0.5 M Na_2SO_4 in the counter chamber and only 0.5 M Na_2SO_4 in the working compartment (scan rate = 5 mV s^{-1}, iR-corrected).

(B) Comparison of the GC-measured and theoretically calculated H_2 amounts during electrolysis at −1.8 V under (A)'s condition with FcNCl.

(C) Linear sweep voltammograms of NF as the working electrode and carbon rod as the counter electrode with 0 (black) or 50 mM (red) $FcNCl^+$ and 0.5 M Na_2SO_4 in the counter chamber and only 0.5 M Na_2SO_4 in the working compartment (scan rate = 5 mV s^{-1}, iR-corrected).

(D) Comparison of the GC-measured and theoretically calculated H_2 amounts during electrolysis at 1.7 V under (C)'s condition with $FcNCl^+$.

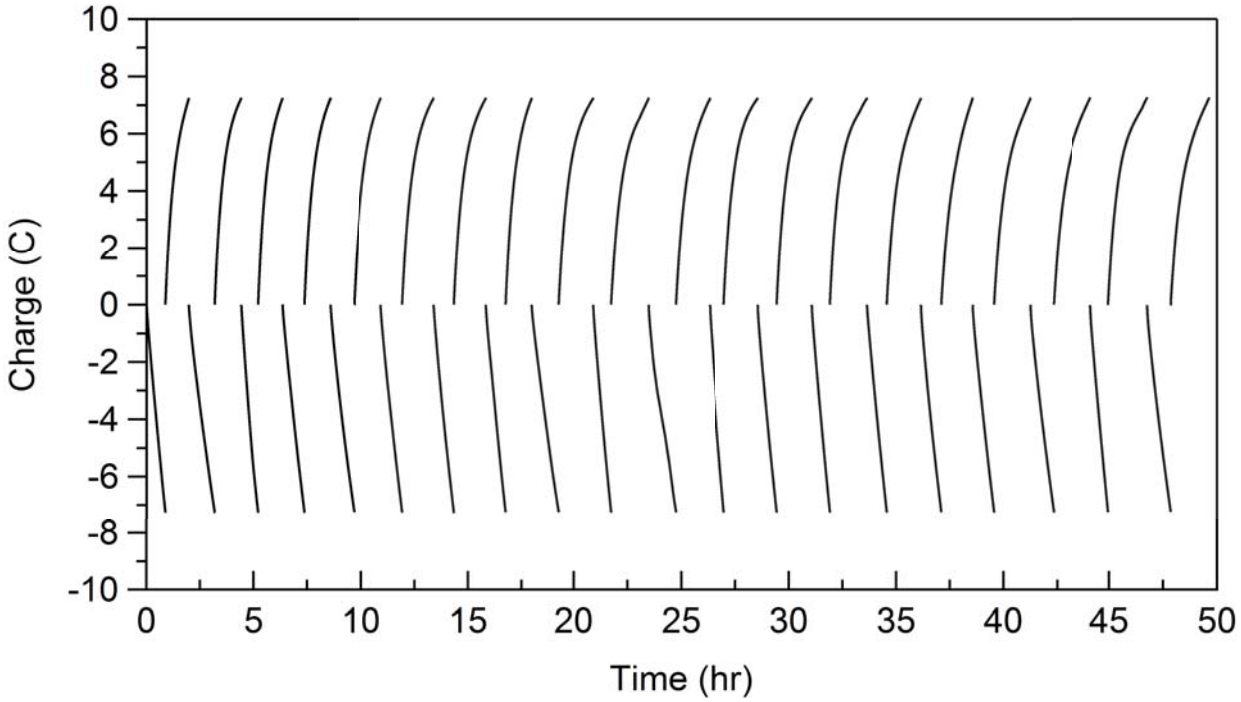

Figure 3. Electrolysis cycles of HER and OER to assess the stability of FcNCl as an electron reservoir. Charge evolution plot for repeated two-electrode water electrolysis cycles with 0.5 M Na_2O_4 in the working compartment and 10 mM FcNCl together with 0.5 M Na_2SO_4 in the counter compartment. Ni_2P/Ni/NF and NF were utilized as the HER and OER electrodes, respectively, in the working chamber and a carbon rod as the counter elelectrode in the counter chamber. Voltage bias between the working and counter electrodes were alternated at −1.6 V for HER and 1.8 V for OER, periodically. No iR correction was applied.

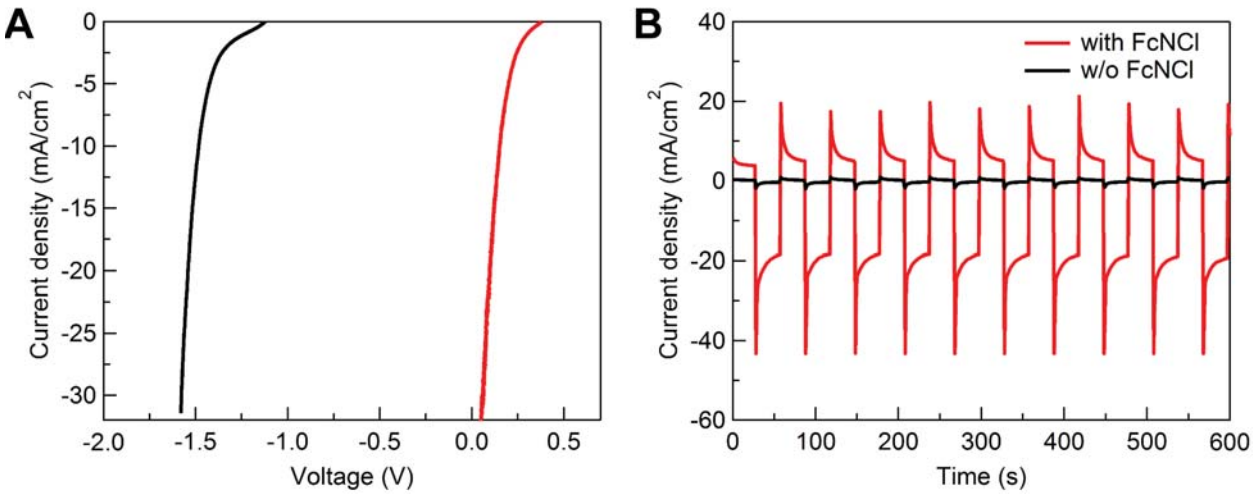

Figure 4. Electrocatalyic H_2 evolution with the assistance of a PV cell under natural sunlight irradiation. (A) Linear sweep voltammograms of HER on Ni_2P/Ni/NF in 0.5 M Na_2SO_4 with a carbon electrode in the counter chamber charged with 10 mM FcNCl and 0.5 M Na_2SO_4 with (red) and without (black) an external PV cell under sunlight irradiation (iR-corrected).
(B) Produced HER current density on Ni_2P/Ni/NF over time under chopped sunlight irradiation with no external voltage bias. Red curve: 10 mM FcNCl in the counter compartment. Black curve: No FcNCl was added in the counter compartment. No iR correction was applied.

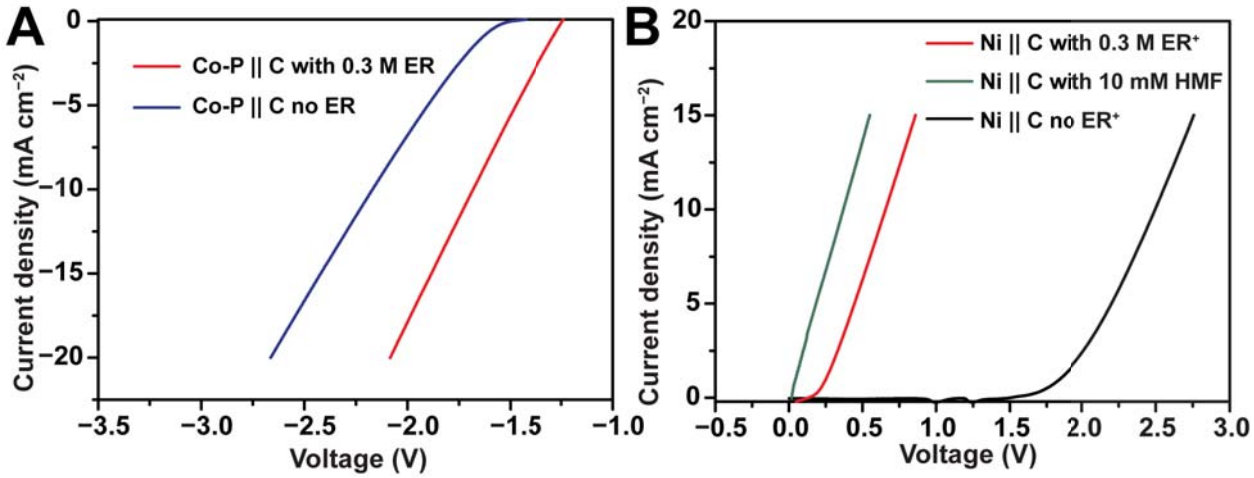

Figure 5. Electrochemical investigation of decoupled HER, OER and HMF oxidation with the assistance of $Na_4[Fe(CN)_6]$ as an electron reservoir.
(A) Linear sweep voltammograms of the two-electrode H-cell systems consisting of a Co-P working electrode and a carbon counter electrode with (red) or without (blue) 0.3 M $Na_4[Fe(CN)_6]$ (ER) in the counter compartment.
(B) Linear sweep voltammograms of the two-electrode H-cell systems consisting of a Ni foam working electrode and a carbon counter electrode under different conditions: neither $Na_3[Fe(CN)_6]$ (ER^+) nor HMF in both compartments (black); with 0.3 M ER^+ in the counter compartment (red); with 10 mM HMF in the working compartment and 0.3 M ER^+ in the counter compartment (green). The common electrolyte for all the above experiments was 1.0 M NaOH. All results were not iR-corrected.

I. Supplemental Experimental Procedures

II. Supplemental Figures

Figure S1. SEM images of the pristine Ni foam (NF) and the prepared Ni_2P/Ni/NF electrocatalyst.

Figure S2. XRD patterns of Ni foam and Ni_2P/Ni/NF.

Figure S3. Three-electrode electrochemical results of FcNCl electron reservoir in 0.5 M Na_2SO_4.

Figure S4. Rotating disk electrode electrochemical results of FcNCl electron reservoir in 0.5 M Na_2SO_4.

Figure S5. Gas chromatography results of produced gases in decoupled water electrolysis.

Figure S6. Polarization curve of Ni_2P/Ni/NF || NF two-electrode system for direct overall water splitting in 0.5 M Na_2SO_4.

Figure S7. Electrochemical investigation of decoupled HER and OER with the assistance of FcNCl as an electron reservoir in 0.1 M potassium hydrogen phthalate buffer and 0.5 M Na_2SO_4 (pH = 5).

Figure S8. Electrochemical investigation of decoupled HER and OER with the assistance of FcNCl as an electron reservoir in 0.1 M phosphate buffer and 0.5 M Na_2SO_4 (pH = 7).

Figure S9. Electrochemical investigation of decoupled HER and OER with the assistance of FcNCl as an electron reservoir in 0.1 M sodium borate buffer and 0.5 M Na_2SO_4 (pH = 9).

Figure S10. Cyclic voltammogram of 30 mM $FcN(NO_3)$ in 0.5 M Na_2SO_4.

Figure S11. Electrochemical investigation of decoupled HER and OER with the assistance of $FcN(NO_3)$ as an electron reservoir in 0.5 M Na_2SO_4.

Figure S12. Current-voltage curves of the PV cell used for driving decoupled water splitting in 0.5 M Na_2SO_4 solution with 10 mM FcNCl under the sunlight irradiation.

Figure S13. Linear sweep voltammograms of carbon working electrode for HER and OER, Co-P working electrode for HER, and Ni foam working electrode for OER in 0.5 M Na_2SO_4 and 0.5 M NaPi (pH = 7.0) and cyclic voltammogram of 0.3 M $Na_4[Fe(CN)_6]$ (ER).

Figure S14. XRD patterns of Co-P and Ni foam electrodes.

Figure S15. SEM images and EDX result of Co-P electrode.

Figure S16. SEM images of Ni foam.

Figure S17. Three-electrode electrochemical results of $Na_4[Fe(CN)_6]$ electron reservoir in 0.5 M Na_2SO_4 and 0.5 M NaPi (pH = 7.0).

Figure S18. Decoupled water electrolysis results with Co-P for HER and Ni foam for OER in the presence of $[Fe(CN)_6]^{4-}$/$[Fe(CN)_6]^{3-}$ electron reservoir in 0.5 M Na_2SO_4 and 0.5 M NaPi buffer (pH = 7.0).

Figure S19. Gas chromatography results of produced gases in decoupled water electrolysis.

Figure S20. Multiple sequential bulk electrolysis cycles of the two-electrode systems (Co-P || carbon, or Ni foam || carbon) with $[Fe(CN)_6]^{4-}$/$[Fe(CN)_6]^{3-}$ electron reservoir for decoupled water splitting.

Figure S21. CV curves of 0.3 M $Na_4[Fe(CN)_6]$ in 0.5 M Na_2SO_4 and 0.5 M NaPi (pH = 7.0) for 1000 cycles.

Figure S22. Current-voltage curves of the PV cells used for solar-driven decoupled water splitting with 0.3 M $Na_4[Fe(CN)_6]$ electron reservoir in 0.5 M Na_2SO_4 and 0.5 M NaPi (pH = 7.0).

Figure S23. Solar-driven decoupled water electrolysis results in neutral electrolyte with $[Fe(CN)_6]^{4-}/[Fe(CN)_6]^{3-}$ electron reservoir.

Figure S24. Nyquist plots of Co-P and Ni foam working electrodes in neutral electrolyte.

Figure S25. Polarization curves of carbon electrode, Ni foam and Co-P electrode, and CV curve of 0.3 M of $Na_4[Fe(CN)_6]$ electron reservoir in 1 M NaOH.

Figure S26. Three-electrode electrochemical results of $Na_4[Fe(CN)_6]$ electron reservoir in 1 M NaOH.

Figure S27. Concentration of HMF precursor and its oxidation products during the electrochemical oxidation and reaction pathways.

III. Supplemental Table

Table S1. Comparison of our electron reservoir-mediated decoupled water electrolyzers with reported decoupled water splitting systems with redox mediators.

IV. Supplemental References

I. Supplemental Experimental Procedures

Materials.
Deionized water (18 MΩ·cm) was produced by a Barnstead E-Pure system and used in all experiments. $CoCl_2·6H_2O$ was purchased from Sigma-Aldrich. NH_4Cl, $NiCl_2·6H_2O$, Na_2SO_4, $NaH_2PO_4·H_2O$, Na_2HPO_4, and NaOH were purchased from Fisher Chemical. $Na_4[Fe(CN)_6]·10H_2O$ was purchased from Acros Organics. $NaH_2PO_2·H_2O$ was acquired from Alfa Aesar. (Ferrocenylmethyl)dimethylamine, methyl chloride, acetonitrile and diethyl ether were purchased from Sigma-Aldrich. Ni foam (> 99.99%, 80–110 pores per inch) and Co foam (> 99.99%, 110 pores per inch) were purchased from MTI and Hezhe Jiaotong Group, respectively. HCl was purchased from Pharmco-Aaper. 5-Hydroxymethylfurfural (HMF), 2,5-diformylfuran (DFF) and 2-formyl-5-furancarboxylic acid (FFCA) were purchased from Ark Pharm. 2,5-Furandicarboxylic acid (FDCA) was purchased from Chem-Impex International. 5-Hydroxymethyl-2-furan-carboxylic acid (HMFCA) was purchased from Asta Tech. Anion exchange membrane (SELEMION™, AMV 120 μm) was purchased from AGC Chemicals. Cation exchange membrane (Nafion, NR-212) was purchased from Fuel Cell Store. All chemicals were used as received without purification.

Synthesis of (ferrocenylmethyl)trimethylammonium chloride (FcNCl)
FcNCl was prepared according to a reported method.[S1] A Schlenk flask (250 mL) was maintained under N_2. (Ferrocenylmethyl)dimethylamine (20 g, 82.3 mmol) and methyl chloride (1 M in tert-butylether, 90 mL) were added to CH_3CN (50 mL) in the Schlenk flask. The reaction mixture was stirred at room temperature overnight. The orange precipitate was collected by filtration. Diethyl ether (100 mL) was added into the supernatant solution to precipitate a second crop of the product. The product was rinsed with diethyl ether (40 mL) twice and dried under vacuum.

Synthesis of $FcN(NO_3)$
$FcN(NO_3)$ was prepared via the reaction between FcNCl and $AgNO_3$. FcNCl (1 mmol) was dissolved in water (150 mL). $AgNO_3$ (1 mmol) was also dissolved into water (20 mL). FcNCl solution was stirred at room temperature; while $AgNO_3$ solution was added slowly and dropwisely to the FcNCl solution. Then, the AgCl precipitate was removed through filtration and $FcN(NO_3)$ was obtained via rotary evaporation at 30°C.

Preparation of Ni_2P/Ni/NF.
The electrodeposition of porous Ni microspheres on nickel foam (Ni/NF) was performed in a standard two-electrode configuration at room temperature with an aqueous electrolyte consisting of NH_4Cl (2.0 M) and $NiCl_2$ (0.1 M). A piece of commercial nickel foam (0.5 cm × 0.5 cm) was used as the working electrode and a carbon rod was used as the counter electrode. The electrodeposition was carried out at a constant current of −1.0 A cm^{-2} for 500 s to obtain Ni/NF samples. Subsequently, the resulting Ni/NF was placed in the center of a tube furnace, and $NaH_2PO_2·H_2O$ (1.0 g) was placed at the upstream side and near Ni/NF. After flushing with Ar gas, the center of the furnace was quickly elevated to 400°C with a ramping rate of 10°C min^{-1} and kept at this temperature for 2 h to convert the metallic nickel to nickel phosphides, resulting in the formation of Ni_2P/Ni/NF. The as-prepared Ni_2P/Ni/NF was stored under vacuum at room temperature and directly used for electrochemical experiments without any further treatment.

Preparation of the Co-P Electrode.
The Co-P working electrodes were prepared by electrodeposition of Co particles on Co foams followed by thermal phosphorization. Typically, a piece of Co foam was cleaned by ultrasonication in 6 M HCl for 10 min, subsequently rinsed with water and ethanol, and finally dried under N_2 at room temperature. Then the cleaned Co foam was used as the working electrode and a carbon rod was used as the counter electrode. The electrolyte was 0.1 M $CoCl_2$ and 2.0 M NH_4Cl mixture solution and deaerated by N_2 bubbling. The electrodeposition was performed in a two-electrode configuration at a constant current density of −0.5 A cm^{-2} for 1000 s under N_2 protection without stirring. The resultant Co-deposited Co foam was loaded in a ceramic boat, with 10.0 g of $NaH_2PO_2·H_2O$ placed 2 cm away in the upstream side. The ceramic boat was placed in a horizontal tube furnace and purged with Ar gas (99.999 %) for 1 h. Afterwards, it was heated to 400°C at a ramping rate of 5 °C min^{-1} and maintained at 400°C for 2 h. Finally, the furnace was naturally cooled down to room temperature. The Ar flow was kept throughout the whole process. The final Co-P electrode was washed with water and ethanol, dried under N_2 and stored in a vacuum desiccator for further

use. The Ni foam working electrode was a piece of commercial Ni foam, which was cleaned and dried in the similar procedure as for the Co foam.

Electrochemical Measurements.

For the studies of $Na_4[Fe(CN)_6]$, three-electrode linear sweep voltammogram (LSV) and cyclic voltammogram (CV) experiments were conducted on a CHI760E electrochemical workstation (CH Instruments). Deaerated 0.5 M Na_2SO_4 and 0.5 M sodium phosphate buffer (NaPi) mixture solution (pH = 7.0) was used as the neutral electrolyte to eliminate the possible pH gradient, while 1 M NaOH was used as the alkaline electrolyte. The synthesized Co-P electrode and Ni foam electrode were used as the working electrodes for HER and OER, respectively. A carbon electrode (spectro-grade carbon rod, Electron Microscopy Sciences) and a calibrated Ag/AgCl (3 M NaCl, BASi) electrode were used as the counter and reference electrodes, respectively. Unless stated otherwise, all potentials are reported versus reversible hydrogen electrode (RHE) by converting the potentials measured versus Ag/AgCl (3 M NaCl) according to the following equation:

$$E(vs.\ \text{RHE}) = E(vs.\ \text{Ag/AgCl}) + 0.209 + 0.059 \times \text{pH} \quad (1)$$

The current density presented in this work is normalized with respect to the geometric surface area of each working electrode. For HER studies, the Co-P electrode was firstly conditioned by CV scans from 0.05 to −0.6 V *vs.* RHE at 5 mV s^{-1}. The steady-state LSV curve of the Co-P electrode was then obtained by scanning from negative to positive potential at 5 mV s^{-1}. For OER studies, the Ni foam electrode was conditioned by repetitive CV scans at 5 mV s^{-1} in the potential window from 0.7 to 2.2 V *vs*. RHE. Afterwards, the steady-state LSV curve of the Ni foam electrode was obtained by scanning from positive to negative potential at 5 mV s^{-1}. For comparison, the electrocatalytic performance of the carbon electrode for HER and OER was also measured under the same conditions. Unless stated otherwise, all LSV polarization curves measured in the three-electrode configuration are iR-corrected. The correction was made according to the following equation:

$$E_{\text{corrected}} = E_{\text{measured}} - iR_s \quad (2)$$

where $E_{\text{corrected}}$ is the iR-corrected potential, E_{measured} and i are experimentally measured potential and current, respectively, and R_s is the equivalent series resistance measured by electrochemical impedance spectroscopy (EIS) in the frequency range of 10^6 – 0.1 Hz with an amplitude of 10 mV.

The diffusion and electron transfer properties of $Na_4[Fe(CN)_6]$ were studied by using CV in a three-electrode configuration. A polished glassy carbon electrode (GCE, area = 0.07065 cm^2) was used as the working electrode. A carbon rod and a calibrated Ag/AgCl (3 M NaCl) electrode were used as the counter and reference electrodes, respectively. The electrolyte consisted of 0.01 or 0.3 M $Na_4[Fe(CN)_6]$ in 0.5 M Na_2SO_4 and 0.5 M NaPi, or 1 M NaOH deaerated by N_2 bubbling. The CV curves of $Na_4[Fe(CN)_6]$ over GCE were collected within 0 – 0.6 V *vs.* Ag/AgCl (3 M NaCl) at varying scan rates from 10 to 4000 mV s^{-1} without stirring but under N_2 protection. LSV measurements on the rotating disk electrode (RDE) were performed by using a RRDE-3A apparatus (ALS Co., Ltd) in a similar three-electrode configuration except for a polished glassy carbon RDE (area = 0.07065 cm^2) used as the working electrode. The electrolyte was composed of 10 mM $Na_4[Fe(CN)_6]$ in 0.5 M Na_2SO_4 and 0.5 M NaPi or 1 M NaOH deaerated by N_2 bubbling. LSV curves were recorded at a scan rate of 5 mV s^{-1} with the rotation rate varying from 400 to 4000 rpm. The limiting currents were plotted against the square root of the rotation rate (rad s^{-1}). The data were fitted to a linear Levich plot, resulting in the Levich plot slope.[S1] The diffusion coefficient of $Na_4[Fe(CN)_6]$ was calculated based on the following equation:

$$\text{Levich plot slope} = 0.62nFAC_0D^{2/3}\upsilon^{1/6} \quad (3)$$

where n = 1 for a one-electron process, Faraday constant F = 96485 C mol^{-1}, electrode area A = 0.07065 cm^2, $Na_4[Fe(CN)_6]$ concentration C_0 = 10 mM, D is the diffusion coefficient, and υ is the kinematic viscosity of 0.5 M Na_2SO_4 and 0.5 M NaPi (1.16222×10^{-6} m^2 s^{-1}) or 1 M NaOH (1.05303×10^{-6} m^2 s^{-1}). The diffusion coefficients (D) of $Na_4[Fe(CN)_6]$ were calculated as 3.53×10^{-6} cm^2 s^{-1} in 0.5 M Na_2SO_4 and 0.5 M NaPi

and 4.70×10^{-6} cm^2 s^{-1} in 1 M NaOH. The electron transfer rate constant k^0 was estimated by the Nicholson method and calculated through the equation as follows,[S2,S3]

$$\Psi = (-0.6288 + 0.0021\times\Delta E\times n)/(1-0.017\times\Delta E\times n) \quad (4)$$

where ΔE (expressed in mV) is the potential difference between anodic and cathodic peaks, n = 1 for a one-electron process and Ψ is a kinetic parameter accounting for the electron transfer rate constant k^0 through the following equation:

$$\Psi = k^0 \times [\pi \times D \times n \times \nu \times F/(R \times T)]^{-0.5} \quad (5)$$

where ν is the scan rate (mV s^{-1}), T is the temperature (298.15 K), and R is the ideal gas constant (8.3145 J K^{-1} mol^{-1}).

Two electrode electrochemical measurements were conducted on a Gamry 1000E potentiostat in a H-cell consisting of two compartments (the volume of each compartment is 250 mL) separated by a cation exchange membrane (Nafion, NR-212, Fuel Cell Store). The working electrodes were Co-P electrode for HER and Ni foam electrode for OER. The counter electrode was a carbon electrode. The electrolyte was 200 mL of 0.5 M Na_2SO_4 and 0.5 M NaPi in each chamber. The buffering capability of the NaPi solution alleviated the formation of pH gradient. For decoupled water electrolysis, 0.3 M $Na_4[Fe(CN)_6]$ was added to the counter chamber. For HER studies, the Co-P electrode was firstly conditioned by CV scans from −0.7 to −4 V at 5 mV s^{-1}. Then the steady-state LSV curve of Co-P electrode was obtained by scanning from negative to positive potential at 5 mV s^{-1}. For OER studies, the Ni foam electrode was firstly conditioned by CV scans from 0 to 4 V at 5 mV s^{-1}. Then the steady-state LSV curve of Ni foam electrode was obtained by scanning from positive to negative potential at 5 mV s^{-1}. All LSV curves measured in the two-electrode configuration had no iR correction. The resistances of our two-electrode systems were measured by EIS in the frequency range of 10^6 – 0.1 Hz with a magnitude of 10 mV.

The cycling of such decoupled water electrolysis in neutral solution was tested in a small H-cell. The counter electrode was a carbon electrode immersed in 15 mL of 0.5 M NaPi and 0.5 M Na_2SO_4 (pH = 7.0) containing 10 mM $Na_4[Fe(CN)_6]$. The working electrode was either Co-P for HER or Ni foam for OER, immersed in 0.5 M NaPi and 0.5 M Na_2SO_4. The buffering capability of the NaPi solution alleviated the formation of pH gradient. Prior to HER or OER for each time, the chambers were purged with N_2. The resistances of such two-electrode systems were also measured by EIS in the frequency range of 10^6 – 0.1 Hz with a magnitude of 10 mV.

Solar-driven decoupled water electrolysis was conducted by in series connection of electrodes, the Gamry 1000E potentiostat and a photovoltaic (PV) cell. The PV cell used in the experiments was a solar cell panel (1.1 V or 1.6 V, Solar Made). The I-V curves of PV cells were collected using both forward and backward voltage sweeps at 5 mV s^{-1} under the sunlight irradiation (92 $\pm$ 5 mW cm^{-2}), leading to same results and thus only the forward voltage sweep results were shown. Typically, for decoupled HER studies, the Co-P electrode was connected with the working lead of the potentiostat while the counter lead was connected to the negative side of PV and the positive side of PV was connected to the carbon electrode. For decoupled OER studies, the Ni foam electrode was connected with the working lead of the potentiostat while the counter lead was connected to the positive side of PV and the negative side of PV was connected to the carbon electrode. The steady-state LSV curves of Co-P for HER and Ni electrodes for OER were collected in the same way as preceding decoupled electrocatalytic water electrolysis. The electrolyte was 200 mL of 0.5 M Na_2SO_4 and 0.5 M NaPi in each chamber, with 0.3 M $Na_4[Fe(CN)_6]$ or $Na_3[Fe(CN)_6]$ only in the counter chamber.

Electrocatalytic water splitting and HMF oxidization under alkaline condition were conducted in a small two-compartment H-cell. The working electrodes were Co-P electrode for HER and Ni foam electrode for either OER or HMF oxidation. The counter electrode was a carbon electrode immersed in 15 mL of 1 M NaOH and 0.3 M $Na_4[Fe(CN)_6]$. The working compartment contained 15 mL of 1 M NaOH. When OER was replaced by HMF oxidation, The Ni foam could also be used for catalyzing HMF oxidation, and 10 mM HMF

was added to the working compartment. The LSV curves were collected at 5 mV s^{-1}. Chronocoulometry was performed at 0.2 V applied to the Ni foam working electrode for HMF oxidation.

For electrochemical studies of (ferrocenylmethyl)trimethylammonium based electron reservoir, Na_2SO_4 aqueous solution (0.5 M) was used as the electrolyte for most of the electrochemical measurements. Cyclic voltammetry experiment in a three-electrode configuration for FcNCl or $FcN(NO_3)$ was conducted with a glassy carbon working electrode (3 mm diameter), a Ag/AgCl (sat. KCl) reference electrode and a carbon rod counter electrode. N_2 was bubbled through the electrolyte solution for at least 20 min prior to measurements and maintained above the electrolyte during the entire process. The CV curves of FcNCl and $FcN(NO_3)$ were not iR-corrected. The steady-state CV curves of Ni_2P/Ni/NF for HER and Ni foam for OER were obtained at a scan rate of mV s^{-1} with iR correction according to **Equation 2**.

The diffusion and electron transfer properties of FcNCl were studied by using CV in a three-electrode configuration. A polished glassy carbon electrode (GCE, area = 0.07065 cm^2) was used as the working electrode. A carbon rod and a calibrated Ag/AgCl (sat. KCl) electrode were used as the counter and reference electrodes, respectively. The electrolyte consisted of 0.01 M FcNCl in 0.5 M Na_2SO_4 deaerated by N_2 bubbling. The CV curves of FcNCl over GCE were collected within 0 – 0.8 V *vs.* Ag/AgCl (sat. KCl) at varying scan rates from 5 to 800 mV s^{-1} without stirring but under N_2 protection. LSV measurements on the rotating disk electrode (RDE) were performed by using a RRDE-3A apparatus (ALS Co., Ltd) in a similar three-electrode configuration except for a polished glassy carbon RDE (area = 0.07065 cm^2) used as the working electrode. The electrolyte was composed of 10 mM FcNCl in 0.5 M Na_2SO_4 deaerated by N_2 bubbling. LSV curves were recorded at a scan rate of 5 mV s^{-1} with the rotation rate varying from 400 to 2800 rpm within the potential window of 0 – 0.8 V *vs.* Ag/AgCl (sat. KCl). The limiting currents (*i.e.*, the mass transport-limited current intensity) were collected at 0.8 V *vs.* Ag/AgCl and plotted over the square root of the rotation rate. The diffusion coefficient of $Na_4[Fe(CN)_6]$ was calculated based on **Equation 3**,[S1] where n = 1 for a one-electron process, Faraday's constant F = 96485 C mol^{-1}, electrode area A = 0.07065 cm^2, FcNCl concentration C_0 = 10 mM, while D is the diffusion coefficient, and the kinematic viscosity υ is 0.0107 cm^2 s^{-1} in 0.5 M Na_2SO_4 aqueous solution. The calculated diffusion coefficient (D) of FcNCl is 0.71 × 10^{-6} cm^2 s^{-1}.

The reciprocals of the current intensities at selected potentials were plotted against the reciprocals of the square root of the rotation rate (**Figure S4C**). The data for each potential were fitted with a linear line; the intercept gives the reciprocal of i_K, the current in the absence of mass transport limitations (the extrapolation to infinite rotation rate). A plot of log(i_K) versus overpotential was linearly fitted (**Figure S4D**). The x-intercept gives the logarithm of the exchange current density i_0, which is equal to FAC_0k_0 based on **Equation 6**,[S1] and gives an electron transfer rate constant k^0 as 1.33 × 10^{-6} cm s^{-1} for FcNCl.

$$i_0 = FAC_0K^0 \quad (6)$$

The decoupled water electrolysis and solar-driven decoupled water splitting with FcNCl electron reservoir are similar to those of $Na_4[Fe(CN)_6]$ assisted water electrolysis. In a typical two-electrode experiment for linear sweep voltammetry studies, 0.5 M Na_2SO_4 solution (pH ~ 6.5, 75 mL) was added into the working compartment of a two-compartment H-cell while 15 ml 0.5 M Na_2SO_4 solution and 0.2202 g FcNCl (50 mM) were added in the counter compartment with a carbon counter electrode. In the working compartment, Ni_2P/Ni/NF and Ni foam electrodes were used as the working electrode for H_2 and O_2 evolution, respectively. Two chambers of the H-cell were separated by an anion exchange membrane (SELEMION™, AMV 120 μm). Both chambers were bubbled with N_2, stirred vigorously and kept under a N_2 atmosphere throughout the experiment. Linear sweep voltammetry (LSV) scans of Ni_2P/Ni/NF for HER were collected at a scan rate of 5 mV s^{-1}. In order to obtain the LSV scans of NF for OER, a two-electrode controlled potential electrolysis was conducted at a voltage input of −2.0 V between Ni_2P/Ni/NF and carbon electrodes to oxidize FcNCl into $FcNCl^+$ in the counter compartment. When an amount of −72.4 C charge had passed, FcNCl in the counter chamber was fully oxidized to $FcNCl^+$. Subsequently, NF was connected as the working electrode and LSV curves scanning anodically were collected at a scan rate of 5 mV s^{-1}. The internal resistance of this cell was measured by EIS. The LSV curves of Ni_2P/Ni/NF for HER and NF for OER had iR correction according to **Equation 2**.

For the cycling test plotted in **Figure 3**, the same experimental condition was utilized as described above, except that the original concentration of FcNCl was 10 mM in the counter compartment. The cycling experiment started with HER electrolysis at −1.6 V applied to Ni_2P/Ni/NF until −7.25 C passed, which indicated that 50 % of FcNCl was oxidized to $FcNCl^+$. Then, NF was utilized as the working electrode and OER electrolysis was started at an applied voltage of 1.7 V until 7.25 C passed, which implied that all the oxidized $FcNCl^+$ was reduced back to FcNCl. Prior to HER or OER for each time, the chambers were purged with N_2. Such a process was repeated for 20 successive cycles. No internal resistance was accounted in these measurements.

The solar-driven decoupled water splitting was conducted by connecting the PV cell (Mini-Panel 1.5 V, SolarMade) in series with the two-electrode water splitting system and the Gamry Interface 1000E potentiostat. Typically, for decoupled HER studies, the Ni_2P/Ni/NF electrode was connected with the working lead of the potentiostat, while the counter lead was connected to the negative side of PV and the positive side of PV was connected to the carbon electrode. A two-compartment H-cell was utilized. The working compartment was charged with 0.5 M Na_2SO_4 (100 mL) and Ni_2P/Ni/NF was used as the working electrode for HER. The counter compartment was filled with 100 mL 0.5 M Na_2SO_4 and 10 mM FcNCl together with a carbon electrode. The two compartments were separated by an anion exchange membrane. The steady-state LSV curves of Ni_2P/Ni/NF for HER were collected in the same way as preceding decoupled electrocatalytic water electrolysis. The sunlight irradiation intensity was 92 ± 5 mW cm^{-2} during these experiments. The internal resistance of this cell was measured by EIS. The LSV curves of Ni_2P/Ni/NF for HER were iR-corrected.
All the aforementioned current densities were calculated on the basis of the geometrical area of electrodes.

Characterization.
Scanning electron microscopy and elemental mapping analysis were conducted on a FEI Quanta 650 FEG microscope equipped with an INCA 350 spectrometer (Oxford Instruments) for energy dispersive X-ray (EDX) spectroscopy. X-ray diffraction (XRD) patterns were collected on a Rigaku MiniflexII Desktop X-ray diffractometer. The generated H_2 and O_2 during electrolysis were detected with a SRI gas chromatograph system 8610C equipped with a HayesSep D packed column, a molecular sieve 13 × packed column, and a thermal conductivity detector. The oven temperature was maintained at 80 °C and argon was used as the carrier gas. High-performance liquid chromatography (HPLC, Shimadzu Prominence LC-2030C) was used to quantify the products of HMF oxidation. During the chronocoulometry experiment, 20 µL of the electrolyte was withdrawn from the working compartment and diluted with 480 µL water. The HPLC was equipped with a 4.6 mm × 150 mm Shim-pack GWS 5 µm C 18 column and an ultraviolet-visible detector set at 265 nm. A mixture of eluting solvents (A and B) was used. Solvents A and B were 5 mM ammonium acetate aqueous solution and methanol, respectively. Separation and quantification were conducted using an isocratic elution of 70 % A and 30 % B for 10 min at a flow rate of 0.5 mL min^{-1}. The quantification and identification of the reaction products were determined from the calibration curves by using standard solutions with known concentrations of commercial HMF, HMFCA, DFF, FFCA and FDCA.

Isolation 2,5-furandicarboxylic acid from 1 M NaOH solution.
After electrolysis (HMF oxidation coupled with reduction of $[Fe(CN)_6]^{3-}$), the FDCA product in 1 M NaOH solution can be isolated by acidifying the solution to pH ~ 0 with H_2SO_4 and subsequently filtering the white precipitate from the solution.

Calculation of energy efficiency of the water electrolyzer.

Water electrolysis involves the hydrogen evolution reaction (HER) on cathode and the oxygen evolution reaction (OER) on anode. The overall reaction is

$$H_2O \rightarrow H_2 + \frac{1}{2}O_2 \quad (7)$$

an endothermic reaction defined as follows,

$$\Delta G^0 = \Delta H^0 - T\Delta S^0 \quad (8)$$

where the change of the Gibbs free energy ΔG^0 = 237.1 kJ mol^{-1}, the enthalpy change ΔH^0 = 285.8 kJ mol^{-1} and the thermal energy $T\Delta S^0$ = 48.7 kJ mol^{-1} under standard conditions (298 K, 1 atm pressure). The thermodynamic voltage corresponding to the change of the Gibbs free energy ΔG^0 is 1.23 V under standard conditions T (298 K, 1 atm pressure), calculated by the following equation,

$$\mathrm{E} = \frac{\Delta G^0}{nF} \quad (9)$$

where n = 2, which is the number of transferred electrons and F the Faradaic constant (96495 C mol^{-1}). The thermodynamic voltage is considered as the theoretical voltage enabling the water electrolysis to start. In fact, the energy efficiency is calculated based on the thermoneutral voltage (E_{tn}), defined as

$$E_{tn} = \frac{\Delta H^0}{nF} \quad (10)$$

which is 1.48 V under standard conditions.[S4, S5]

This calculation method is the same as the one for calculating the energy efficiency of silicotungstic acid-mediated decoupled water splitting by only considering the enthalpy change ΔH^0 = 285.8 kJ mol^{-1}.[S6]
If an electrolyzer works at 100 % efficiency (*i.e.*, at 1.48 V under the standard condition), the heat generated from the electrolyzer will be equal to the heat needed for the electrolysis to proceed, and therefore a thermoneutral situation is achieved. In other words, the electrolyzer neither releases nor absorbs heat to or from the environment. If the voltage is below a cell voltage of 1.48 V (but above 1.23 V), the electrolysis cell would act as a refrigerator absorbing heat from the surroundings. If the voltage is above 1.48 V, heat is generated and must be removed, for an isothermal operation of the electrolyzer.[S4]

Since the Faradaic efficiency is almost 100% in water electrolysis for producing H_2 and O_2, the practical energy efficiency should be calculated by dividing the thermoneutral voltage 1.48 V by the practical cell voltage.

Calculation of energy efficiency for decoupled water splitting with FcNCl electron reservoir in near neutral electrolyte.
As shown in **Figure 2A** (**red curve**), the voltage between Ni_2P/Ni/NF and carbon counter electrodes is −1.478 V to drive a current density of −10 mA cm^{-2} for HER in the presence of 50 mM FcNCl. In the following step for OER and reduction of $FcNCl^+$, a small voltage of 0.954 V is required upon NF and carbon counter electrodes (**Figure 2C red curve**). If a Ni_2P/Ni/NF || NF electrode couple was used for one-step water splitting without any electron reservoir, a large voltage input of 2.338 V was required to produce 10 mA cm^{-2} in 0.5 M Na_2SO_4 (**Figure S6**). This demonstrates a high efficiency of 96 % ($\frac{2.338\ V}{1.478\ V+0.954\ V} \times 100\% = 96\%$) for two-step decoupled water splitting relative to one-step direct water splitting. This efficiency is higher than that of the reported phosphomolybdic acid-mediated (79 %) and potassium hydroquinone sulfonate-mediated (80 %) decoupled water electrolyzers and comparable to that (93 %) of silicotungstic acid-based system in acidic solution and $Ni(OH)_2$-mediated decoupled water electrolysis system (92 %) without considering resistive factors. [S6-S9]
The practical energy efficiency of our decoupled water electrolyzer should be calculated by dividing the thermoneutral potential (*i.e.*, 1.48 V) of water electrolysis by the total cell voltage at room temperature, when the Faradaic efficiencies of HER and OER are both 100 %. The calculated energy efficiency is 61 % ($\frac{1.48\ V}{1.478\ V+0.954\ V} \times 100\% = 61\%$) at 10 mA cm^{-2}. This is comparable to that (63 %) of the silicotungstic acid-mediated decoupled water splitting and the efficiency of Pt-based PEM electrolyzer (67 %) in 1 M H_3PO_4 and $Ni(OH)_2$-mediated Ir || Pt electrolyzer (67 %) in 1 M NaOH solution at room temperature (**Table S1**).

Calculation of energy efficiency for decoupled water splitting with $Na_4[Fe(CN)_6]$ electron reservoir in the neutral electrolyte.
As shown in **Figure S18A** (**red curve**), the voltage between Co-P working electrode and carbon counter electrode is −1.23 V to produce a catalytic HER current density of −10 mA cm^{-2} when the counter chamber

contains 0.3 M $Na_4[Fe(CN)_6]$ and 0.5 M Na_2SO_4 and 0.5 M NaPi buffer solution. In the following step for OER and reduction of $Na_4[Fe(CN)_6]$, a small voltage of 1.06 V is required upon Ni foam working electrode and carbon counter electrode (**Figure S18C, red curve**). If a Co-P || Ni electrode couple was used for one-step water splitting without any electron reservoir, a large voltage input of 2.27 V was required to produce 10 mA cm^{-2} under the same condition (**Figures S18A** and **S18C**, **black curves**). This renders a high efficiency of 99% ($\frac{2.27\ V}{1.23\ V+1.06\ V} \times 100 = 99\%$) for our two-step decoupled water splitting strategy utilizing $Na_4[Fe(CN)_6]$ as an electron reservoir relative to direct water electrolysis. This efficiency is higher than that of the reported phosphomolybdic acid-mediated (79 %) and potassium hydroquinone sulfonate-mediated (80 %) decoupled water electrolyzers, the silicotungstic acid-based system in acidic solution (93 %) and the $Ni(OH)_2$-mediated decoupled water electrolysis system (92 %).[S6-S9]

The practical energy efficiency of such decoupled water electrolyzer should be calculated by dividing the thermoneutral potential (*i.e.*, 1.48 V) of water electrolysis by the total cell voltage at room temperature, when the Faradaic efficiencies of HER and OER are both 100 %. The calculated energy efficiency is 64.6 % ($\frac{1.48\ V}{1.23\ V+1.06\ V} \times 100\% = 64.6\%$) at 10 mA cm^{-2}. This is comparable to that of the silicotungstic acid-mediated (63 %), the potassium hydroquinone sulfonate-mediated (61 %) or the phosphomolybdic acid-mediated (59 %) decoupled water electrolyzers and the Pt-based PEM electrolyzer (67 %) in acidic electrolyte and the efficiency of $Ni(OH)_2$-mediated Ir || Pt electrolyzer (67 %) in 1 M NaOH solution at room temperature (**Table S1**).

The state-of-the-art proton exchange membrane (PEM) electrolyzers show an energy efficiency ranging from 48.5 to 82 %, which mostly work in the acidic media with noble metal based electrocatalysts (Pt, IrO_2 and RuO_2) at elevated temperatures (50–80°C).[S10, S11] The state-of-the-art alkaline electrolyzers show an energy efficiency ranging from 47.2 to 82 %, which work in the alkaline electrolyte with transition metal based electrocatalysts at elevated temperatures (60–80°C). [S10, S11]

Compared to that of the PEM and alkaline electrolyzers, the energy efficiency of our new design of electrolyzer for decoupled water splitting with electron reservoir indeed remains mediocre in the aforementioned range. However, our electrolyzer can function in the environmentally benign neutral electrolyte with transition metal based electrocatalysts and carbon electrodes for decoupled water splitting at room temperature, avoiding the H_2/O_2 crossover issue. The energy efficiency of our new design of electrolyzer for decoupled water splitting with electron reservoir is comparable to that of various reported decoupled water splitting systems (**Table S1**).

Calculation of the experimental solar-to-chemical conversion efficiency.
In the designed PV-electrolyzer system for decoupled water splitting with $Na_4[Fe(CN)_6]$ electron reservoir, the solar-to-hydrogen (STH) conversion efficiency is calculated according to the following equations.[S12, S13]

$$\text{STH efficiency}_{\mathbf{PV\ 1.6V}} = \frac{\Delta E \times I_{WE} \times \eta_F}{P_{in}} = \frac{[0.90\ V - (0\ V)] \times 21\ mA\ cm^{-2} \times 2\ cm^2 \times 100\%}{92\ mW\ cm^{-2} \times 24.99\ cm^2} = 1.64\% \quad (11)$$

Here, ΔE is the potential difference between HER (0 V *vs.* RHE) and oxidation of $Na_4[Fe(CN)_6]$ (0.90 V *vs.* RHE) in 0.5 M Na_2SO_4 and 0.5 M NaPi buffer solution (**Figure S13**). I_{WE} is the operating electrolysis current, which is the average current density (21 mA cm^{-2}, see **Figure S23C**, blue curve) multiplied by the area of Co-P working electrode (2 cm^2). η_F is the Faradaic efficiency (100 %). Power input (P_{in}) is the sunlight intensity (92 mW cm^{-2}) multiplied by the active PV cell area (1.6 V cell, 24.99 cm^2).

$$\text{STH efficiency}_{\mathbf{PV\ 1.1V}} = \frac{\Delta E \times I_{WE} \times \eta_F}{P_{in}} = \frac{[0.90\ V - (0\ V)] \times 5.3\ mA\ cm^{-2} \times 2\ cm^2 \times 100\%}{92\ mW\ cm^{-2} \times 27.34\ cm^2} = 0.38\% \quad (12)$$

Here, ΔE is the potential difference between HER (0 V *vs.* RHE) and oxidation of $Na_4[Fe(CN)_6]$ (0.90 V *vs.* RHE) in 0.5 M Na_2SO_4 and 0.5 M NaPi buffer solution (**Figure S13**). I_{WE} is the operating electrolysis current, which is the average current density (5.3 mA cm^{-2}, see **Figure S23C**, red curve) multiplied by the

area of Co-P working electrode (2 cm^2). η_F is the Faradaic efficiency (100 %). Power input (P_{in}) is the sunlight intensity (92 mW cm^{-2}) multiplied by the active PV cell area (1.1 V cell, 27.34 cm^2).
In the designed PV-electrolyzer system for decoupled water splitting with $Na_4[Fe(CN)_6]$ electron reservoir, the solar-to-oxygen (STO) conversion efficiency is calculated according to the following equations.[S12, S13]

$$\text{STO efficiency}_{\mathbf{PV\ 1.6V}} = \frac{\Delta E \times I_{WE} \times \eta_F}{P_{in}} = \frac{[1.23\ V - (0.9\ V)] \times 27.5\ mA\ cm^{-2} \times 2\ cm^2 \times 100\%}{92\ mW\ cm^{-2} \times 24.99\ cm^2} = 0.79\% \quad (13)$$

Here, ΔE is the potential difference between OER (1.23 V *vs.* RHE) and reduction of $Na_3[Fe(CN)_6]$ (0.90 V *vs.* RHE) in 0.5 M Na_2SO_4 and 0.5 M NaPi buffer solution (**Figure S13**). I_{WE} is the operating electrolysis current, which is the average current density (27.5 mA cm^{-2}, see **Figure S23F**, blue curve) multiplied by the area of Ni foam working electrode (2 cm^2). η_F is the Faradaic efficiency (100 %). Power input (P_{in}) is the sunlight intensity (92 mW cm^{-2}) multiplied by the active PV cell area (1.6 V cell, 24.99 cm^2).

$$\text{STO efficiency}_{\mathbf{PV\ 1.1V}} = \frac{\Delta E \times I_{WE} \times \eta_F}{P_{in}} = \frac{[1.23\ V - (0.9\ V)] \times 16.7\ mA\ cm^{-2} \times 2\ cm^2 \times 100\%}{92\ mW\ cm^{-2} \times 27.34\ cm^2} = 0.44\% \quad (14)$$

Here, ΔE is the potential difference between OER (0 V *vs.* RHE) and reduction of $Na_3[Fe(CN)_6]$ (0.90 V *vs.* RHE) in 0.5 M Na_2SO_4 and 0.5 M NaPi buffer solution (**Figure S13**). I_{WE} is the operating electrolysis current, which is the average current density (16.7 mA cm^{-2}, see **Figure S23F**, red curve) multiplied by the area of Ni foam working electrode (2 cm^2). η_F is the Faradaic efficiency (100 %). Power input (P_{in}) is the sunlight intensity (92 mW cm^{-2}) multiplied by the active PV cell area (1.1 V cell, 27.34 cm^2).

The effects of electrode size, PV panel size and PV power density on the solar-to-hydrogen (STH) conversion efficiency.
The solar-to-hydrogen (STH) conversion efficiency is calculated according to the following equation. [S12, S13]

$$\text{STH efficiency} = \frac{\Delta E \times J_{WE} \times A_{WE} \times \eta_F}{\text{Intensity} \times A_{PV}} \quad (15)$$

Here, ΔE is the potential difference between HER and oxidation of electron reservoir or water in the electrolyte at a given pH. J_{WE} is the electrolysis current density normalized by the working electrode area. A_{WE} is the area of the working electrode. η_F is the Faradaic efficiency. Intensity is the sunlight intensity and A_{PV} is the active area of the PV panel.

Since the Faradaic efficiency is nearly 100 % in most cases and Intensity is determined by the natural sunlight irradiation, the STH efficiency is mainly dependent on the potential difference (ΔE), the ratio of the electrode area versus the PV panel area and the current density (J_{WE}). Therefore, the match between the electrolyzer and PV plays a critical role in determining the STH efficiency.
In order to driven the water splitting at an appreciable current, the open circuit voltage (V_{OC}) of the PV cell should be higher than the theoretical potential difference (ΔE) and the practical operating voltage. The short circuit current (I_{SC}) of the PV cell should be higher than the practical electrolysis operating current. The efficient electrocatalysts can promote the electrolysis current density (J_{WE}). Increasing the ratio of the electrode area versus the PV panel area will enhance the STH efficiency.

For example, a PV cell (*e.g.*, V_{OC} = 1.1 V, I_{SC} = 500 mA, A_{PV} = 27.34 cm^2) and the neutral electrolyte (0.5 M Na_2SO_4 and 0.5 M NaPi buffer solution) were used in this work. Without the assistance of electron reservoir, the thermodynamic voltage for water splitting (ΔE) is 1.23 V and the practical operating voltage is always higher than 2.0 V. Such a PV cell cannot drive the direct water splitting. Therefore, it is necessary to connect several PV panels in series to drive the overall water splitting.

In contrast, ΔE is decreased to 0.9 V with the assistance of $Na_4[Fe(CN)_6]$ electron reservoir and such PV cell can apparently drive the HER coupled with the oxidation of $Na_4[Fe(CN)_6]$, resulting in a calculated STH efficiency of 0.38 % when the area of the working Co-P electrode is 2 cm^2. If the area of the working electrode is enlarged to 100 cm^2, the STH efficiency is estimated to be 18 % (assuming the HER current density is still *ca.* 5 mA cm^{-2}), which is comparable to the efficiency of many reports.[S14, S15] Therefore, our

decoupled water electrolysis system demonstrates the advantages in lowering the voltage input, expanding the candidate pool of semiconductors absorbing longer-wavelength sunlight for solar-driven water electrolysis without the need of many solar cells in series connection. [S12, S14]

If a large-area working electrode is used (*e.g.*, 100 cm^2, current density = 5 mA cm^{-2}) with the PV cell of 1.1 V and a diurnal cycle is 10 h, at least 622 mL of 0.3 M $Na_4[Fe(CN)_6]$ electron reservoir is required to maintain the electrolysis. The electron reservoir with higher solubility is preferred in order to minimize the space. Therefore, the (ferrocenylmethyl)trimethylammonium chloride (FcNCl) electron reservoir is also introduced with the solubility of 4 M in water and proper redox potential (**Figure 1**) for decoupled water splitting under near neutral conditions. For instance, if 4 M FcNCl is used to replace 0.3 M $Na_4[Fe(CN)_6]$ electron reservoir, the volume of electrolyte in the counter chamber can be reduced to 47 mL.

The optimal match between the decoupled water electrolysis system and the PV cell is critical for achieving a high STH efficiency and meeting the practical requirements of diurnal cycles, in terms of the power density and size of PV cell and electrolyzer as well as other operation parameters such as temperature, concentration and volume of electron reservoir and sunlight irradiation intensity. Optimizing the PV-decoupled water electrolysis system design will be crucial for enabling the deployment of economical large-scale installations.[S12]

II. Supplemental Figures

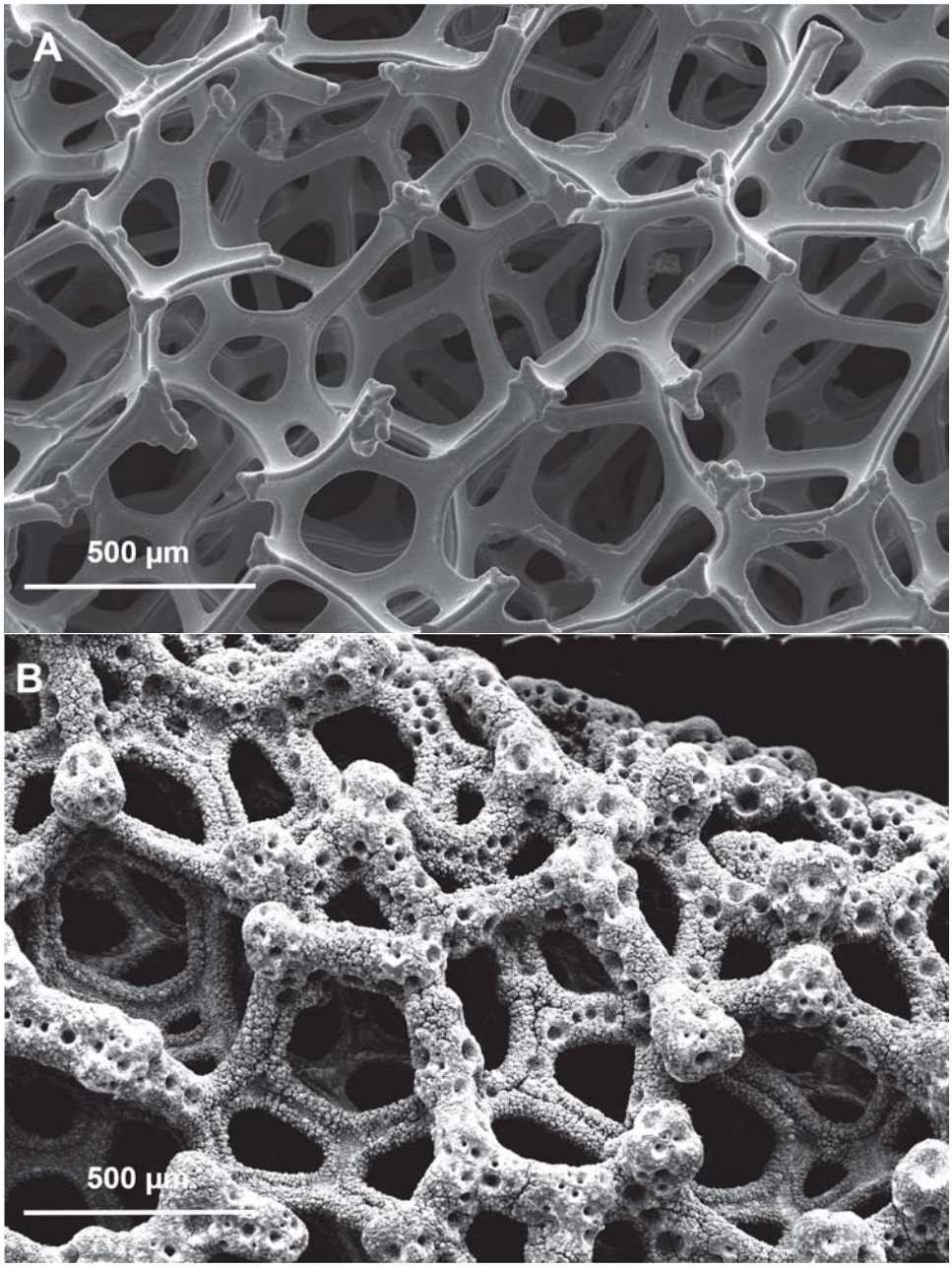

Figure S1. SEM images of (A) the pristine Ni foam (NF) and (B) the prepared Ni_2P/Ni/NF electrocatalyst.

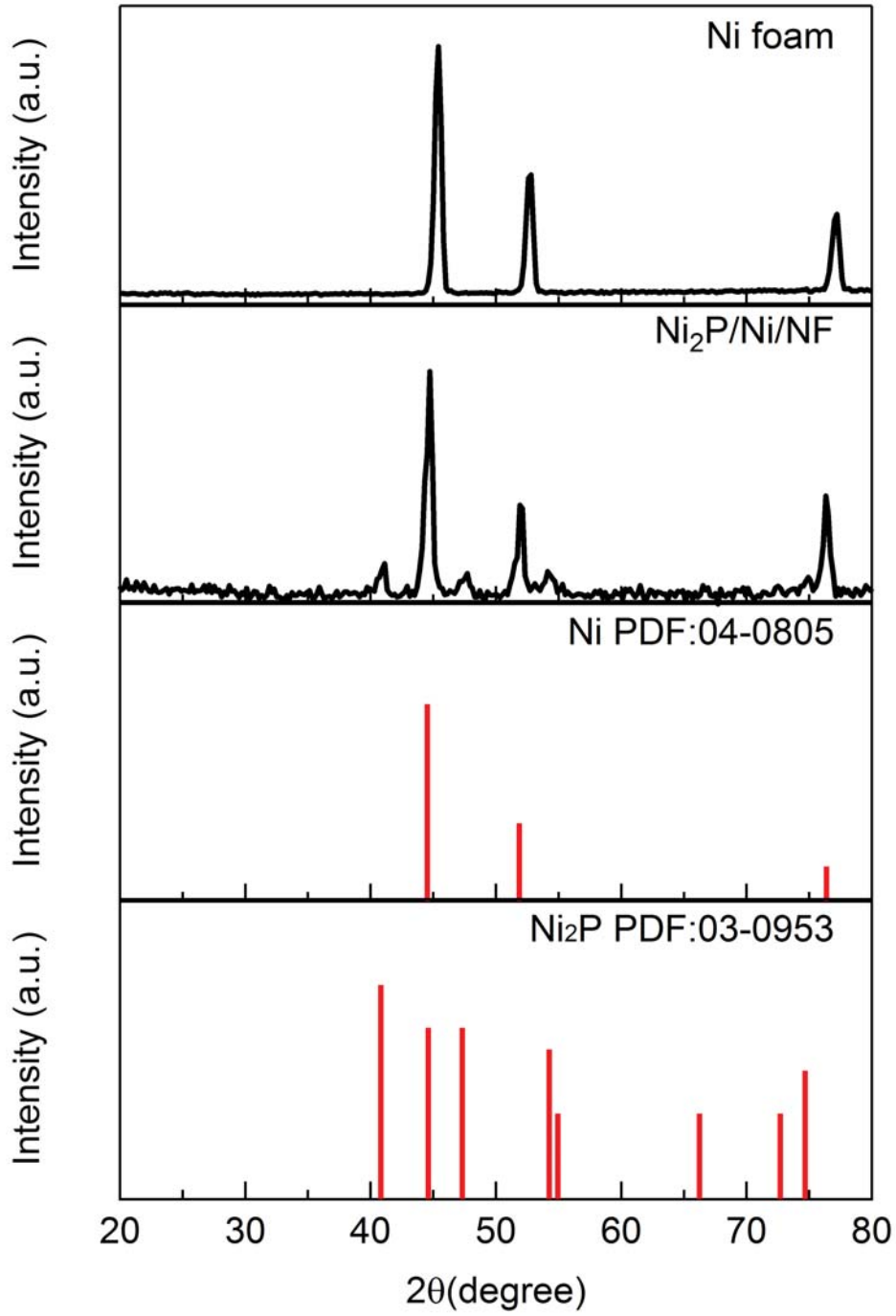

Figure S2. XRD patterns of Ni foam and Ni_2P/Ni/NF as well as the standard XRD patterns of metallic nickel and Ni_2P.

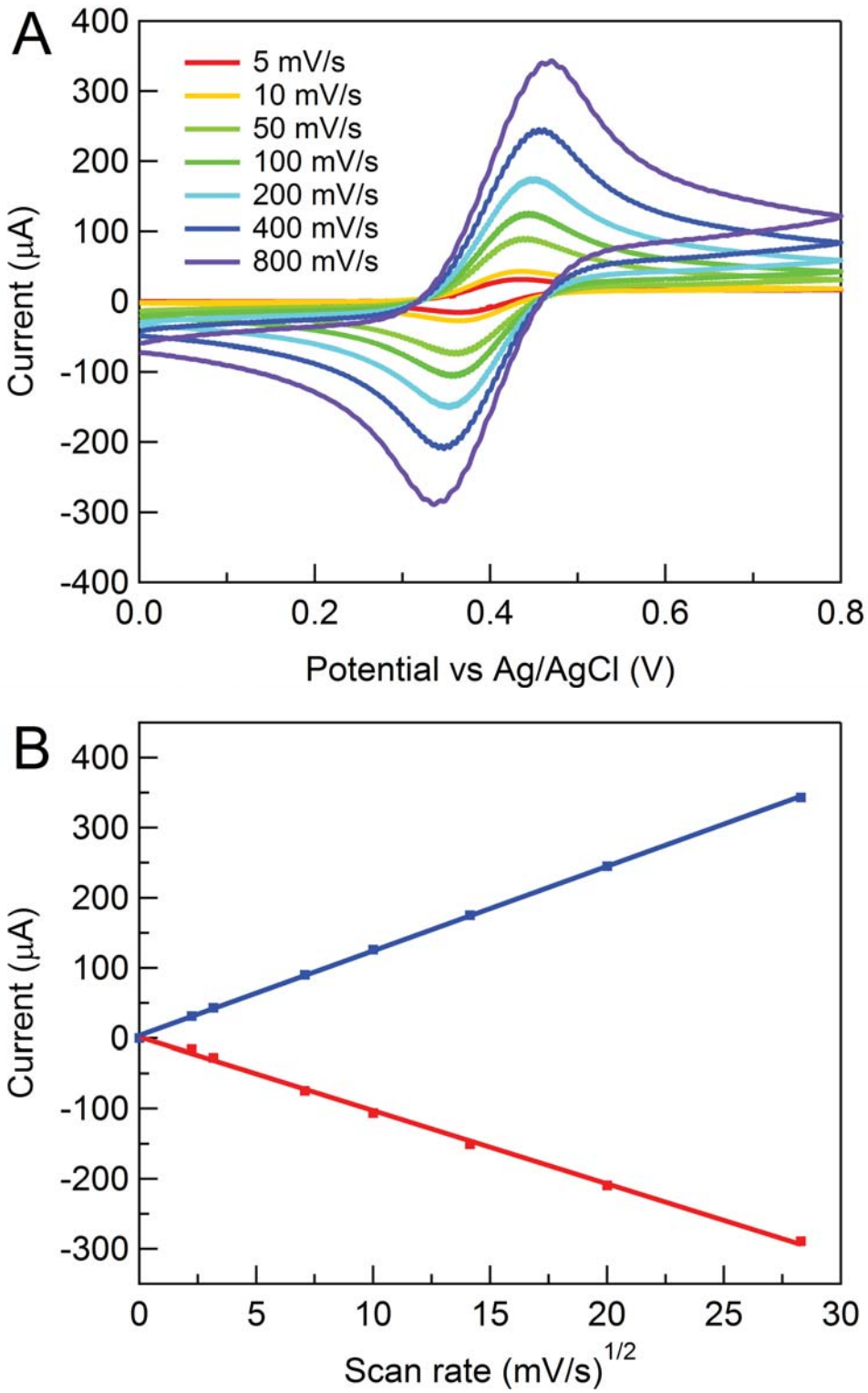

Figure S3. (A) Cyclic voltammograms of 10 mM FcNCl in 0.5 M Na_2SO_4 at different scant rates. (B) Plots of anodic (blue line) and cathodic (red line) peak currents *vs.* square root of scan rate for 10 mM FcNCl in 0.5 M Na_2SO_4. A three-electrode configuration was utilized with a glassy carbon working electrode (d = 3 mm), a carbon rod counter electrode and a Ag/AgCl (sat. KCl) reference electrode.

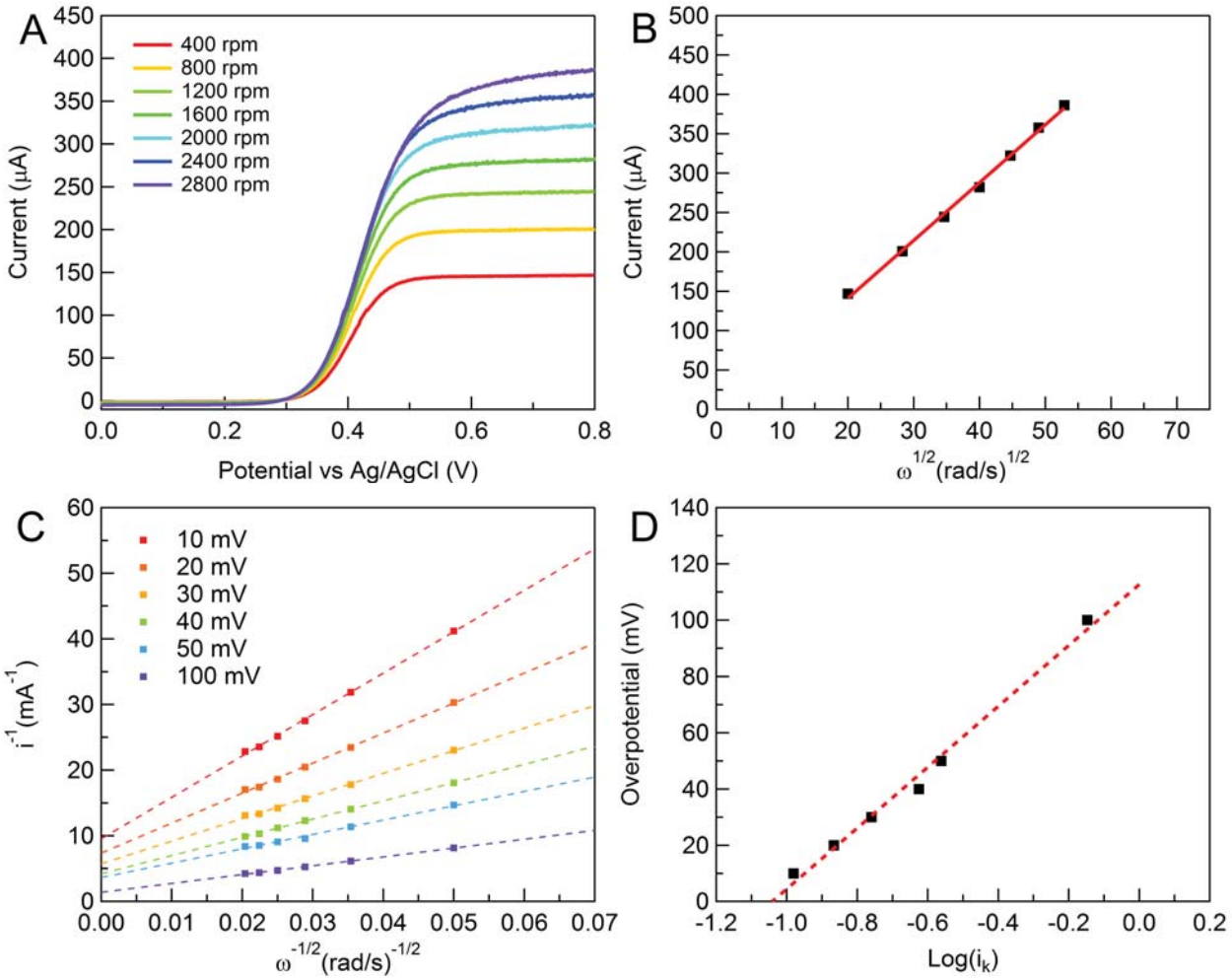

Figure S4. (A) Anodic scans of cyclic voltammetry of 10 mM FcNCl in 0.5 M Na_2SO_4 at different rotating speeds on a rotating disk glassy carbon electrode. (B) Levich plot of the limiting current versus the square root of different rotating speeds. (C) The reciprocals of current intensities at 0.36, 0.37, 0.38, 0.39, 0.40, and 0.45 V (*vs.* Ag/AgCl) versus the reciprocals of the square root of rotation rates. (D) A plot of potential versus log(i_k).

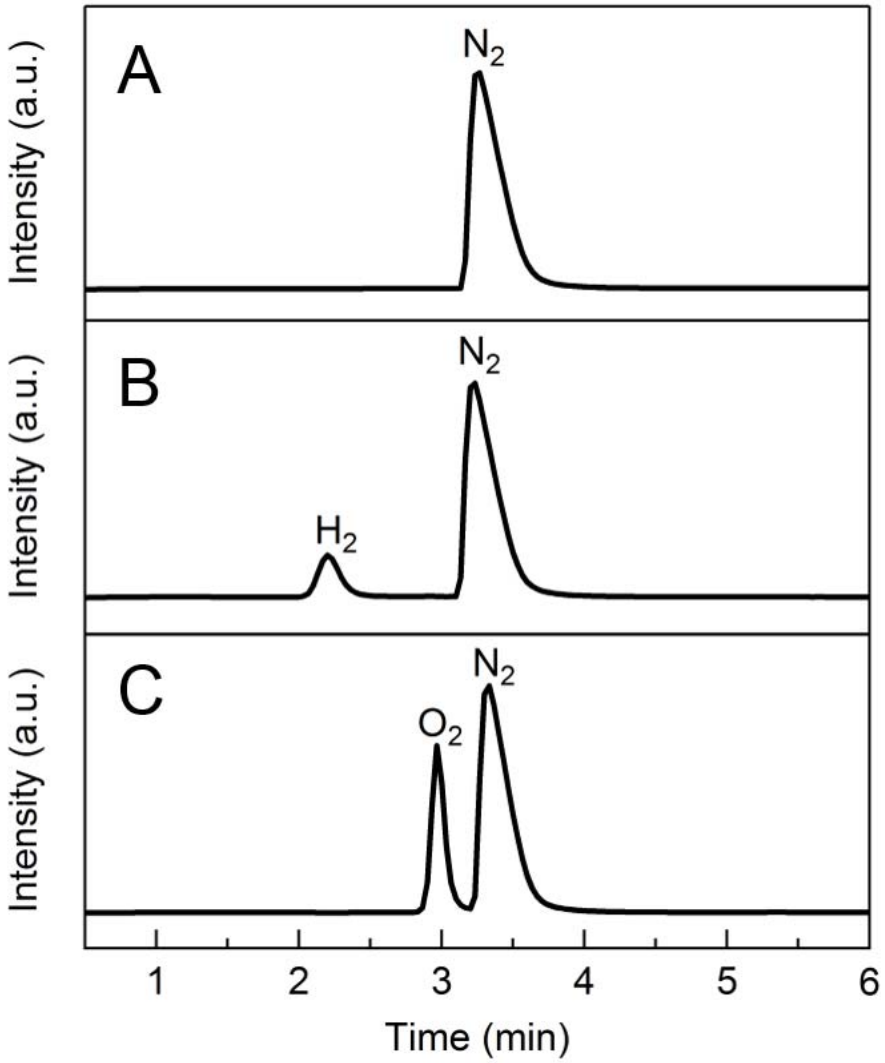

Figure S5. Representative gas chromatograms collected from the headspace of the working compartment of a two-electrode H cell before (A), during H_2 evolution (B), and during O_2 evolution (C) electrolysis. Electrolytes in the working and counter compartments were 0.5 M Na_2SO_4 and 0.5 M Na_2SO_4 + 50 mM FcNCl, respectively.

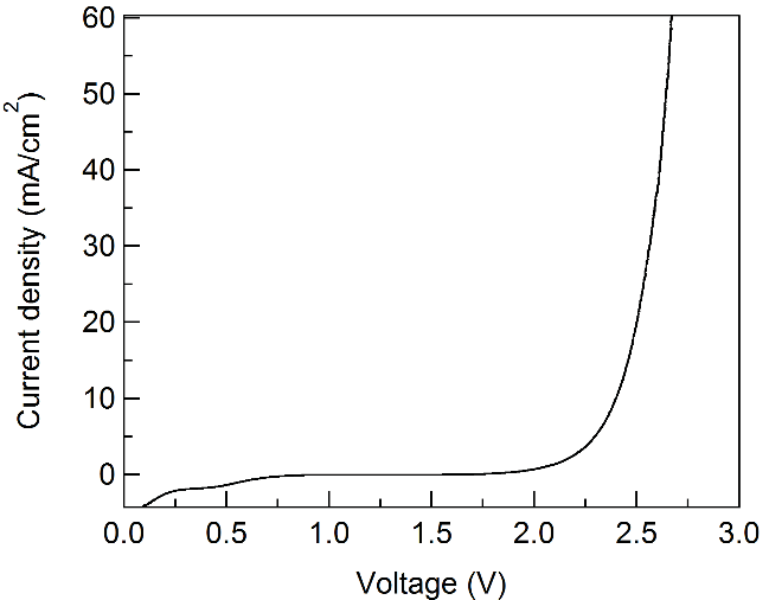

Figure S6. Polarization curve of Ni_2P/Ni/NF || NF two-electrode system for direct overall water splitting in 0.5 M Na_2SO_4 at a scan rate of 5 mV s^{-1} (with iR correction). The Ni foam (NF) was used as the working electrode for OER, while the Ni_2P/Ni/NF was used as the counter electrode for HER.

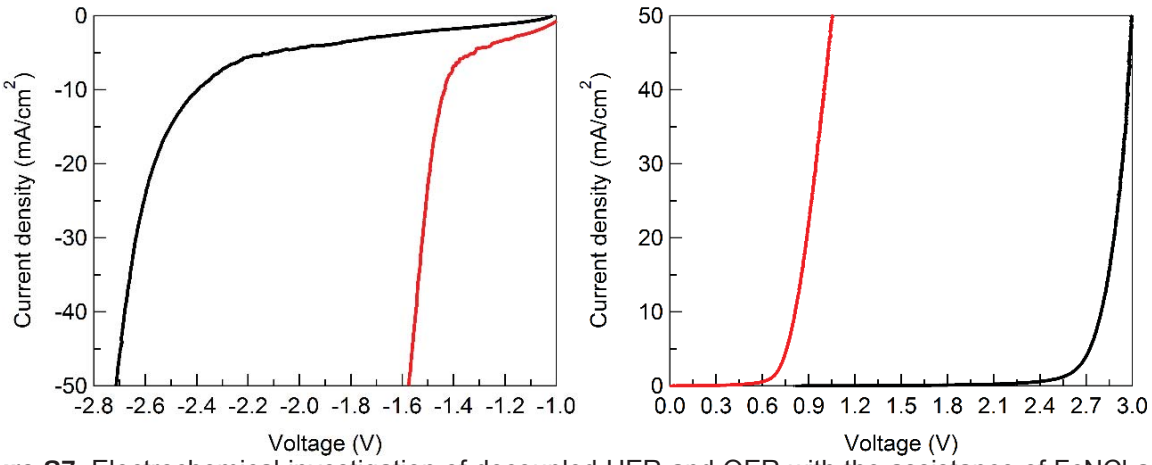

Figure S7. Electrochemical investigation of decoupled HER and OER with the assistance of FcNCl as an electron reservoir in 0.1 M potassium hydrogen phthalate buffer and 0.5 M Na_2SO_4 (pH = 5).
Left: Linear sweep voltammograms of Ni_2P/Ni/NF as the working electrode and carbon rod as the counter electrode with 0 (black) or 50 mM (red) FcNCl, 0.1 M potassium hydrogen phthalate buffer and 0.5 M Na_2SO_4 in the counter chamber, and only 0.1 M potassium hydrogen phthalate buffer and 0.5 M Na_2SO_4 in the working compartment (scan rate = 5 mV s^{-1}, iR-corrected).
Right: Linear sweep voltammograms of NF as the working electrode and carbon rod as the counter electrode with 0 (black) or 50 mM (red) $FcNCl^+$, 0.1 M potassium hydrogen phthalate buffer and 0.5 M Na_2SO_4 in the counter chamber, and only 0.1 M potassium hydrogen phthalate buffer and 0.5 M Na_2SO_4 in the working compartment (scan rate = 5 mV s^{-1}, iR-corrected).

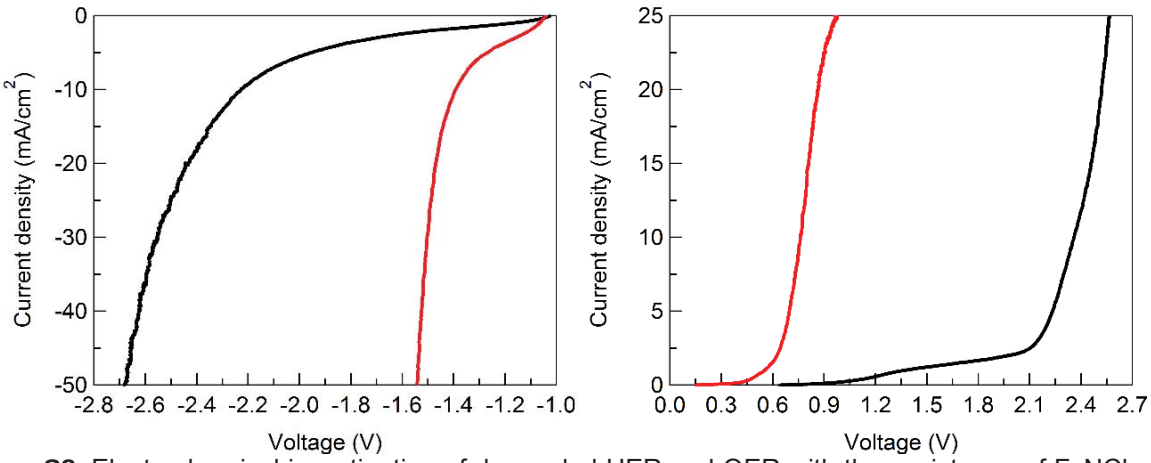

Figure S8. Electrochemical investigation of decoupled HER and OER with the assistance of FcNCl as an electron reservoir in 0.1 M phosphate buffer and 0.5 M Na_2SO_4 (pH = 7).
Left: Linear sweep voltammograms of Ni_2P/Ni/NF as the working electrode and carbon rod as the counter electrode with 0 (black) or 50 mM (red) FcNCl, 0.1 M phosphate buffer, and 0.5 M Na_2SO_4 in the counter chamber and only 0.1 M phosphate buffer and 0.5 M Na_2SO_4 in the working compartment (scan rate = 5 mV s^{-1}, iR-corrected).
Right: Linear sweep voltammograms of NF as the working electrode and carbon rod as the counter electrode with 0 (black) or 50 mM (red) $FcNCl^+$, 0.1 M phosphate buffer and 0.5 M Na_2SO_4 in the counter chamber, and only 0.1 M phosphate buffer and 0.5 M Na_2SO_4 in the working compartment (scan rate = 5 mV s^{-1}, iR-corrected).

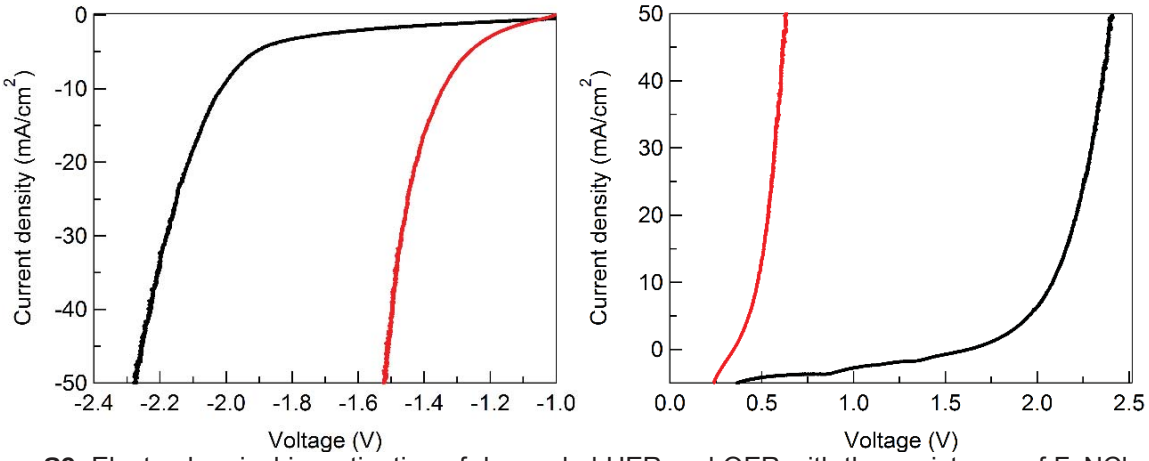

Figure S9. Electrochemical investigation of decoupled HER and OER with the assistance of FcNCl as an electron reservoir in 0.1 M sodium borate buffer and 0.5 M Na_2SO_4 (pH = 9).
Left: Linear sweep voltammograms of Ni_2P/Ni/NF as the working electrode and carbon rod as the counter electrode with 0 (black) or 50 mM (red) FcNCl, 0.1 M sodium borate buffer, and 0.5 M Na_2SO_4 in the counter chamber, and only 0.1 M sodium borate buffer and 0.5 M Na_2SO_4 in the working compartment (scan rate = 5 mV s^{-1}, iR-corrected).
Right: Linear sweep voltammograms of NF as the working electrode and carbon rod as the counter electrode with 0 (black) or 50 mM (red) $FcNCl^+$, 0.1 M sodium borate buffer, and 0.5 M Na_2SO_4 in the counter chamber, and only 0.1 M sodium borate buffer and 0.5 M Na_2SO_4 in the working compartment (scan rate = 5 mV s^{-1}, iR-corrected).

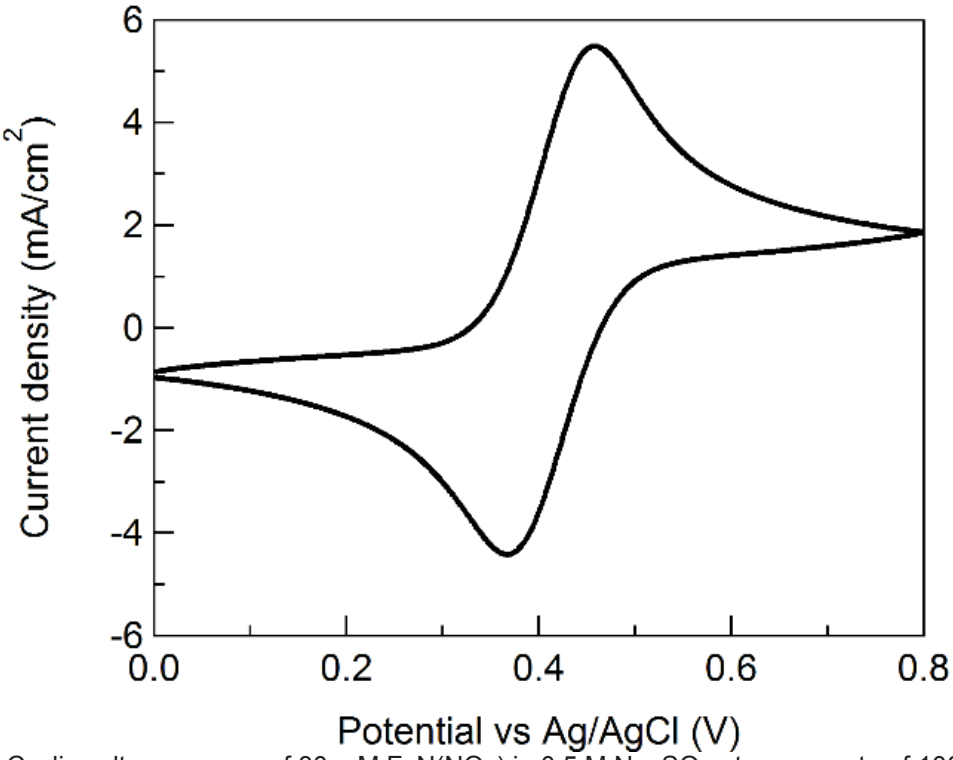

Figure S10. Cyclic voltammogram of 30 mM $FcN(NO_3)$ in 0.5 M Na_2SO_4 at a scan rate of 100 mV s^{-1} with glassy carbon and carbon rod as the working and counter electrodes, respectively. No iR correction was applied.

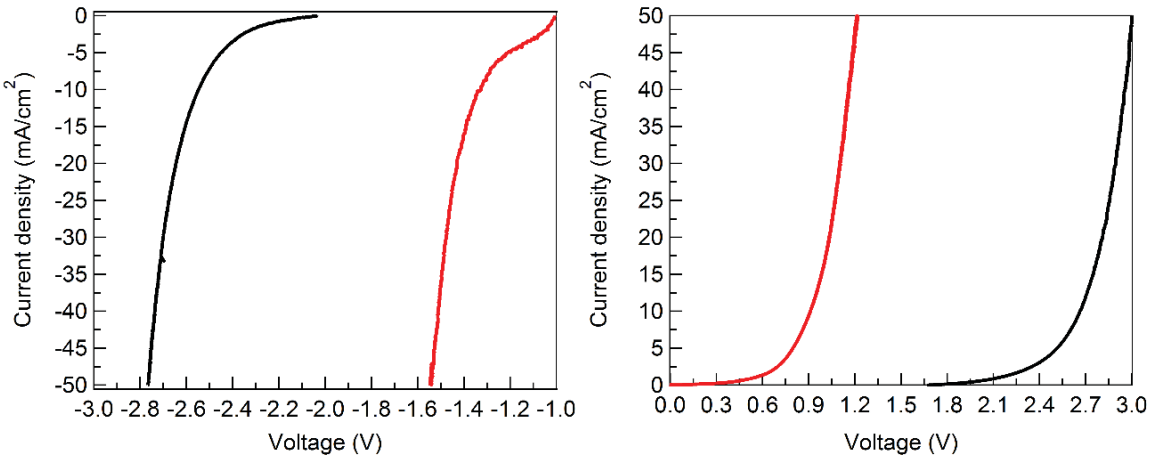

Figure S11. Electrochemical investigation of decoupled HER and OER with the assistance of $FcN(NO_3)$ as an electron reservoir in 0.5 M Na_2SO_4.
Left: Linear sweep voltammograms of Ni_2P/Ni/NF as the working electrode and carbon rod as the counter electrode with 0 (black) or 50 mM (red) $FcN(NO_3)$ and 0.5 M Na_2SO_4 in the counter chamber only 0.5 M Na_2SO_4 in the working compartment (scan rate = 5 mV s^{-1}, iR-corrected).
Right: Linear sweep voltammograms of NF as the working electrode and carbon rod as the counter electrode with 0 (black) or 50 mM (red) $FcN(NO_3)^+$ and 0.5 M Na_2SO_4 in the counter chamber and 0.5 M Na_2SO_4 in the working compartment (scan rate = 5 mV s^{-1}, iR-corrected).

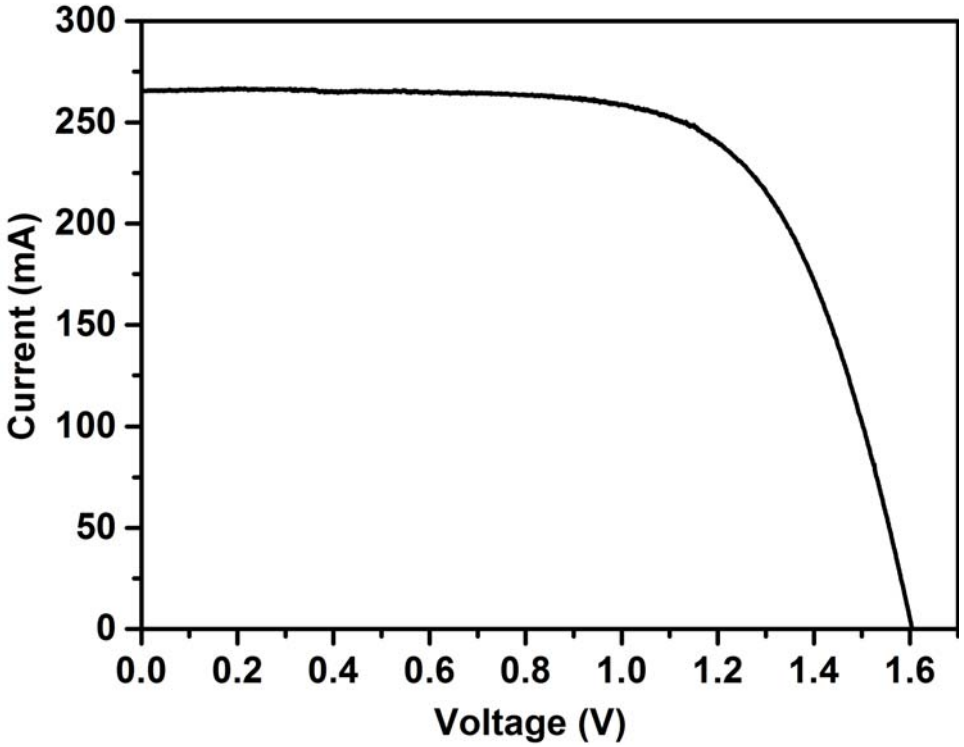

Figure S12. Current-voltage curve of the PV cell used for driving decoupled water splitting in 0.5 M Na_2SO_4 solution with 10 mM FcNCl electron reservoir under the sunlight irradiation (92 $\pm$ 5 mW cm^{-2}).

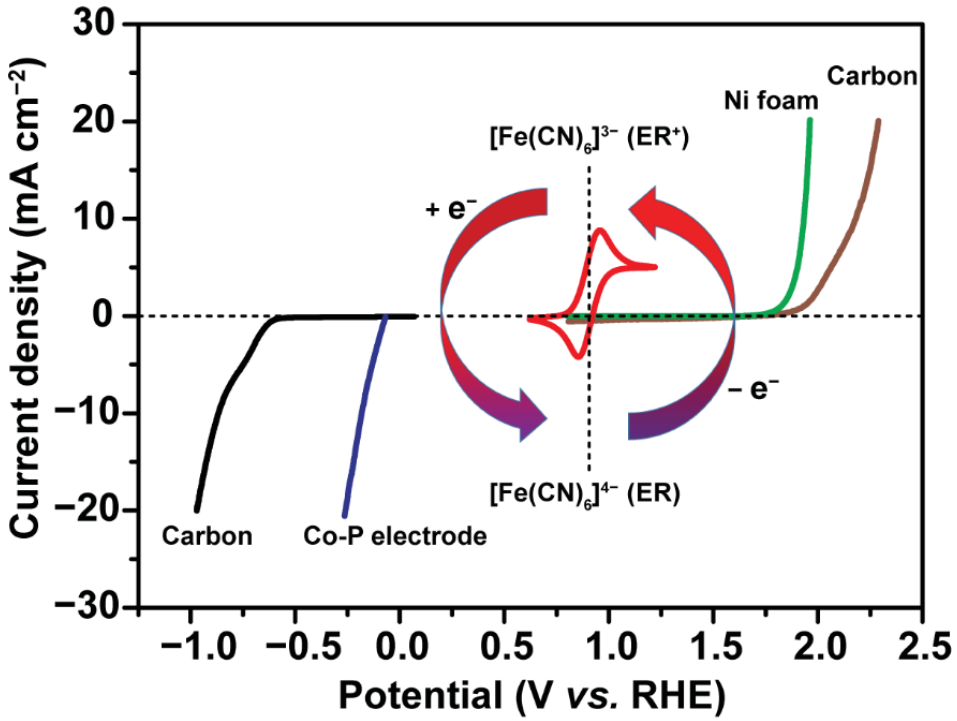

Figure S13. Linear sweep voltammograms of carbon working electrode for HER (black) and OER (brown), Co-P working electrode for HER (blue), and Ni foam working electrode for OER (green) in 0.5 M Na_2SO_4 and 0.5 M NaPi (pH = 7.0) at a scan rate of 5 mV s^{-1}. Cyclic voltammogram (red) of 0.3 M $Na_4[Fe(CN)_6]$ (ER) measured over a glassy carbon working electrode in the same electrolyte at a scan rate of 5 mV s^{-1}. All linear sweep voltammogram curves were iR-corrected. A carbon counter electrode and a Ag/AgCl (3 M NaCl) reference electrode were utilized for all the above measurements in a three-electrode configuration. As displayed in **Figure S13**, the cyclic voltammogram of 0.3 M $Na_4[Fe(CN)_6]$ in 0.5 M Na_2SO_4 and 0.5 M sodium phosphate buffer (NaPi) solution (pH = 7.0) shows a reversible redox feature at 0.90 V *vs.* reversible hydrogen electrode (RHE). In the same electrolyte, carbon electrodes achieve the benchmark current density of 10 mA cm^{-2} for HER at −0.87 V *vs.* RHE and OER at 2.18 V *vs.* RHE. Since in neutral electrolyte, a large group of earth-abundant electrocatalysts can be employed to reduce the voltage inputs for water splitting, herein we used a Co-P electrode for HER and a Ni foam electrode for OER (**Figures S14**–**S16**). Consequently, the current density of 10 mA cm^{-2} could be achieved for HER on Co-P and OER on Ni foam at −0.185 and 1.932 V *vs.* RHE, respectively. Nevertheless, the redox potential of $Na_4[Fe(CN)_6]$ is still well located between the onset potentials of HER and OER.

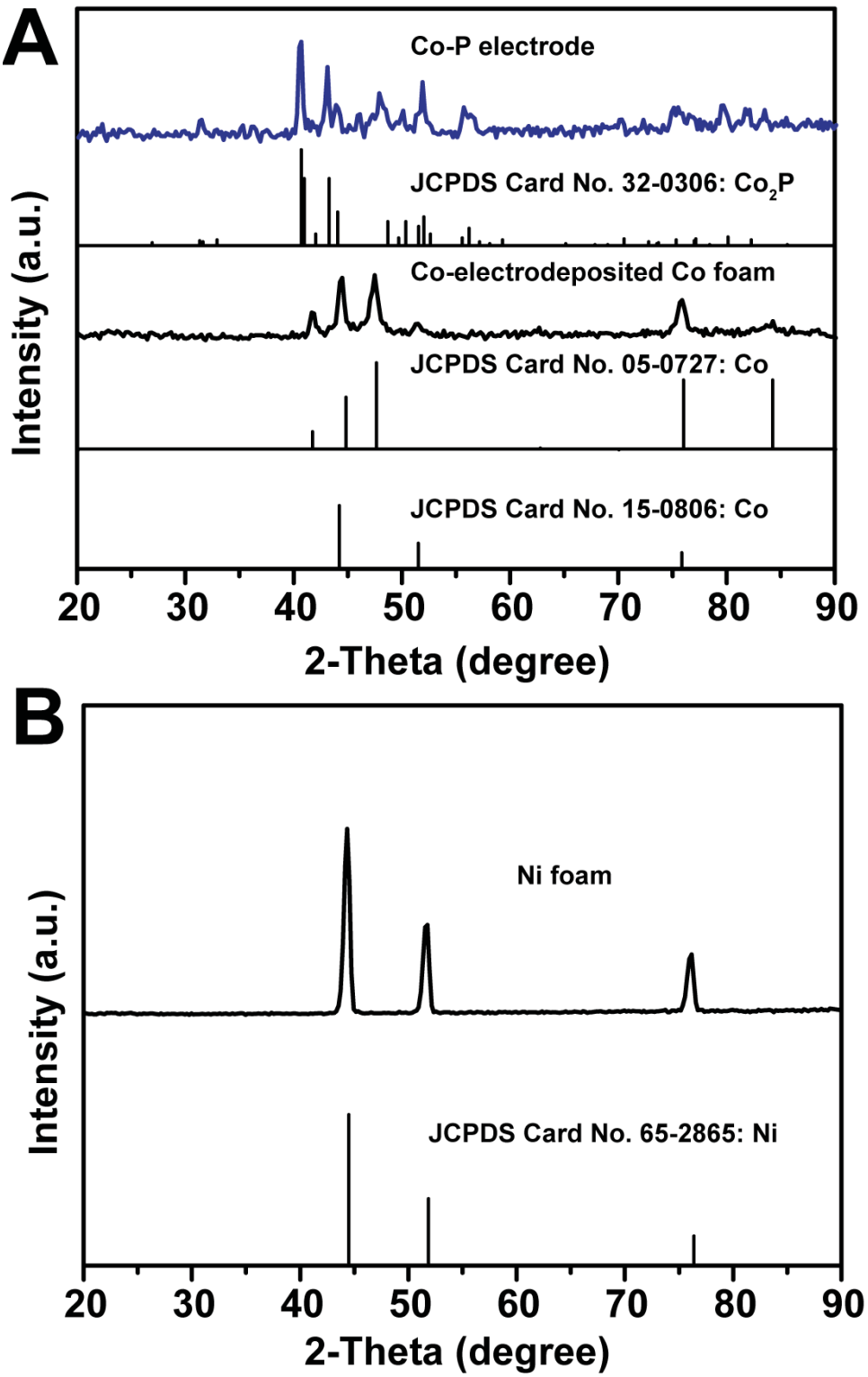

Figure S14. (A) XRD patterns of a Co foam electrodeposited with Co particles and the resultant Co-P electrode after thermal phosphorization. (B) XRD pattern of a cleaned Ni foam. Corresponding standard XRD patterns are included as references.

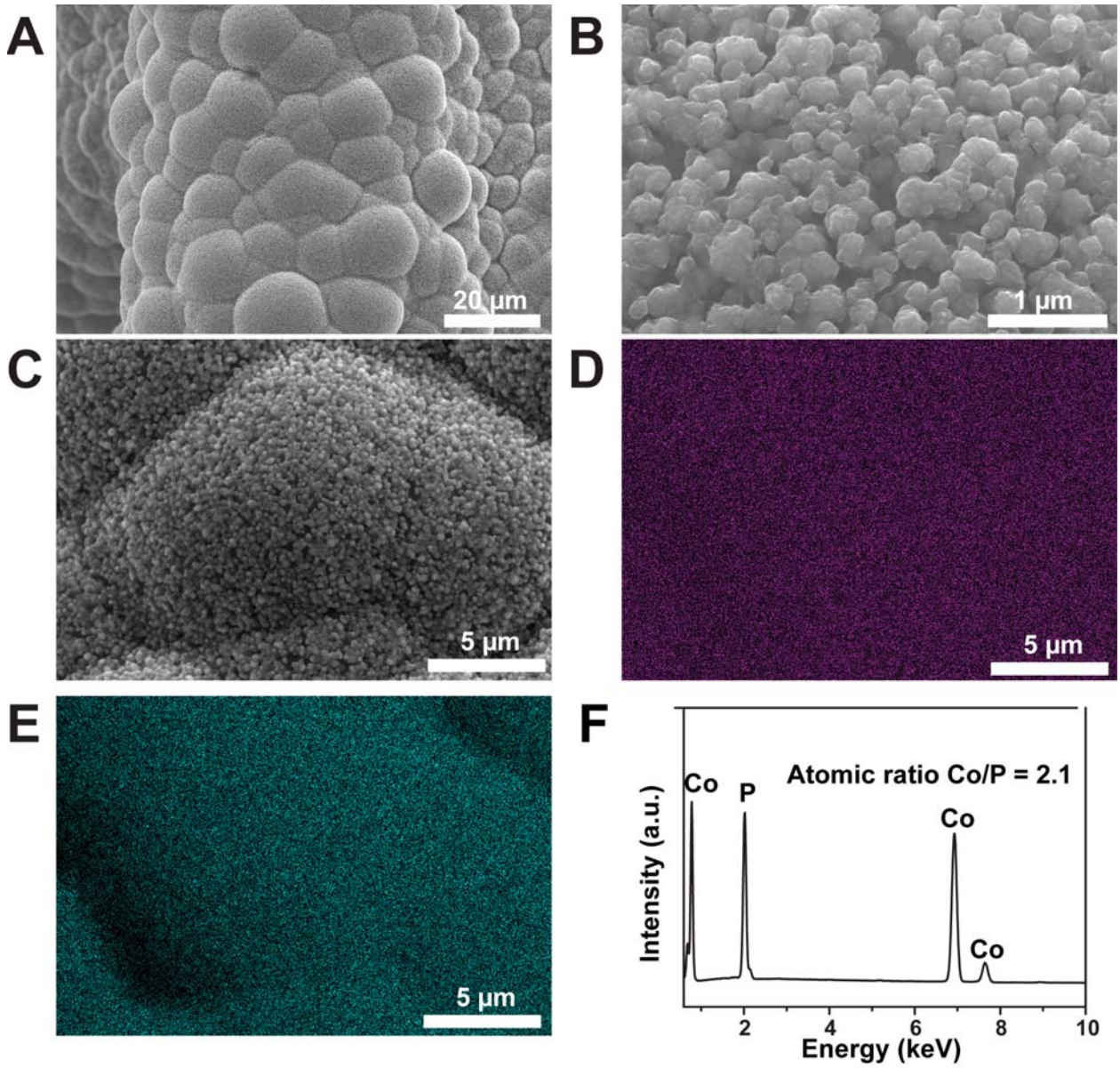

Figure S15. SEM images of Co-P electrode (A-C), elemental mapping images of Co (D) and P (E) and EDX spectrum of Co-P electrode (F).

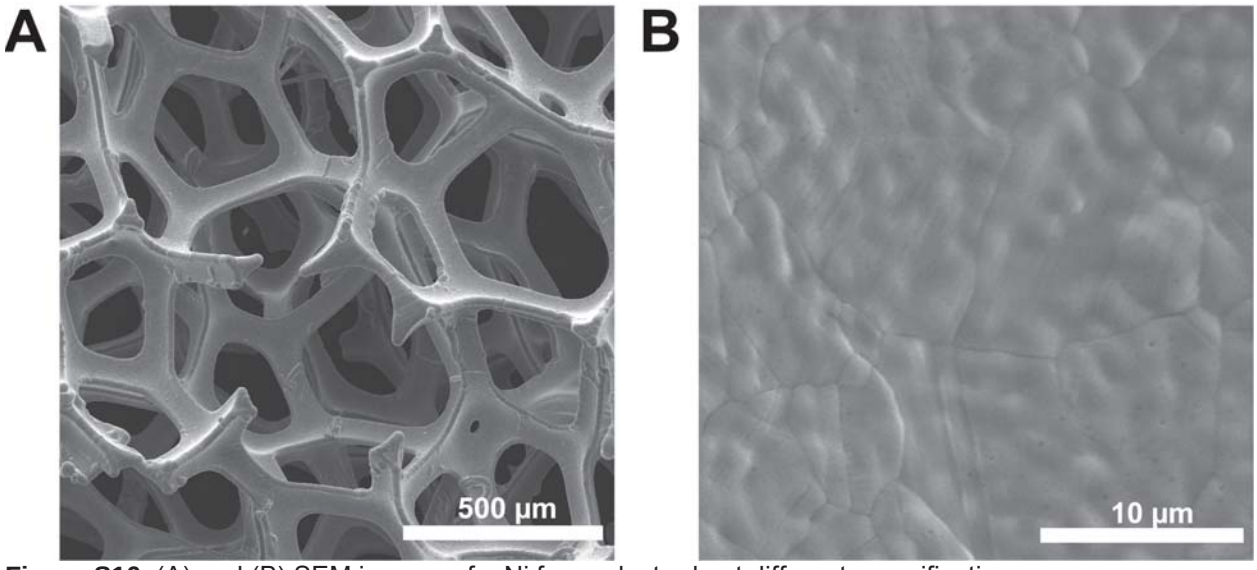

Figure S16. (A) and (B) SEM images of a Ni foam electrode at different magnifications.

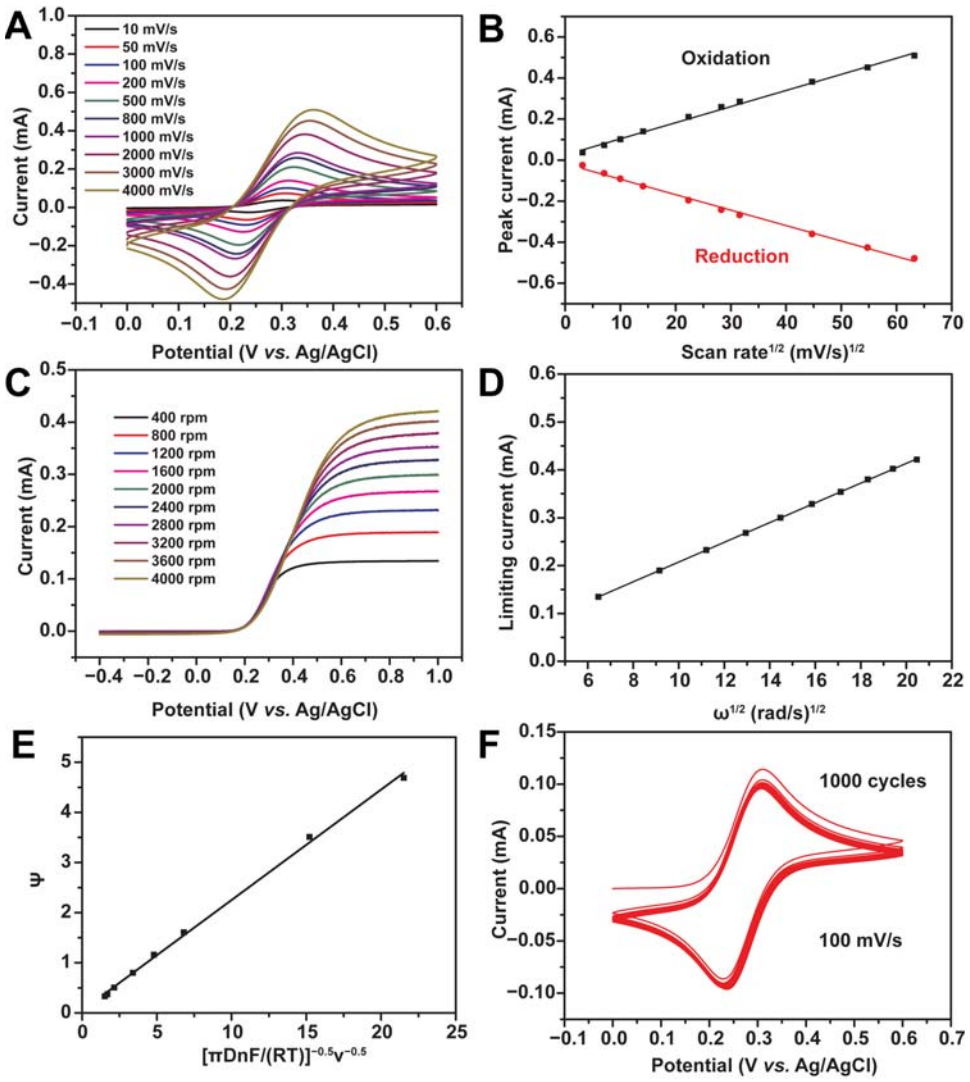

Figure S17. (A) Cyclic voltammetry (CV) curves of 10 mM $Na_4[Fe(CN)_6]$ over a glassy carbon electrode at varying scan rates from 10 to 4000 mV s^{-1}. (B) Plots of oxidation and reduction peak currents *vs.* square root of scan rate for 10 mM of $Na_4[Fe(CN)_6]$. (C) Linear sweep voltammetry (LSV) curves of 10 mM of $Na_4[Fe(CN)_6]$ over a rotating disk glassy carbon electrode scanned at 5 mV s^{-1} at different rotation speeds ranging from 400 to 4000 rpm. (D) Levich plot of the limiting current *vs.* the square root of rotation rates for 10 mM of $Na_4[Fe(CN)_6]$. (E) Plot of Ψ versus $[\pi DnF/(RT)]^{-0.5}v^{-0.5}$ for calculating the electron transfer rate constant of $Na_4[Fe(CN)_6]$. (F) CV curves of 10 mM of $Na_4[Fe(CN)_6]$ over a glassy carbon electrode at 100 mV s^{-1} for 1000 cycles. The electrolyte was 0.5 M Na_2SO_4 and 0.5 M sodium phosphate buffer (NaPi) solution (pH = 7.0). The area of either the glassy carbon electrode or rotating disk glassy carbon electrode was 0.07065 cm^2. All plots were not iR-corrected.

Scan rate dependence of its redox feature demonstrates the linear relationship of its anodic and cathodic current densities with the square root of the scan rate (**Figures S17A**–**S17B**), indicating this redox process involves a molecular species under diffusion control.[S1] The diffusion coefficient of $Na_4[Fe(CN)_6]$ was measured as 3.53×10^{-6} cm^2 s^{-1} from the derived Levich plot (**Figures S17C**–**S17D**), which is comparable with the previous report.[S16] The electron transfer rate constant of $Na_4[Fe(CN)_6]$ was estimated to be 2.20×10^{-1} cm s^{-1} by the Nicolson method (**Figure S17E**).[S2, S3, S17] Such large diffusion coefficient and electron transfer rate indicate fast electron transfer kinetics of $Na_4[Fe(CN)_6]$ as an electron reservoir. The robustness of $Na_4[Fe(CN)_6]$ was also manifested by the negligible degradation during 1000 redox cycles (**Figure S17F**).

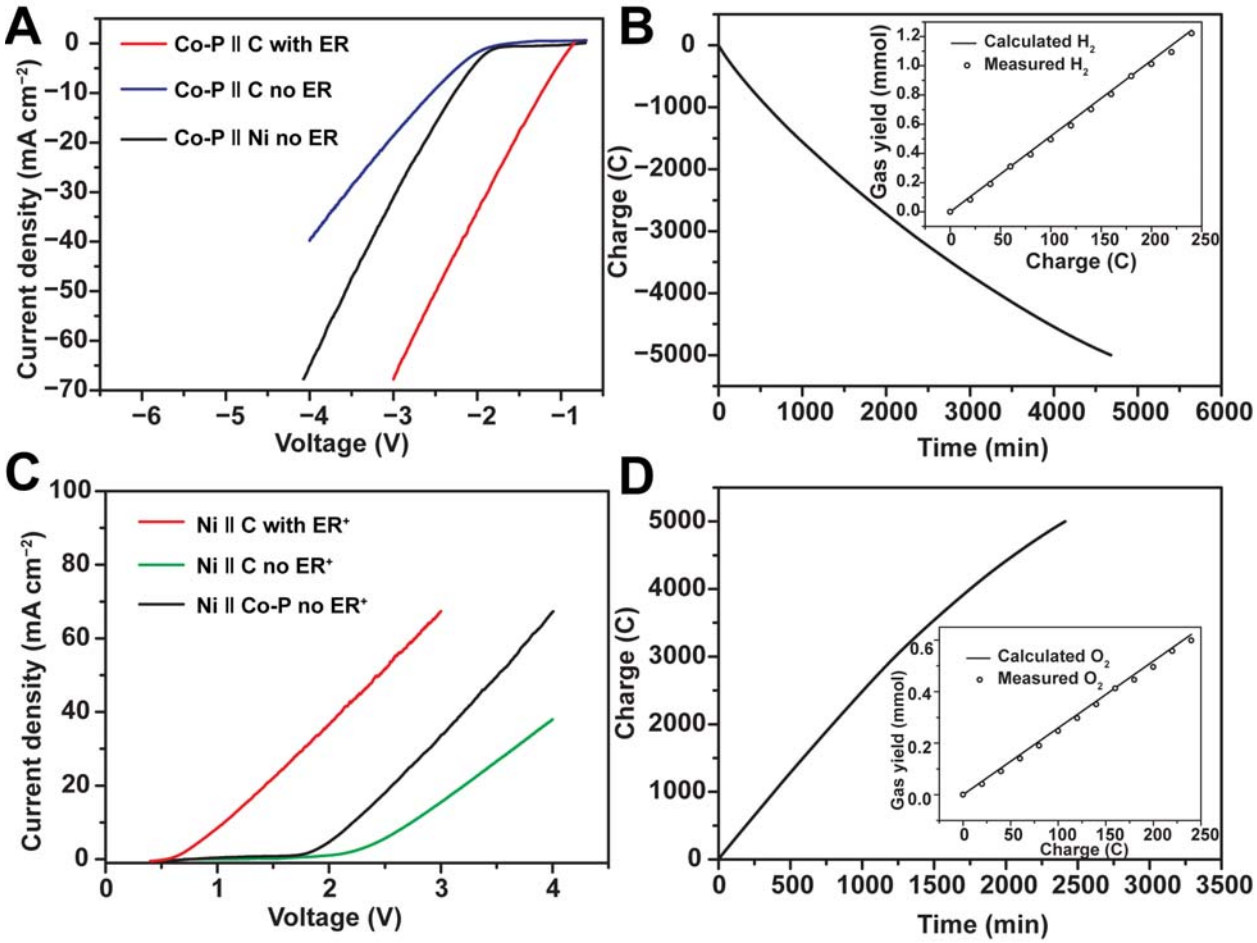

Figure S18. (A) Linear sweep voltammograms of the two-electrode H-cell systems consisting of a Co-P working electrode and a carbon counter electrode with (red) or without (blue) 0.3 M $[Fe(CN)_6]^{4-}$ (ER) in the counter compartment, and a Co-P working electrode and a Ni foam counter electrode without ER (black) at a scan rate of 5 mV s^{-1}. (B) Chronocoulometry curve of a Co-P working electrode for HER coupled with the oxidation of $[Fe(CN)_6]^{4-}$ in the counter compartment with a voltage input of −1.5 V. Inset is the comparison of GC-measured and theoretically calculated H_2 amounts during the electrolysis. (C) Linear sweep voltammograms of the two-electrode H-cell systems consisting of a Ni foam working electrode and a carbon counter electrode with (red) or without (green) 0.26 M $[Fe(CN)_6]^{3-}$ (ER^+) in the counter compartment, and a Ni foam working electrode and a Co-P counter electrode without ER^+ (black) at a scan rate of 5 mV s^{-1}. (D) Chronocoulometry curve of a Ni foam working electrode for OER coupled with the reduction of ER^+ in the counter compartment with a voltage input of 1.5 V. Inset is the comparison of GC-measured and theoretically calculated O_2 amounts during the electrolysis. For all the above experiments, both compartments of the H-cell contained 200 mL of 0.5 M Na_2SO_4 and 0.5 M NaPi buffer (pH = 7.0). All the results were not iR-corrected.

With the favorable electrochemical results of $Na_4[Fe(CN)_6]$ in hand, we next probed its function as an electron reservoir for decoupled water splitting. A two-compartment H-type electrochemical cell was adopted (**Scheme 1B**). All two-electrode electrochemical results were not iR-corrected. As shown in **Figure S18A**, a large voltage of −2.54 V is required to attain a cathodic current density of −10 mA cm^{-2} on a Co-P working electrode for HER if there was no electron reservoir in the counter compartment. However, upon the addition of 0.3 M $Na_4[Fe(CN)_6]$ in the counter chamber, the voltage bias is significantly reduced to −1.23 V to produce a catalytic current density of −10 mA cm^{-2}. In this case, the coupled reaction occurring on the carbon counter electrode was the oxidation of $[Fe(CN)_6]^{4-}$ to $[Fe(CN)_6]^{3-}$. A chronocoulometry electrolysis at −1.5 V (**Figure S18B**) was able to pass an amount of 5000 C charge within 78 h (theoretical charge capacity of 200 mL of 0.3 M $Na_4[Fe(CN)_6]$ is 5789 C). The produced H_2 amount quantified by gas

chromatography (GC) well matched the theoretically calculated quantity assuming that all the passed charge was utilized to form H_2 on Co-P, implying a Faradaic efficiency of nearly 100%. No O_2 was detected in headspace of the electrolyzer (**Figure S19**), indicating that the H_2 product has high purity without the requirement of downstream-purification *(e.g.,* catalytic de-oxygenation). In this step, the voltage input of −1.5 V between Co-P and carbon electrodes cannot drive the full water splitting (HER on Co-P and OER on carbon). The HER current on Co-P electrode gradually decreases, as the $[Fe(CN)_6]^{4-}$ is oxidized to $[Fe(CN)_6]^{3-}$ over the carbon electrode, leading to the decrease in the concentration of $[Fe(CN)_6]^{4-}$ in the counter chamber.

After a large portion of $[Fe(CN)_6]^{4-}$ (*ca.* 86.4%) had been oxidized to $[Fe(CN)_6]^{3-}$, we switched the working lead from Co-P to a Ni foam electrode and applied a positive voltage bias to drive OER. As shown in **Figure S18C**, the Ni foam electrode delivered an OER current density of 10 mA cm^{-2} at a small voltage of 1.06 V. In contrast, a much larger voltage input (2.74 V) was required to achieve the same OER current density in the absence of $[Fe(CN)_6]^{3-}$ in the counter compartment. A similar long-term chronocoulometry electrolysis for OER was also conducted and 100% Faradic efficiency for OER was also obtained (**Figure S18D**). In the meantime, no H_2 was detected during the whole process (**Figure S19**). In this step, the voltage input of 1.5 V between Ni foam and carbon electrodes cannot drive the full water splitting (OER on Ni and HER on carbon). The OER current on Ni foam electrode gradually decreases, as the $[Fe(CN)_6]^{3-}$ is reduced to $[Fe(CN)_6]^{4-}$ over the carbon electrode, leading to the decrease in the concentration of $[Fe(CN)_6]^{3-}$ in the counter chamber.

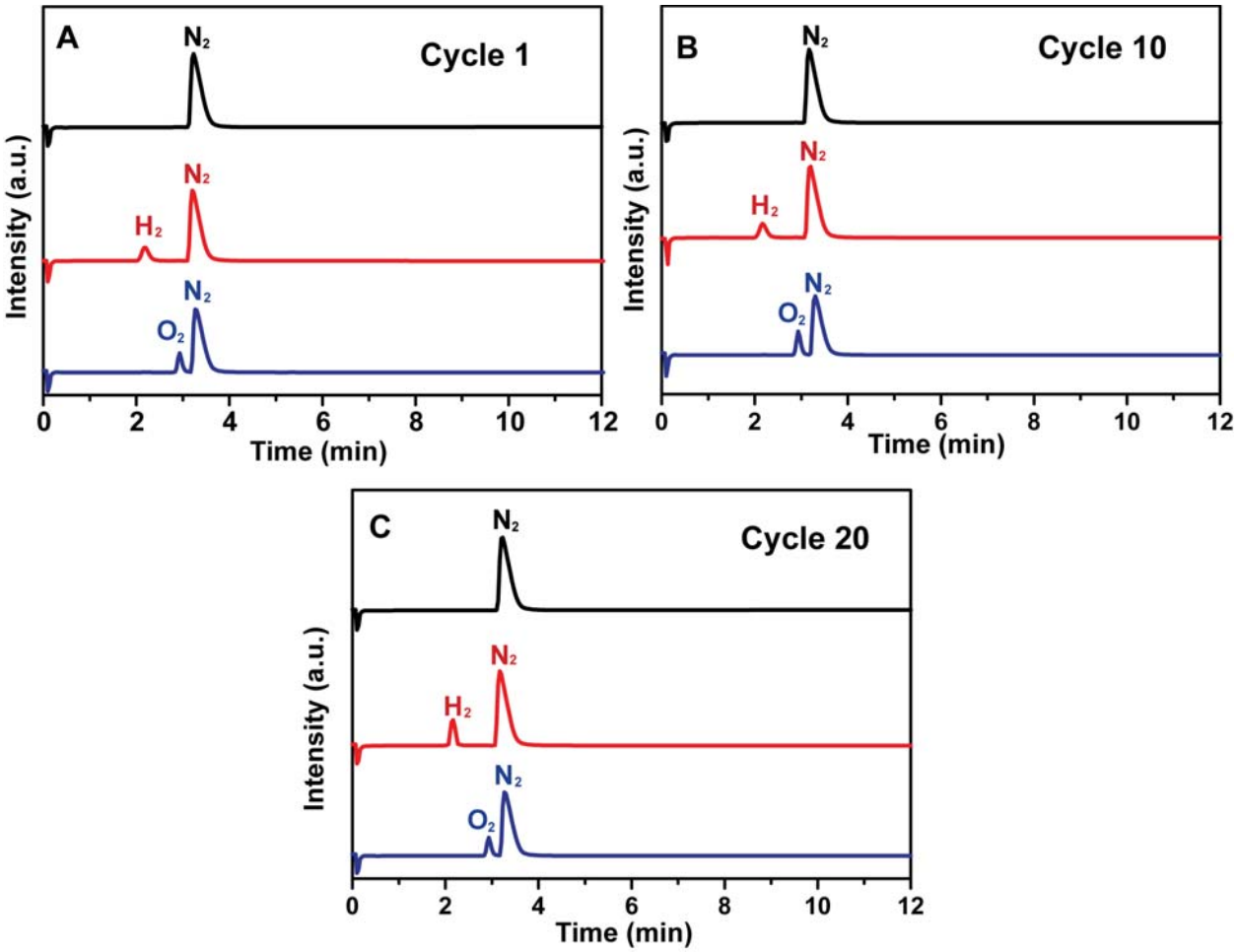

Figure S19. The representative gas chromatograph (GC) trace showing N_2 bubbling in the cell headspace (black line) and a typical GC trace showing that only H_2 was produced during HER electrolysis in the working compartment headspace (red line) and a GC trace showing that only O_2 was produced in the working cell headspace during OER electrolysis (blue line). The produced H_2 and O_2 in the cycling experiment were analyzed by GC in cycle 1 (A), 10 (B) and 20 (C) to confirm that the H_2/O_2 crossover for the overall cycling operation was minimized. The electrochemical chambers were thoroughly purged by N_2 when switching the electrocatalytic reaction in the working chamber between HER and OER.

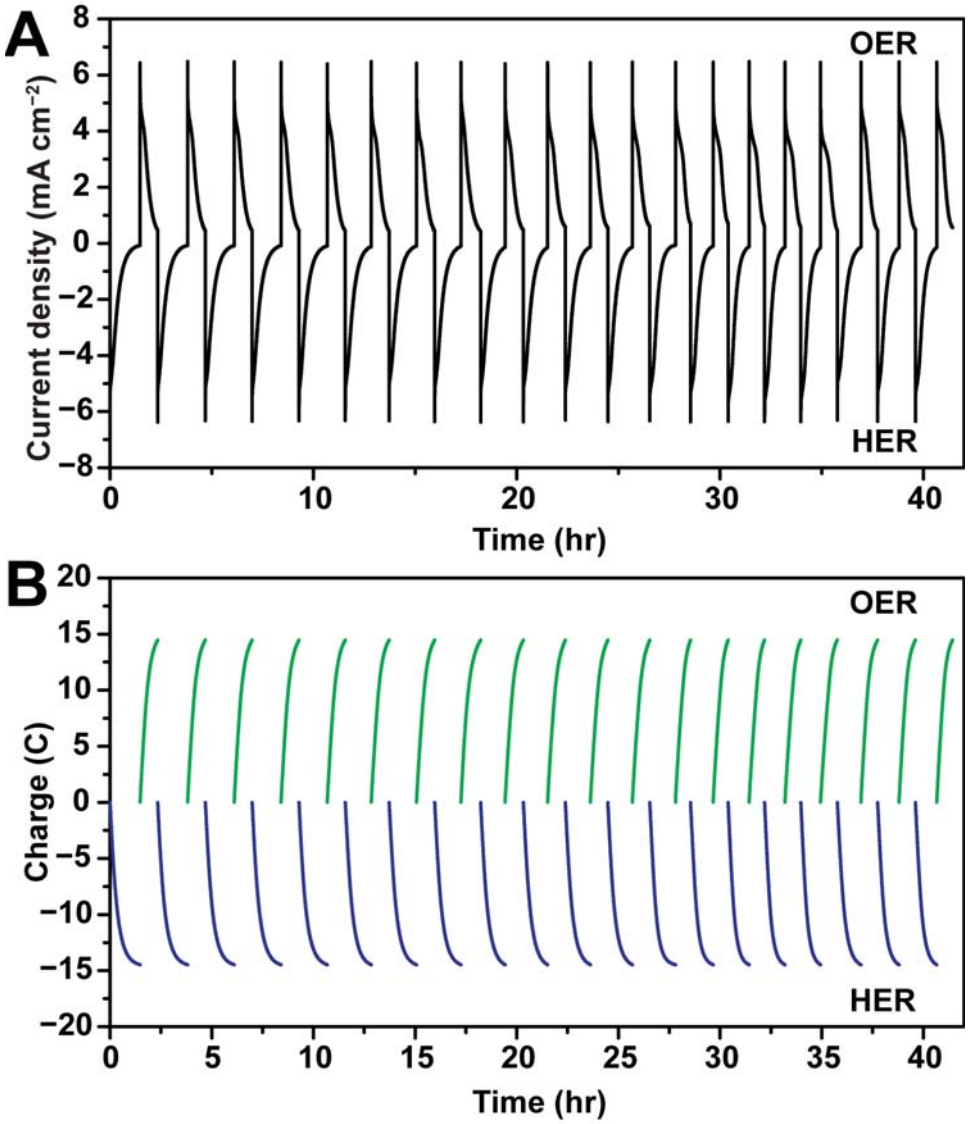

Figure S20. Multiple sequential bulk electrolysis cycles of the two-electrode systems (Co-P || carbon, or Ni foam || carbon) for decoupled water splitting. (A) Chronoamperometry and (B) chronocoulometry curves of the Co-P working electrode for HER and the Ni foam working electrode for OER alternately. The two working electrodes were placed in the working compartment charged with 0.5 M Na_2SO_4 and 0.5 M NaPi buffer (pH = 7) while a carbon rod electrode was positioned in the counter compartment which was not only filled with the same electrolyte but also 10 mM $Na_4[Fe(CN)_6]$. The input voltage alternated between −1.6 V on the Co-P working electrode for HER and 1.5 V on the Ni foam working electrode for OER. For each half cycle, the passed charge was equal to the theoretical charge capacity (14.472 C) of 10 mM $Na_4[Fe(CN)_6]$ (15 mL).

The robustness of $Na_4[Fe(CN)_6]$ as an electron reservoir for decoupled water splitting was evaluated by alternating HER and OER in a two-compartment electrolyzer for 20 consecutive cycles as shown in **Figure S20**. The applied voltage alternated between −1.6 V on the Co-P working electrode for HER and 1.5 V on the Ni foam working electrode for OER; while in the counter compartment 10 mM $Na_4[Fe(CN)_6]$ was oxidized and reduced periodically on a carbon electrode to couple the corresponding HER and OER in the working chamber (**Figure S20A**). In the step of HER coupled with oxidation of $Na_4[Fe(CN)_6]$, the HER current on Co-P electrode gradually decreases, as the $Na_4[Fe(CN)_6]$ is oxidized to $Na_3[Fe(CN)_6]$ over the carbon electrode, leading to the decrease in the concentration of $[Fe(CN)_6]^{4-}$ in the counter chamber. When the $Na_4[Fe(CN)_6]$ is completely oxidized to $Na_3[Fe(CN)_6]$, the HER current is reduced to nearly 0 mA, as

the voltage input of 1.6 V between Co-P and carbon electrodes cannot drive the water splitting (HER on Co-P and OER on carbon). Then the working lead is switched to Ni foam electrode and connected to the same carbon electrode by the external electrochemical workstation for the next step of OER coupled with reduction of $Na_3[Fe(CN)_6]$. The OER current on Ni foam electrode gradually decreases, as the $Na_3[Fe(CN)_6]$ is reduced to $Na_4[Fe(CN)_6]$, leading to the decrease in the concentration of $[Fe(CN)_6]^{3-}$ over the carbon electrode in the counter chamber. When the $Na_3[Fe(CN)_6]$ is completely reduced to $Na_4[Fe(CN)_6]$, the OER current is reduced to the minimum value, as the voltage input of 1.5 V between Ni foam and carbon electrodes cannot drive the water splitting (OER on Ni foam and HER on carbon). To achieve the cycling, the applied voltage alternates between −1.6 V on the Co-P working electrode for HER and 1.5 V on the Ni foam working electrode for OER; while in the counter compartment 10 mM $Na_4[Fe(CN)_6]$ is oxidized and reduced periodically on a carbon electrode to couple the corresponding HER and OER in the working chamber. The period for each cycle (one HER on Co-P and one OER on Ni foam) is around 2 h when using 10 mM $Na_4[Fe(CN)_6]$ electron reservoir for demonstrating the multiple sequential bulk electrolysis cycles here. Each half cycle was performed by passing 14.472 C charge, equivalent to the theoretical charge capacity of the electron reservoir (**Figure S20B**). Such a decoupled water electrolysis was conducted for 20 successive cycles over 41 h with no degradation, proving the great robustness of $Na_4[Fe(CN)_6]$ as an electron reservoir. Besides, the remarkable stability of $Na_4[Fe(CN)_6]$ was also demonstrated by the negligible degradation during 1000 redox cycles (**Figure S21**).

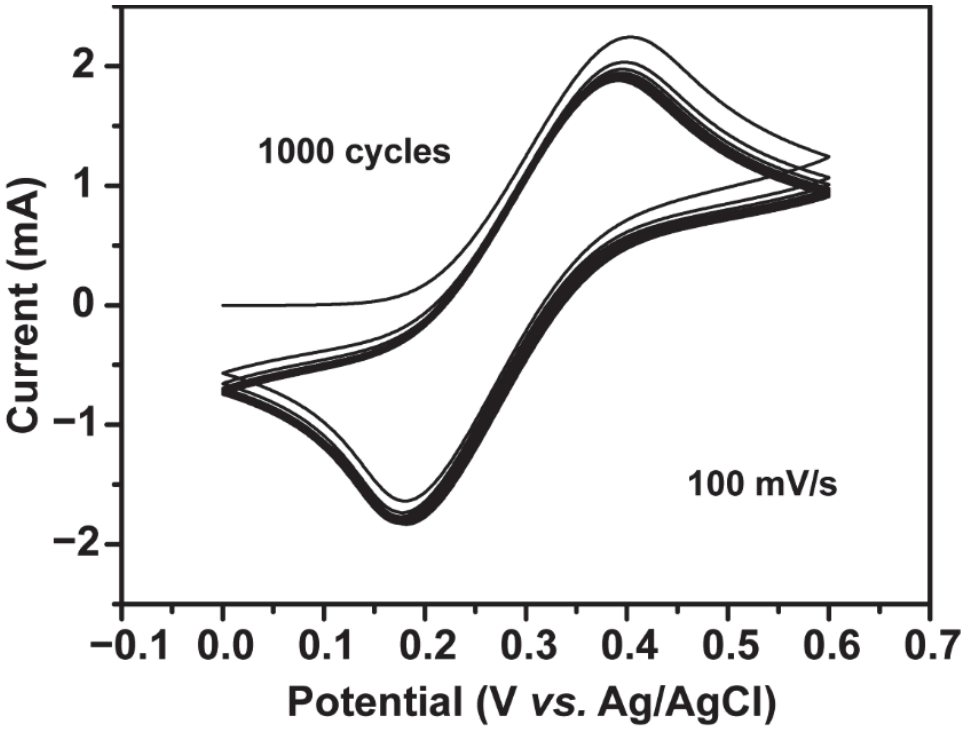

Figure S21. CV curves of 0.3 M of $Na_4[Fe(CN)_6]$ over a glassy carbon electrode at 100 mV s^{-1} for 1000 cycles. The electrolyte was 0.5 M Na_2SO_4 and 0.5 M sodium phosphate buffer (NaPi) solution (pH = 7.0) and the measurement was conducted in a three-electrode configuration. All curves were not iR-corrected.

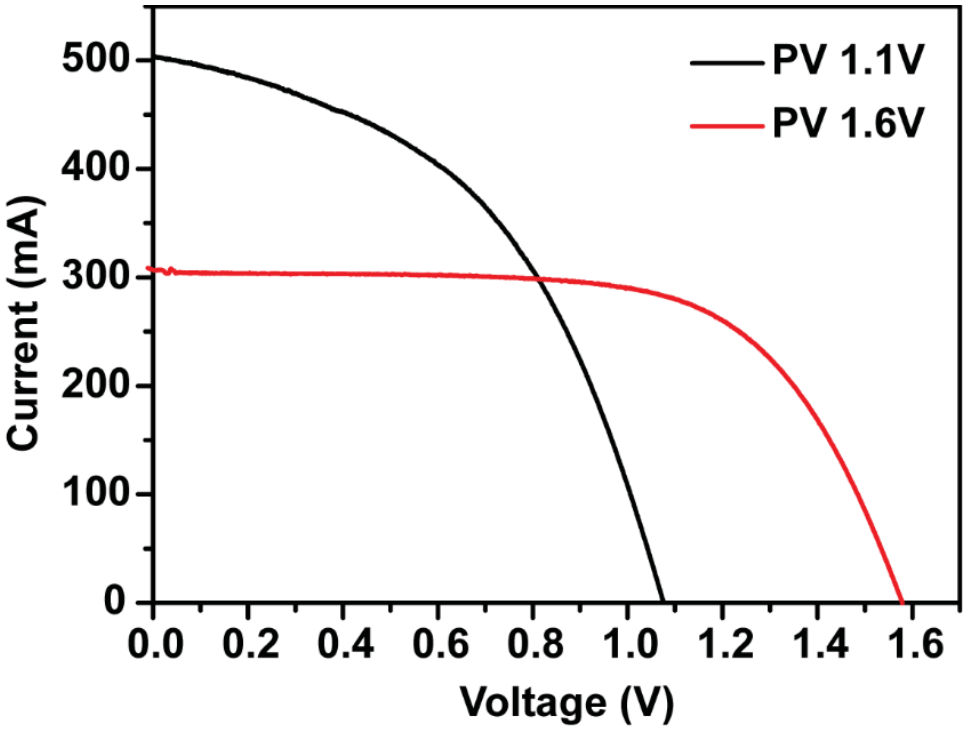

Figure S22. Current-voltage curves of the PV cells of 1.1 and 1.6 V used for driving decoupled water splitting in 0.5 M Na_2SO_4 and 0.5 M sodium phosphate buffer (NaPi) with 0.3 M $Na_4[Fe(CN)_6]$ electron reservoir under the natural sunlight irradiation (92 ± 5 mW cm^{-2}).

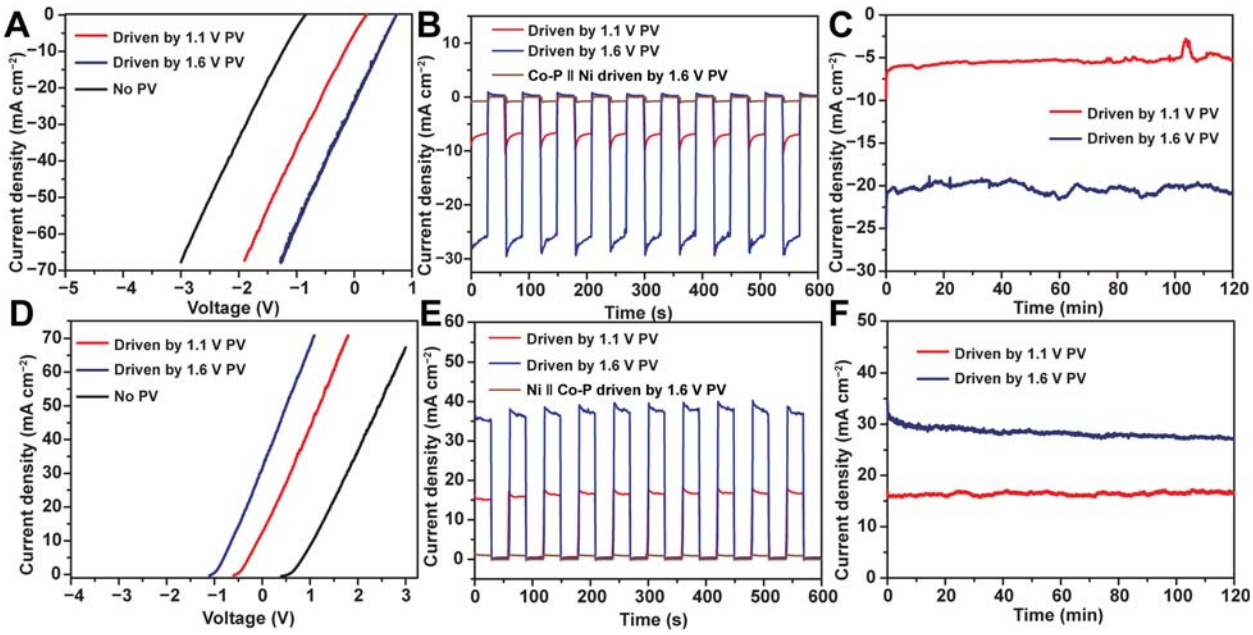

Figure S23. (A) Linear sweep voltammograms of a Co-P working electrode for HER coupled with the oxidation of 0.3 M $Na_4[Fe(CN)_6]$ on a carbon counter electrode with a 1.1 V (red) or 1.6 V (blue) photovoltaic (PV) cell or without (black) a PV cell under sunlight irradiation. (B) PV-driven HER electrolysis on a Co-P working electrode coupled with $Na_4[Fe(CN)_6]$ oxidation on a carbon counter electrode, or paired with OER on a Ni foam counter electrode without $Na_4[Fe(CN)_6]$ under chopped sunlight irradiation with no external voltage bias. (C) Chronoamperometry curves of PV-driven HER electrolysis on a Co-P working electrode coupled with $Na_4[Fe(CN)_6]$ oxidation on a carbon counter electrode with no external voltage bias. (D) Linear sweep voltammograms of a Ni foam working electrode for OER coupled with the reduction of 0.26 M $Na_3[Fe(CN)_6]$ on a carbon counter electrode with 1.1 V (red) or 1.6 V (blue) PV or without (black) a PV under sunlight irradiation. (E) PV-driven OER electrolysis on a Ni foam working electrode coupled with $Na_3[Fe(CN)_6]$ reduction on a carbon counter electrode, or paired with HER on a Co-P counter electrode without $Na_3[Fe(CN)_6]$ under chopped sunlight irradiation with no external voltage bias. (F) Chronoamperometry curves of PV-driven OER electrolysis on a Ni foam working electrode coupled with $Na_3[Fe(CN)_6]$ reduction on a carbon counter electrode with no external voltage bias. The electrolyte in both compartments was 0.5 M Na_2SO_4 and 0.5 M NaPi buffer (pH = 7.0). The areas of Co-P and Ni foam electrodes were 2 cm^2. All results were not iR-corrected.

Since the utilization of an electron reservoir has been proved to split a large voltage input of one-step water splitting to two smaller voltage inputs for separate HER and OER processes, we envision that photovoltaic (PV) cells with small photovoltage (< 1.23 V) would be able to drive decoupled water splitting without the need of tandem or multi-junction PVs.[S12,S14] Therefore, two commercial PV cells were used and their photovoltages were measured to be 1.1 and 1.6 V (**Figure S22)**, respectively, under natural sunlight irradiation. **Figure S23A** compares the linear sweep voltammograms (LSV) of a Co-P working electrode for HER with and without PV cells. With the assistance of 1.1 or 1.6 V PV cells, a current density of −5.4 and −24 mA cm^{-2} for H_2 evolution was achieved at zero external bias. **Figure S23B** plots the cathodic current evolution with PV cells under chopped sunlight irradiation at zero external bias. The instantaneous on/off change of the current density responding to periodic sunlight irradiation suggests that the obtained HER current was solely determined by sunlight illumination. A control experiment with a Co || Ni electrode couple without $Na_4[Fe(CN)_6]$ showed negligible cathodic current with 1.6 V PV cell, highlighting the important role of the electron reservoir in lowering the required voltage input. The stability of such a PV-electrolysis system was confirmed by measuring the HER current density change over 2 h with the assistance of the above two PV cells under natural sunlight irradiation (**Figure S23C**). The current densities were maintained at −5.3 and −21 mA cm^{-2} powered by PV of 1.1 and 1.6 V, respectively. After the $Na_4[Fe(CN)_6]$ in the counter compartment had been mostly oxidized to $Na_3[Fe(CN)_6]$, the LSV curves of a Ni form working electrode for OER were collected (**Figure S23D**). Analogous to the above HER situation, much lower voltage inputs were

required to achieve appreciable anodic current density with PV cells. In the absence of any external bias, the obtained OER current density is highly dependent on the sunlight illumination upon PV cells, as demonstrated by the chopped-sunlight experiment (**Figure S23E**). No apparent current was observed using a Ni || Co-P couple powered by a 1.6 V PV cell under sunlight irradiation without $Na_3[Fe(CN)_6]$ in the counter compartment. The OER currents were stabilized at 16.7 and 27.5 mA cm^{-2} for a 2-hour electrolysis driven by PV cells of 1.1 and 1.6 V, respectively, under natural sunlight illumination (**Figure S23F**). It should be noted that the aforementioned solar-driven experiments for were performed without iR compensation and the internal resistance of our PV-electrolysis systems was measured as *ca.* 14 Ω (**Figure S24**).

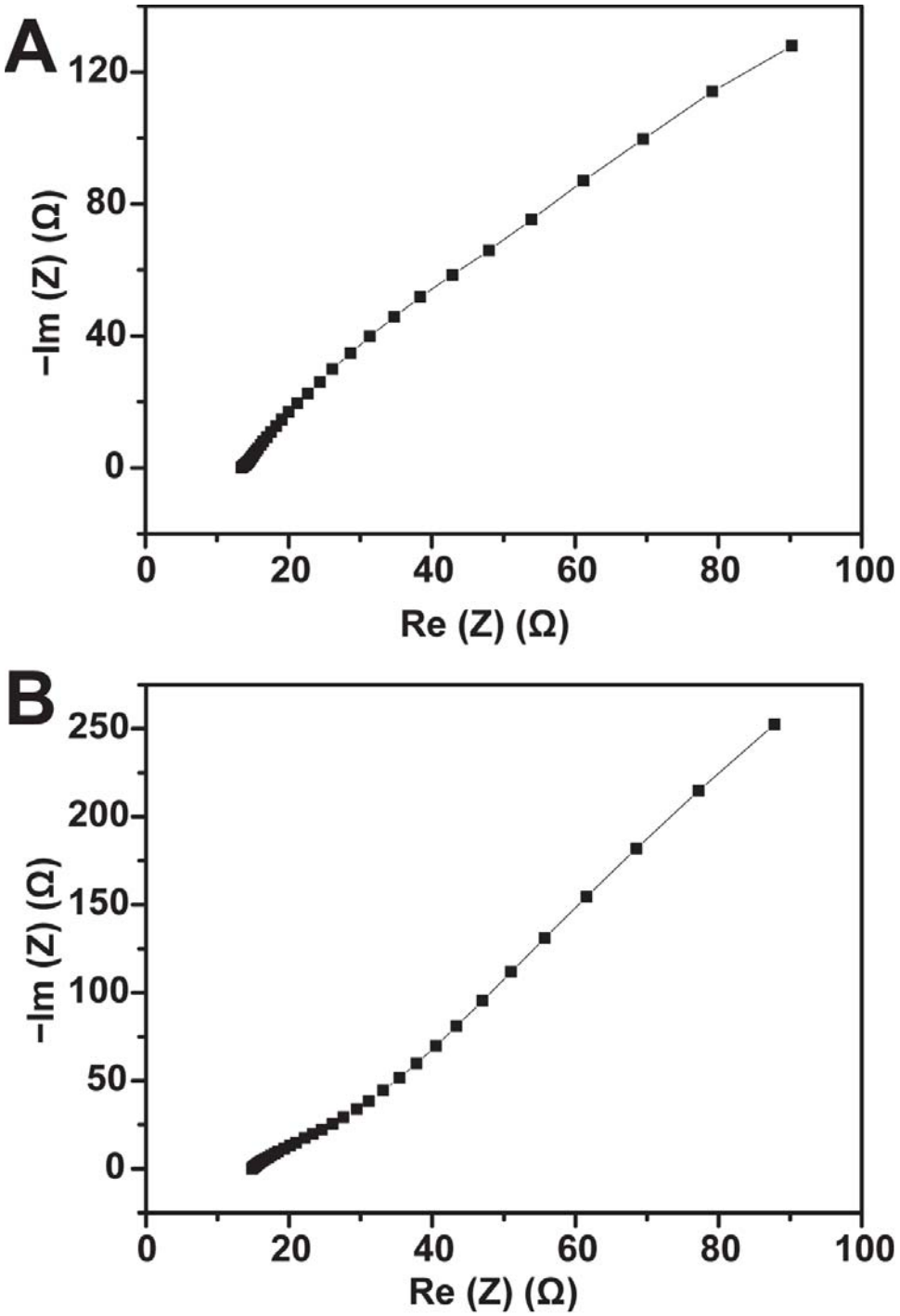

Figure S24. Electrochemical impedance spectroscopy (EIS) Nyquist plots of the Co-P (A) and Ni foam (B) working electrodes in 0.5 M Na_2SO_4 and 0.5 M NaPi buffer. The counter chamber contained either 0.3 M $Na_4[Fe(CN)_6]$ (coupled with the Co-P working electrode) or $Na_3[Fe(CN)_6]$ (coupled with Ni foam working electrode) in 0.5 M Na_2SO_4 and 0.5 M NaPi buffer with a carbon counter electrode.

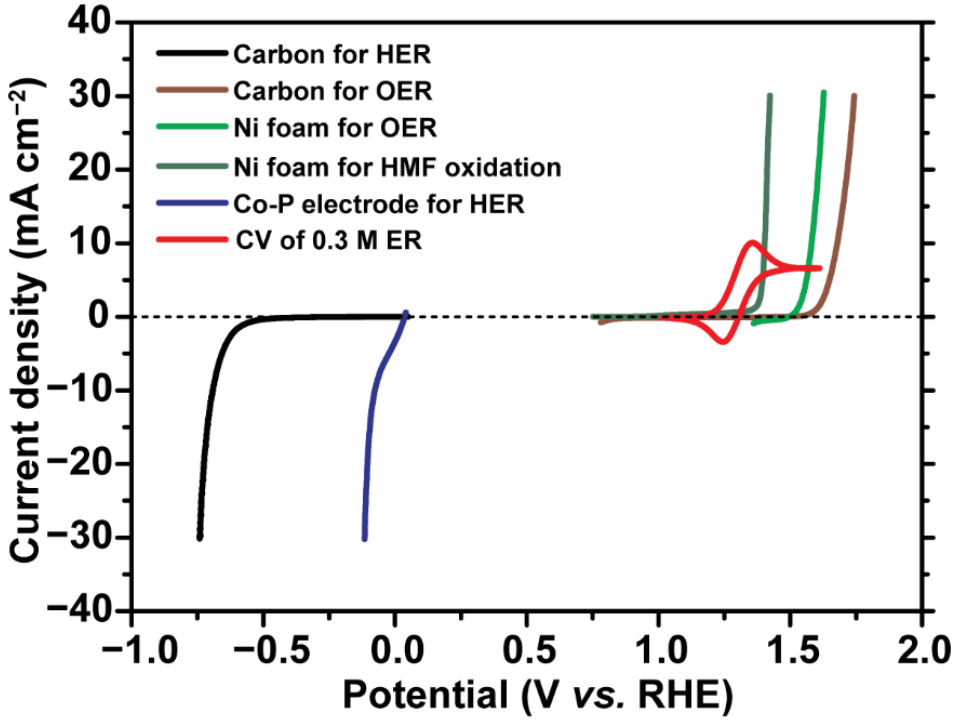

Figure S25. Polarization curves of carbon electrode, Ni foam and Co-P electrode, and CV curve of 0.3 M $Na_4[Fe(CN)_6]$ over a glassy carbon electrode measured in 1 M NaOH at a scan rate of 5 mV s^{-1}. All polarization curves were iR-corrected.

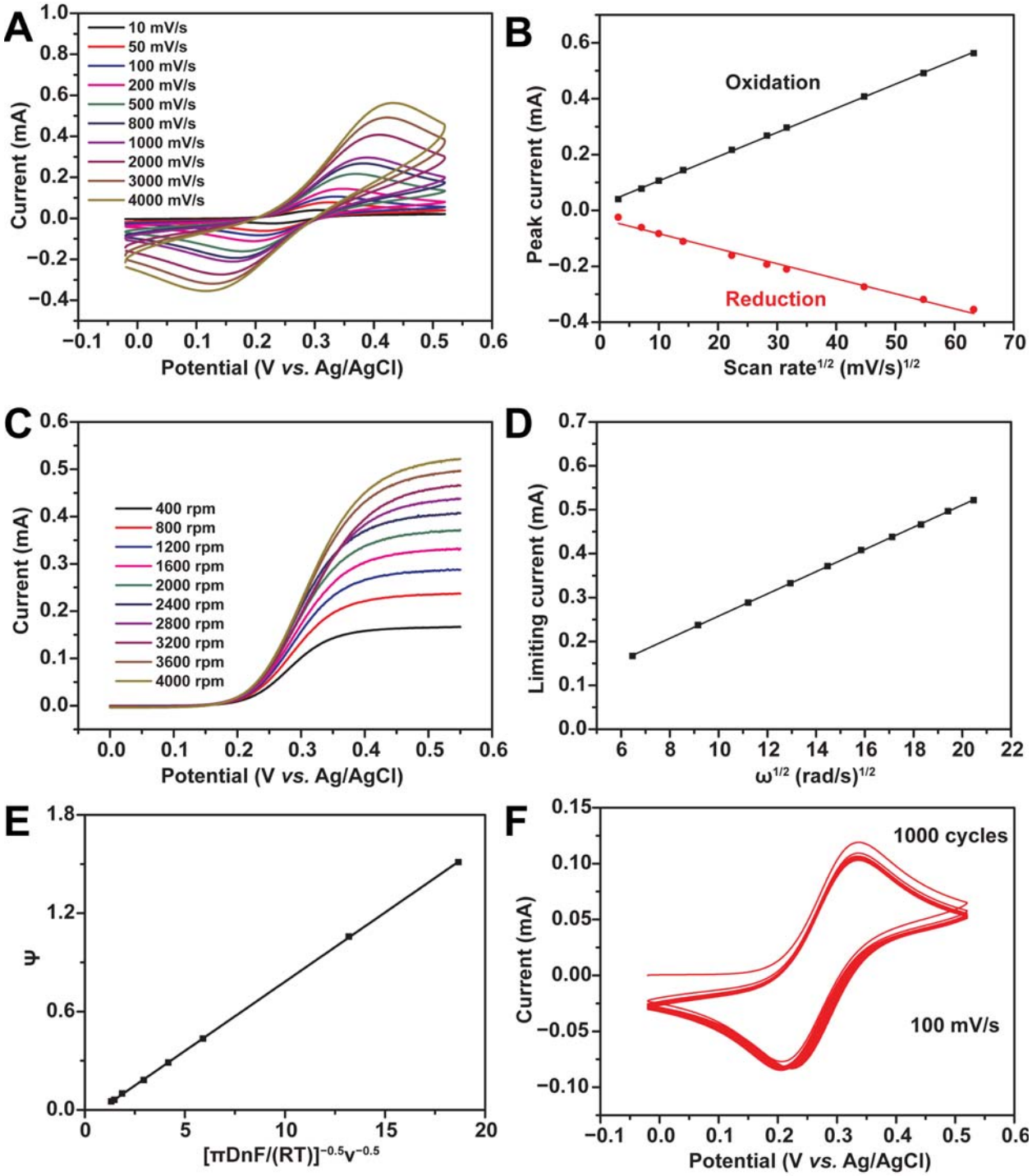

Figure S26. (A) Cyclic voltammetry (CV) curves of 10 mM $Na_4[Fe(CN)_6]$ over a glassy carbon electrode at varying scan rates from 10 to 4000 mV s^{-1}. (B) Plots of oxidation and reduction peak currents *vs.* square root of scan rate for 10 mM of $Na_4[Fe(CN)_6]$. (C) Linear sweep voltammetry (LSV) curves of 10 mM of $Na_4[Fe(CN)_6]$ over a rotating disk glassy carbon electrode scanned at 5 mV s^{-1} at different rotation speeds ranging from 400 to 4000 rpm. (D) Levich plot of the limiting current *vs.* the square root of rotation rates for 10 mM of $Na_4[Fe(CN)_6]$. (E) Plot of Ψ versus $[\pi DnF/(RT)]^{-0.5}v^{-0.5}$ for calculating the electron transfer rate constant of $Na_4[Fe(CN)_6]$. (F) CV curves of 10 mM of $Na_4[Fe(CN)_6]$ over a glassy carbon electrode at 100 mV s^{-1} for 1000 cycles. The electrolyte was 1.0 M NaOH. The area of either the glassy carbon electrode or rotating disk glassy carbon electrode was 0.07065 cm^2. All plots were not iR-corrected.

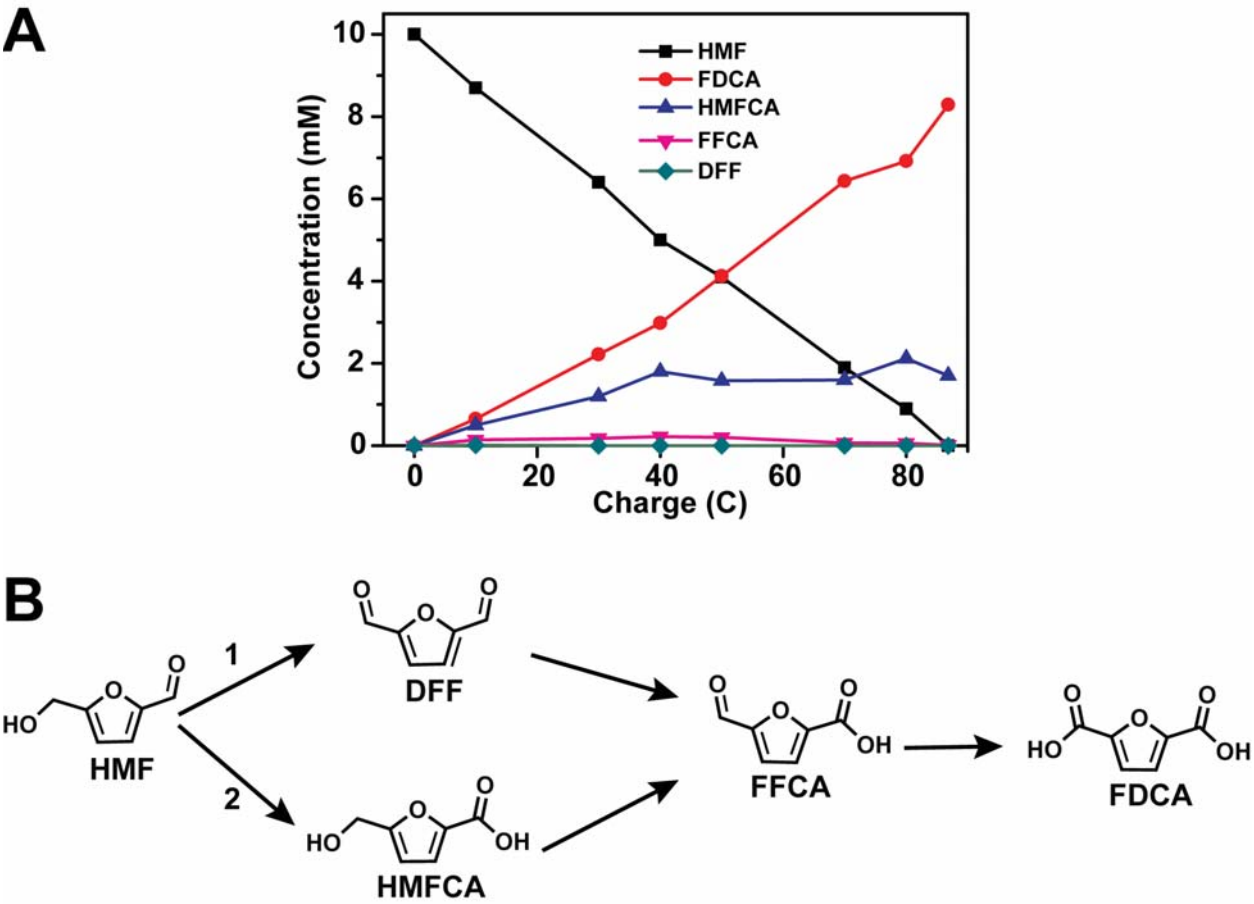

Figure S27. (A) Concentration of HMF and its oxidation products during electrolysis. (B) Two possible pathways of HMF oxidation to FDCA.

III. Supplemental Table

Table S1. Comparison of our electron reservoir-mediated decoupled water electrolyzers with reported decoupled water splitting systems with redox mediators.

Electron reservoirs / Redox mediators	Electrocatalysts	Electrolyte	Total voltage for both HER and OER (V)	Energy efficiency (%)	Reference
$Na_4[Fe(CN)_6]$	Co-P for HER Ni for OER	0.5 M Na_2SO_4 and 0.5 M NaPi buffer (pH = 7.0)	2.29	64.6	This work
FcNCl	Ni_2P/Ni for HER Ni for OER	0.5 M Na_2SO_4 (pH = 6.5)	2.43	61	This work
$(H_3O^+)[H_2PMo_{12}O_{40}]^-$	Pt for HER and OER	1 M H_3PO_4 (pH = 1.0)	2.5	59.2	[S7]
$H_4[SiW_{12}O_{40}]$	Pt/C for HER Pt for OER	1 M H_3PO_4 (pH = 1.0)	2.37	63	[S6]
No redox mediator	Pt/C for HER Pt for OER	1 M H_3PO_4 (pH = 1.0)	2.21	67	
Potassium hydroquinone sulfonate	Pt/C for HER Pt for OER	1.8 M H_3PO_4 (pH = 0.7)	2.4	61.6	[S9]
V(II)/V(III) and Ce(III)/Ce(IV)	Mo_2C for HER RuO_2 for OER	1 M H_2SO_4	N/A	48	[S18]
$Ni(OH)_2$/NiOOH	Pt for HER RuO_2/IrO_2 for OER	1 M KOH (pH = 14)	2.1	70	[S8]
$Ni(OH)_2$/NiOOH	Ni for HER Co_3O_4 for OER	1 M KOH (pH = 14)	2.25	65.7	
$Ni(OH)_2$/NiOOH	Pt for HER Ir for OER	1 M NaOH (pH = 14)	2.21	67	[S15]
$Ni(OH)_2$/NiOOH	Ni for HER Ni for OER	1 M NaOH (pH = 14)	2.3	64.3	

IV. Supplemental References

[S1] Hu, B., DeBruler, C., Rhodes, Z., and Liu, T.L. (2017). Long-cycling aqueous organic redox flow battery (AORFB) toward sustainable and safe energy storage. J. Am. Chem. Soc. *139*, 1207–1214.

[S2] Nicholson, R.S. (1965). Theory and application of cyclic voltammetry for measurement of electrode reaction kinetics. Anal. Chem. *37*, 1351–1355.

[S3] Lavagnini, I., Antiochia, R., and Magno, F. (2004). An extended method for the practical evaluation of the standard rate constant from cyclic voltammetric data. Electroanalysis *16*, 505–506.

[S4] Bockris, J., Conway, B., Yeager, E., and White, R. (1981). Comprehensive treatise of electrochemistry: electrochemical processing (Plenum Press).

[S5] Qi, Z. (2013). Proton exchange membrane fuel cells (CRC Press).

[S6] Rausch, B., Symes, M.D., Chisholm, G., and Cronin, L. (2014). Decoupled catalytic hydrogen evolution from a molecular metal oxide redox mediator in water splitting. Science *345*, 1326–1330.

[S7] Symes, M.D. and Cronin, L. (2013). Decoupling hydrogen and oxygen evolution during electrolytic water splitting using an electron-coupled-proton buffer. Nat. Chem. *5*, 403–409.

[S8] Chen, L., Dong, X., Wang, Y., and Xia, Y. (2016). Separating hydrogen and oxygen evolution in alkaline water electrolysis using nickel hydroxide. Nat. Commun. *7*, 11741.

[S9] Rausch, B., Symes, M. D., and Cronin, L. (2013). A bio-inspired, small molecule electron-coupled-proton buffer for decoupling the half-reactions of electrolytic water splitting. J. Am. Chem. Soc. *135*, 13656–13659.

[S10] Ursua, A., Gandia, L.M., and Sanchis, P. (2012). Hydrogen production from water electrolysis: current status and future trends. Proc. IEEE *100*, 410–426.

[S11] Carmo, M., Fritz, D.L., Mergel, J., and Stolten, D. (2013). A comprehensive review on PEM water electrolysis. Int. J. Hydrogen Energy *38*, 4901–4934.

[S12] Jia, J., Seitz, L.C., Benck, J.D., Huo, Y., Chen, Y., Ng, J.W.D., Bilir, T., Harris, J.S., and Jaramillo, T.F. (2016). Solar water splitting by photovoltaic-electrolysis with a solar-to-hydrogen efficiency over 30%. Nat. Commun. *7*, 13237.

[S13] Ma, W., Han, J., Yu, W., Yang, D., Wang, H., Zong, X., and Li, C. (2016). Integrating perovskite photovoltaics and noble-metal-free catalysts toward efficient solar energy conversion and H_2S splitting. ACS Catal. *6*, 6198–6206.

[S14] Luo, J., Im, J.-H., Mayer, M.T., Schreier M., Nazeeruddin, M.K., Park, N.-G., Tilley, S.D., Fan, H.J., and Grätzel, M. (2014). Water photolysis at 12.3% efficiency via perovskite photovoltaics and Earth-abundant catalysts. Science *345*, 1593–1596.

[S15] Landman, A., Dotan, H., Shter, G.E., Wullenkord, M., Houaijia, A., Maljusch, A., Grader, G.S., and Rothschild, A. (2017). Photoelectrochemical water splitting in separate oxygen and hydrogen cells. Nat. Mater. *16*, 646–651.

[S16] Konopka, S.J., and McDuffie, B. (1970). Diffusion coefficients of ferri- and ferrocyanide ions in aqueous media, using twin-electrode thin-layer electrochemistry. Anal. Chem. *42*, 1741–1746.

[S17] Daum, P.H., and Enke, C.G. (1969). Electrochemical kinetics of the ferri-ferrocyanide couple on platinum. Anal. Chem. *41*, 653–656.

[S18] Amstutz, V., Toghill, K.E., Powlesland, F., Vrubel, H., Comninellis, C., Hu, X., and Girault, H.H. (2014). Renewable hydrogen generation from a dual-circuit redox flow battery. Energy Environ. Sci. *7*, 2350–2358.